University of Illinois at Urbana-Champaign

ACRC

Air Conditioning and Refrigeration Center A National Science Foundation/University Cooperative Research Center

An Analytical and Empirical Study of Frost Accumulation Effects on Louvered-Fin, Microchannel Heat Exchangers

Y. Xia, P. S. Hrnjak, and A. M. Jacobi

ACRC TR-256 December 2006

For additional information:

Air Conditioning and Refrigeration Center
University of Illinois
Department of Mechanical Science & Engineering
1206 West Green Street
Urbana, IL 61801

(217) 333-3115

Prepared as part of ACRC Project #132
Investigation of Refrigerant/Oil Mixtures in Horizontal Tubes and Flat Plate Condensers and Evaporators
A. M. Jacobi, P. S. Hrnjak, and J. G. Georgiadis, Principal Investigators

And part of ACRC Project #177
Ultra-hydrophobic Surfaces for Heat Exchangers in Air-Conditioning Systems
A. M. Jacobi, Principal Investigator

The Air Conditioning and Refrigeration Center was founded in 1988 with a grant from the estate of Richard W. Kritzer, the founder of Peerless of America Inc. A State of Illinois Technology Challenge Grant helped build the laboratory facilities. The ACRC receives continuing support from the Richard W. Kritzer Endowment and the National Science Foundation. The following organizations have also become sponsors of the Center.

Arçelik A. S.
Behr GmbH and Co.
Carrier Corporation
Cerro Flow Products, Inc.
Daikin Industries, Ltd.
Danfoss A/S
Delphi Thermal and Interior
Embraco S. A.
Emerson Climate Technologies, Inc.
General Motors Corporation
Hill PHOENIX
Honeywell, Inc.
Hydro Aluminum Precision Tubing
Ingersoll-Rand/Climate Control
Lennox International, Inc.
LG Electronics, Inc.
Manitowoc Ice, Inc.
Matsushita Electric Industrial Co., Ltd.
Modine Manufacturing Co.
Novelis Global Technology Centre
Parker Hannifin Corporation
Peerless of America, Inc.
Samsung Electronics Co., Ltd.
Sanden Corporation
Sanyo Electric Co., Ltd.
Tecumseh Products Company
Trane
Visteon Automotive Systems
Wieland-Werke, AG

For additional information:

Air Conditioning & Refrigeration Center
Mechanical & Industrial Engineering Dept.
University of Illinois
1206 West Green Street
Urbana, IL 61801

217 333 3115

Abstract

The thermal-hydraulic behavior of folded-louvered-fin, microchannel heat exchangers is explored under conditions of air-side frosting, defrosting, and refrosting. The temperature distribution within a two-dimensional composite fin is analyzed. A parametric analysis shows that for some conditions, such as those typical to frost-coated fins, the problem can be approximated as a two-dimensional slab on a one-dimensional fin. Under this approximation, an exact solution to the heat diffusion equation is obtained through an eigenfunction expansion. The analytical solution and a one-term approximation to the full solution have broad applicability in addition to their use for calculating fin efficiency for frost-coated fins.

Valid *HA*-LMED and *UA*-LMTD methods for wet- and frosted-surface heat transfer are formulated. The *UA*-LMTD method is shown to provide the best results for dry, partially-wet/frosting, and fully-wet/frosting conditions. Without area partitioning, the *HA*-LMED method is only applicable to fully-wet/frosting conditions. For all the conditions considered in a parametric study to mimic the experimental range of this work, the *UA*-LMTD method provides the value of the air-side convective heat transfer coefficient within 3% and is more accurate than the *HA*-LMED method.

Heat transfer and pressure drop data for nine different fin geometries are presented, and a decrease in the overall heat transfer coefficient and an increase in the pressure drop are observed as frost accumulates on the surfaces. A reduction in air-side flow rate and bridging of louver gaps by frost are identified as the factors most important to the reduced heat transfer performance. Correlations are presented for predicting the thermal performance of these heat exchangers under frosting conditions.

A numerical model is developed to predict the time-varying performance of folded-louvered-fin, microchannel heat exchangers. The model utilizes the correlations developed from the experimental data and incorporates a sub-model for frost properties. The model successfully predicts the heat transfer performance of the heat exchangers studied, but its ability to predict the pressure-drop behavior needs further improvement. The model can be used to evaluate geometry effects on the frosting behavior of the louvered-fin, microchannel heat exchangers, and can be easily generalized to other applications with simultaneous heat and mass transfer.

Table of Contents

List of Figures

Page

List of Tables

Page

Chapter 1. Introduction

1.1 Background

Folded-louvered-fin, microchannel heat exchangers are usually constructed by brazing folded (sometimes called serpentine) fins to extruded microchannel tubes. This type of heat exchanger is finding wider application as performance, compactness and cost concerns continue to drive heat exchanger design. In order to use folded-fin microchannel heat exchangers in heat-pump or refrigeration systems in which frosting occurs, the effect of frost accumulation on their performance must be characterized. Unfortunately, few design guidelines can be found for using microchannel heat exchangers under frosting conditions, due to lack of performance data. Moreover, very few models exist that can predict the transient performance of extended-surface heat exchangers, not to mention this type of heat exchanger with such complex and compact fin structures.

In this chapter, a detailed literature review on the research related to frost formation and its effects on the thermal-hydraulic characteristics of moist air flow in simple geometries and extended surface heat exchangers will be provided, followed by the proposed objectives.

1.2 Literature Review

1.2.1 Frost Properties and Growth in Simple Geometries

Over the past several decades, significant research has been conducted on frost properties and growth in simple geometries. O'Neal and Tree (1985) provided an early review of frost formation in simple geometries. They grouped the literature into three categories: frost properties, heat transfer, and mass transfer, and they focused on available empirical correlations and complementary analytical developments.

1.2.1.1 Frost Properties and Growth on a Flat Surface

Yonko and Sepsy (1967) experimentally investigated the thermal conductivity of frost forming on a flat horizontal plate. They also formulated a theoretical expression for the thermal conductivity of frost, based on a composite model consisting of a cubic lattice of uniform spherical ice particles surrounded by humid air. Although they correlated the thermal conductivity data with frost density, they expressed the concern that other factors could also affect frost thermal conductivity, and demonstrated that two frost layers with identical density but different macroscopic structures (caused by the melting and refreezing of the upper frost layer) could have different thermal conductivities.

Trammell *et al.* (1968) conducted experiments on frost formed on a flat plate held at sub-freezing temperatures in a humid air stream to study the effect of air velocity, air humidity, and air and plate temperatures on the formation. They measured frost thickness using an optical dial gauge, and determined frost density from the thickness data and the amount of radiation absorbed by the frost layer from a radioactive source. Their test range of the plate temperatures, however, was from –51 to –73 ˚C, which is not applicable to the heat pump and refrigeration applications motivating this study.

Brian *et al.* (1970) measured frost density, thermal conductivity, and heat and mass flux for frost deposited on a cold plate from a humid air stream. They also correlated the data using a simple analytical model which emphasized the internal diffusion processes within the frost. A density measurement within the frost layer indicated that, within the accuracy of the method they used, there was no significant density gradient in the frost layer.

Yamakawa *et al.* (1972) developed an experimental apparatus to measure the local heat and mass transfer coefficient, the effective thermal conductivity, and density of frost on a flat surface under conditions of forced convection. They proposed four methods to measure the frost surface temperature, and compared the results obtained from two of them, *i.e.* the method of directly contacting a thermocouple with the frost layer, and the method of using an infrared radiation thermometer. They found that the heat transfer coefficient was greater with frost growth than that without frost growth, due to roughness of the frost layer surface. Their results showed that frost density may not be the only factor determining the effective thermal conductivity, and they suggested that the influence of mass transfer caused by moisture diffusion must also be considered.

Jones and Parker (1975) formulated a theoretical model of frost growth based on molecular diffusion of water vapor at the frost surface. They used energy and mass balances to incorporate varying environmental parameters that were related to heat and mass transfer coefficients at the frost surface. In their model of diffusion within the frost layer, they considered the decreased effective cross-sectional area for diffusion and the increased path length the molecules must travel (tortuosity). The model showed good agreement with the observed trends.

Hayashi, Aoki, and Adachi (1977) classified frost formation types into four groups according to their structure in the temperature range from 0 to –25 ˚C. The classification was schematically shown on a ΔC-t_s plane, where ΔC is the humidity ratio difference between a main stream and a cold surface, and t_s is the cold surface temperature. Their frost thermal conductivity data showed that heat transfer in a frost layer was affected not only by the frost density but also by factors such as the structure of a frost layer, the internal diffusion of water vapor, and the flow structure caused by the roughness of the frost surface. They developed a model to predict the effective frost thermal conductivity by applying Woodside's equation to a composite parallel model of a frost layer composed of ice columns and ice-air composite material.

Hayashi, Aoki, and Yuhara (1977) divided the frost formation process into three characteristic periods: "crystal growth period," "frost layer growth period," and "frost layer full growth period." They stated that during the "frost layer growth period," which spanned the most testing time, the frost columns generated in the "crystal growth period" changed into a more uniform frost layer. While in the "frost layer full growth period," the frost-layer shape did not change until melting occurred at the frost surface. They also proposed a structural model to analyze the frost deposition rate, frost height, and mass transfer coefficient in the "frost layer growth" period. The model included three-dimensional diffusion in a finite hollow cylinder to model the water vapor concentration distribution. They formulated an empirical equation for frost density applicable in their experimental range, *i.e.* $\rho=650\cdot\exp(0.277\cdot T_s)$, where T_s is the frost surface temperature in ºC. The frost height predicted using the equation was in good agreement with the experimental results.

Abdel-Wahed *et al.* (1982) theoretically and experimentally examined the factors that influenced the heat and mass transfer from a laminar humid air stream at temperatures above 0 ºC to a plate at subfreezing temperature. They correlated experimental measurements of heat and mass transfer coefficients for frost growth up to 600 minutes using equations for the local Nusselt and Sherwood numbers.

Schulte and Howell (1982) experimentally investigated the effect of turbulence intensity on the growth rate of frost on a cold flat plate in order to reduce the frosting problem, but they found that the effect of air turbulence on frost growth was negligible.

Dietenberger (1983) reviewed a number of papers addressing the problem of computing the frost thermal conductivity, focusing on the underlying assumptions of each method. After evaluating and comparing the different published methods, he presented a new model based on two assumed types of frost structure: random mixture of ice cylinders and ice spheres for low frost density, and random mixture of ice planes and air bubbles for high frost density. His model, including the so-called water vapor conductivity but not the eddy conductivity, was intended to be a general model that covered all possible frost densities; however, it still required a structural parameter to be determined using experimental data for frost conductivity.

Tokura *et al.* (1983) conducted an experimental study of the properties and growth rate of a frost layer on a cooled vertical plate in a free convection flow. They divided the frost formation process into two regions, depending on a dimensionless parameter based on the difference in water vapor density between the ambient air and the wall. They reported that the frost layer grew linearly with time when the value of this parameter was less than 0.1, and grew proportionally to the square root of time when the value was larger. Correlations were developed for the two regimes, but they did not discuss the bases for these correlations.

Sami and Duong (1989) developed a model similar to that of Jones (1975) to predict frost formation and growth processes. They adopted a similar model of water-vapor molecular diffusion in frost layer, but offered an improvement in the ability to predict the spatial variation of the frost density. Compared to other analytical models of the time, their model showed better agreement with experimental data.

Mao and co-workers presented correlations for frost thickness, mass concentration, and heat flux of frost growth in turbulent (Mao *et al.* 1992) and laminar (Mao *et al.* 1993) airflows at room temperature over a cold flat plate. The frost properties were correlated as a function of dimensionless variables, such as dimensionless position ratio (the distance from the leading edge to the channel hydraulic diameter), air inlet humidity ratio, dimensionless temperature ratio, the Reynolds number based on hydraulic diameter at the inlet, and the Fourier number based on the thermal diffusivity of air with the hydraulic diameter at the inlet as the characteristic length. The correlations were less accurate for a small humidity ratio.

Tao *et al.* (1993a) experimentally investigated frost formation on a cold flat plate with forced convection during the initial growth period. They quantified the characteristic sizes of ice particles and the transition times of the subcooling and crystal growth period using microscopic observations. The results were used as the input (initial parameters) in their numerical model of frost formation.

Tao *et al.* (1993b) used a one-dimensional, transient formulation to simulate frost deposition on a cold surface exposed to a warm moist airflow. Based on a volume-averaging technique, the formulation was used to predict the spatial distribution of the temperature, ice-phase volume fraction (related to frost density), and the rate of phase change within the frost layer. The time variation of the average frost density, frost thickness, and heat flux at the cold surface showed good agreement with the experimental data some distance downstream of the leading edge, provided the proper transport properties were used. Their results indicated that for frost temperatures between 264

and 272 K the local effective vapor mass diffusivity was up to seven times larger than the diffusivity of water vapor in air as expressed by Fick's law. They buttressed this finding by noting their results were comparable with data measured for water vapor diffusion in snow. Based on this formulation, Tao and Besant (1993) took the streamwise variation in frost properties into consideration, primarily caused by the profile of the thermal and concentration boundary layers, and they developed a transient, two-dimensional model for frost growth on a cold surface exposed to turbulent airflow.

Sherif *et al.* (1993) developed a semi-empirical model of the transient frost formation process on a flat plate under forced convection conditions. Based on empirical correlations for predicting the convective heat transfer coefficient and frost thermal conductivity and density, the model was numerically solved for the temperature and thickness of the frost, using the Lewis analogy to compute both the mass transfer coefficient and an enthalpy transfer coefficient.

Şahin (1994) made an experimental study of the frost formation on a horizontal plate during the crystal growth period. He reported that during the crystal growth period, frost formation was best characterized by linear crystal growth, and the vapor diffusion through the void portions of the frost layer was on the order of 10% of the total mass flux though the air boundary layer, except at very low plate temperatures. He also provided experimental results on the effects of plate temperature, air temperature, air humidity ratio, and Reynolds number on frost formation. In another work (Şahin, 1995), he developed an analytical model for frost formation during the crystal growth period. In this model, the frost layer was assumed to consist of cylindrical frost columns surrounded by moist air. He used the ice crystal density variation with temperature reported by cloud physicists to predict the density of frost columns.

Lee *et al*. (1997) developed an analytical model for the formulation of a frost layer on a cold flat surface by considering the molecular diffusion of the water vapor, and the heat generation due to the ablimation of water vapor in the frost layer, which was expressed in terms of water-vapor density and the absorption coefficient. In their model, the amount of water vapor absorbed in the frost layer was assumed to be proportional to the water-vapor density in the frost layer. Results from the model showed that frost thickness and the frost surface temperature increased with increasing air velocity and relative humidity; furthermore, the frost thickness underwent a relatively large change at the inlet of the flat plate, but there was little change if the air velocity was over 2 m/s.

Le Gall and Grillot (1997) presented a one-dimensional transient model based on a local volume-averaging technique to predict the frost growth and densification on a cold wall subjected to a moist air flow. The model required a good knowledge of the effective vapor mass diffusion occurring in the frost layer, which was several times larger than the molecular diffusion and had large uncertainties. The discrepancy might be because the effective diffusion in a frost layer accounted for a combination of complex physical mechanisms, such as a decrease in the effective cross-sectional area for diffusion and the tortuosity of the porous frost layer. In adjusting their model to match the experimental work, Le Gall and Grillot imposed a water-vapor transport that deviated significantly from that of Fickian diffusion. They correlated the deviations, via a so-called diffusion resistance factor, with the heat and mass boundary conditions and the rate of densification.

Mao *et al.* (1999) experimentally investigated frost growth on a flat, cold surface subject to a flow of subfreezing, turbulent, parallel, moist air. They found that the frost appeared to be smooth at warmer plate temperatures and lower air relative humidities, where the frost layer was thinner and denser compared to that forming at lower plate temperatures and higher air humidities. Similar to the work of Mao *et al.*(1992 and 1993), the frost growth characteristics were correlated as a function of time, distance from the leading edge, temperature ratio, humidity ratio, and Reynolds number. As a comparison to the experimental data, Chen *et al.* (1999) modified the numerical model presented by Tao *et al.* (1993) to simulate the frost growth for turbulent air flow over a rough frost-air interface.

Şahin (2000) numerically studied the effective thermal conductivity of frost for the crystal growth period, based on his earlier assumption that the frost structure was cylindrical columns surrounded by moist air. The model was one dimensional along the direction normal to the cold surface, and relied on the conservation of energy and mass. He ended up with a local effective frost thermal conductivity consisting of three terms: one term accounting for the effect of diffusion and sublimation of water vapor in the frost layer, a second term accounting for the conductivity of the frost columns, and a third term for the conductivity of the moist air around the columns. The application of this model is limited, because the assumed frost morphology may prevail only during the very short period of crystal growth.

Cheng and Cheng (2001) modified the model of Jones and Parker (1975) and the model of Sherif *et al.* (1993) to develop a theoretical model for frost formation on a cold plate placed in atmospheric air. The model could be used to evaluate environmental effects on the frost growth rate, such as plate surface temperature, and air velocity, temperature and humidity ratio. The predictions of the frost growth rate by the model agreed closely with the existing experimental data during the frost layer growth period for most of the cases considered.

Cheng and Shiu (2002) experimentally investigated the spatial variation of the frost thickness at the leading edge on a cold plate in moist airflow. Their experimental conditions covered air velocities from 2 to 8 m/s, air temperatures from 18 to 30 ˚C, air relative humidities from 40% to 70%, and plate surface temperatures from –18 to 0 ˚C. They observed that the frost formed a ‘round head’ and a ‘sharp head’ at the leading edge at lower and higher air velocities respectively. The variation of the frost thickness in the downstream region, however, was not observed.

Lee and Ro (2002) experimentally studied frost formation on a vertical plate in hydrodynamically and thermally developing flows that simulated the entrance region of a heat exchanger. They measured the time and spatial variation of frost thickness, mass, and density under different inlet air temperatures, inlet air humidities, air velocities, and cold surface temperatures. The data were represented by empirical correlations to be used as tools for predicting frost formation. The valid range of Reynolds numbers for their correlations was from 1000 to 3000, which represents the high end of the typical operating conditions for the type of heat exchangers targeted in this study.

Yun *et al.* (2002) developed a physical model of frost layer growth and frost properties with air flow over a flat plate at subfreezing temperature. They measured frost roughness, and formulated an empirical correlation for the average frost roughness. They used the modified Prandtl mixing-length approach, including the effects of frost roughness on the turbulent boundary layer, to calculate heat and mass transfer coefficients. Frost thermal

conductivity was determined by solving the combined equations of air equivalent conductivity, which incorporated the effect of flow structure generated by the roughness of the frost surface, and thermal conductivity of the frost inner layer. The model was used to estimate frost thickness, frost mass concentration, and frost density with time and space, and it showed good agreement with the basic trends of the data taken from other independent studies.

Cheng and Wu (2003) investigated frost formation on a cold plate in atmospheric air flow by means of experimental and theoretical methods. They used a microscopic imaging system to record the pattern and the thickness of the frost layer every five seconds during the early stage of the frost growth. They observed a multiple-step ascending frost growth pattern caused by the melting of frost crystals at the frost surface. Effects of velocity (2~13 m/s), temperature (20~35 ˚C) and relative humidity (40~80 percent) of the air, as well as the surface temperature of the cold plate (-13~-2 ˚C) were studied. Their work supported the theoretical model of Cheng and Cheng (2001) for predicting the frost growth rate during the frost layer growth period.

Lee *et al.* (2003) presented a mathematical model to predict the behavior of frost formation by simultaneously considering the air flow and the frost layer. They validated the model by comparing their model to several other analytical models. They stated that most of the previous models cause considerable errors, depending on the working conditions or the correlations used in predicting the frost thickness growth, whereas their model estimated the thickness, density, and surface temperature of the frost layer more accurately (within an error of 10%), except for during the early stage of frosting. Numerical results were presented for the variations of heat and mass transfer during the frost formation and for the behavior of frost layer growth along the direction of air flow.

Kwon *et al.* (2006) experimentally studied heat and mass transfer during the flow of humid air over a flat plate with cooling modules at the central region. They measured the local surface temperature of the plate, the local frost thickness, and the total frost mass on the plate. They found that the characteristics of the upstream airflow were very different from that of the downstream airflow.

1.2.1.2 Frost Growth in Geometries Simulating the Flow Path between Straight Heat Exchanger Fins

O'Neal and Tree (1984) measured the frost height and density during the frost layer full growth period (corresponding to a frost growth period up to 7 hours) in a parallel-plate geometry over a range of Reynolds number, air humidity, air temperature, and plate temperature. They developed a multiple regression correlation of the frost height as a function of time, Reynolds number, plate temperature, and humidity of the air stream for Reynolds numbers ranging from 4400 to 15900, which far exceeded the range of typical operating conditions for the type of heat exchangers targeted in this study. The frost growth was found to be independent of the Reynolds number for Re>15900.

Östin and Anderson (1991) experimentally investigated frost formation on parallel horizontal plates facing a forced air stream at varying temperatures, relative humidity, and air velocities. They found that both the plate surface temperature and the air relative humidity have important effects on the frost thickness, and frost density increases with relative humidity and is highly sensitive to air velocity. They used a dynamic one-strip method to determine the thermal conductivity. Two categories of frost formation were observed: monotonic and cyclic growth. In the former it was found that the condensed water vapor contributes in equal amounts to increases in the thickness and the density, while in the latter melting at the frost surface resulted in abrupt internal densification. They reported that the ratio of mass transfer contributing to the growth in frost thickness had an average value of 0.49.

Östin (1992) investigated the influence of frost formation on the heat exchanger surfaces based on experiments with moist air stream between parallel cooling plates, and developed a model for frost growth under forced airflow between parallel plates with separation distances of 8-12 mm. The model predicts the heat transfer coefficient, frost layer thickness, frost mass, and frost surface temperature as a function of time and position. The predicted results were not compared to experimental data, but the authors demonstrated the importance of considering frost formation in the optimization design of commercial plate heat exchangers.

Tao *et al.* (1994) experimentally studied the frost characteristics during the early growth period on single straight fins and on cold surfaces made of different materials. The authors presented information on the early stage of frost growth on various types of surfaces, and used the model reported by Tao *et al.* (1993) and modified by Tao and Besant (1993) to predict frost growth under operating conditions similar to those found in freezers.

Ismail and Salinas (1999) developed a one-dimensional transient model to simulate the process of frost formation on a flat cold surface subject to the flow of humid air. The numerical solution was based on a local-volume-averaging technique. The model was composed of two stages: the stage of one-dimensional crystal growth, and the stage of three-dimensional growth of the branching of ice crystals followed by steady growth. The precision of their numerical solutions was greatly dependent on the initial values of diffusivity, initial geometry of the ice crystals, a factor related to the flow turbulence, and the correlations for frost, ice, and air properties.

Storey and Jacobi (1999) conducted experiments to assess the influence of streamwise vortices on frost growth in a steady developing laminar channel flow. They employed a scaling relation to normalize the frost growth rate with respect to temperature, humidity, and time. They found that the data from baseline experiments in a rectangular channel were accurately correlated using the relation, and that the frost growth still followed the relation when streamwise vortices were introduced into the channel flow, but local growth rates were increased by more than 7% in regions where a surface-normal flow toward the frost surface was induced by the streamwise vortices.

Thomas *et al.* (1999) and Chen *et al.* (1999) developed a special test facility to characterize frost growth on straight heat exchanger fins under conditions similar to those experienced in freezers, *i.e.*, -10 to -20 ˚C air temperature, 80% to 100% air relative humidity, and -35 to -40 ˚C plate surface temperature. Their tests typically lasted 200 to 240 minutes, and the airflow was in the turbulent regime. They used a laser scanning system to measure the distribution of frost height on the fins, and a special pre-cut fin to measure the frost deposition mass along the airflow direction. They reported a rapid decrease in frost height along the direction from the fin base to fin tip, and a less rapid decrease in frost height and a small variation in mass concentration along the direction of airflow. They also provided heat transfer rate and air pressure drop data in the work.

Andreas and Beer (2000) experimentally and theoretically studied the frost formation on cold parallel plates in laminar moist airflow. They measured the temporal and spatial variation of the frost layer thickness under various combinations of air velocity, air temperature, air humidity ratio, and plate temperature. They also simulated the frost formation process numerically, using a two-dimensional transient model based on the conservation of mass, momentum, energy, and species. Two sets of governing equations for the two subdomains – the air stream and the frost layer – were coupled by the boundary conditions at the moving interface, and solved iteratively.

1.2.1.3 Frost Growth on Other Simple Geometries

Chung and Algren (1958) experimentally and theoretically studied the effect of frost formation on the heat transfer between a humid air flow and a cylinder. Their theoretical analysis of the heat and mass transfer processes was made using existing solutions of boundary layer equations and the heat and mass transfer analogy.

Chen and Rohsenow (1964) presented an experimental and theoretical study of the heat, mass, and momentum transfer in a frosted tube. They found that the behavior of the frosted tube was largely determined by the surface roughness of the frost layer, and they performed heat transfer and pressure drop calculations based on a predicted roughness as functions of ($RePrk/k_f$) and the frost thickness.

Parish and Sepsy (1972) combined numerical solutions to the boundary layer equations (momentum, energy, species, and continuity equations) with a simple model for frost density and conductivity to predict frost formation around a cylinder. They showed that the use of analytical or empirical correlations based on an isothermal surface could result in significant errors under frosting conditions.

Schneiger (1978) experimentally investigated the frost growth around a cylindrical tube for periods of up to 8 hours, with various air temperatures, relative humidities, air velocities, and tube surface temperatures. They found that the frost thickness was independent of the variables commonly significant during mass transfer, such as the Reynolds number and the vapor pressure difference. He used a simple model of a frost needle and considered some other factors, such as the mass transfer rate as a function of the ratio of supersaturation, and frost surface melting and refreezing at an air temperature above 0 ˚C. Based on these considerations, they developed a correlation that related the frost thickness as a function of time, tube surface temperature, and frost surface temperature.

Marinyuk (1980) experimentally studied the effect of frost formation around a cylinder on the natural convective heat transfer between the cylinder and the surrounding air. They concluded that frost formation under natural convection conditions did not increase the convective heat transfer coefficient in comparison with the dry state. Their investigation on frost thermal conductivity showed that it is strongly dependent on the formation temperature.

Padki *et al.* (1989) formulated a simple model to predict the frost growth rate, frost thickness, and surface temperature for frost formation in different geometries. The model utilized known convective heat transfer correlations for different geometries and the Lewis analogy to determine the mass transfer coefficient. They also suggested a method to adjust the frost density when melting-and-refreezing occurred on the upper frost layer.

Ismail *et al.* (1997) presented a transient two-dimensional model for frost growth around a cylinder in moist air that could predict local variables such as velocity, temperature, and frost properties. The model was composed of two-dimensional momentum, energy, and continuity equations for the flow field, and one-dimensional, two-stage equations for the frost layer (similar to Tao *et al.* 1993).

Sengupta *et al.* (1998) experimentally investigated frost formation on a circular cylinder with a cross flow of moist air and developed empirical correlations for the frost thickness and heat transfer coefficient. The correlations were as functions of non-dimensional parameters representing the free-stream velocity, humidity, temperature, and time.

Lee and Ro (2001) experimentally studied frost formation on a horizontal cylinder under cross flow and presented the effect of free stream air temperature and humidity on the thickness, effective thermal conductivity, and

effective thermal resistance of the frost layer. They found that in all cases, frost layers formed on the front and rear surfaces were thicker than those on the top and bottom surfaces.

Huang (2002) numerically solved a transient inverse geometry heat conduction problem (shape identification problem) to estimate the irregular frost thickness and shape on the outside surface of a circular tube, based on temperature readings taken at appropriate locations and times on the tube surface. The solution used an inverse algorithm based on the conjugate gradient method and the boundary element method. The effects of reducing the number of sensors and increasing the measurement uncertainties on the inverse solutions were discussed.

1.2.2 Frost Growth on Finned Tube Heat Exchangers

Several reports are available for the more complex geometries of finned tube heat exchangers, but very little has been published to address frost formation on louvered-folded-fin, flat-tube heat exchangers. Kondepudi and O'Neal (1987) provided a literature review on the effects of frost growth on extended surface heat exchanger performance. They focused on four important performance variables: fin efficiency, overall heat transfer coefficient, pressure drop, and surface roughness. Some general conclusions included that frost growth is detrimental to heat exchanger performance, and the pressure drop is a more influential parameter under frosting condition. They mentioned that a generalized and reasonably accurate correlation between the overall heat transfer coefficient, the geometry of the heat exchanger coils, and the varying environmental conditions would be very useful.

1.2.2.1 Frost Formation on Other Types of Heat Exchangers

Some early research on the effects of frost formation on heat exchanger performance includes that of Stoecker (1957 and 1960), Gates *et al.* (1967), and Huffman and Sepsy (1967). Gatchilov and Ivanova (1979) experimentally investigated the characteristics of frosting on finned air coolers, with attention to the influence of the air flow properties. Fisk *et al.* (1985a) conducted some research on the onset of freezing in residential air-to-air heat exchangers, and Fisk *et al.* (1985b) compared the performance of two residential air-to-air heat exchangers (a cross-flow and a counter-flow) with respect to temperature efficiency, defrost fraction, and rate of change in mass flow rate under conditions with freezing and periodic defrosts. Miller (1987) conducted an analysis of frosting and defrosting effects on the seasonal efficiency for an air-to-air heat pump with 14 fins per inch, and reported better seasonal efficiency than the 90- and 45-minute time-temperature controls if the heat pump was operating with a demand-defrost control (based on a set value of air pressure drop). Smith (1989) conducted theoretical calculations for cooling coils working at freezer temperatures, and found a low limit on coil surface temperature to avoid unfavorable coil frosting characteristics.

Huffman and Sepsy (1967) experimentally investigated the heat transfer and pressure loss in extended-surface, round-tube heat exchangers operating under frosting conditions; a non-dimensional heat transfer parameter (average Colburn j factor over initial j factor) was correlated with a non-dimensional mass transfer parameter ($[w_u - w_s]/w_s$, where w_u is the upstream humidity ratio, and w_s is the saturated humidity ratio at the temperature of outside tube wall). A non-dimensional pressure loss parameter (average friction factor over initial friction factor) was correlated with the non-dimensional mass transfer parameter and a dimensionless time parameter (Dt/D_h^2, where D is the mass diffusivity of water vapor in air, t is time, and D_h is the hydraulic diameter). The heat transfer coefficient in their j factor was one that combined both air and frost resistance, and it was reasonable for the authors to argue

that the heat transfer coefficient was dependent on the driving potential of mass transfer, which explained the way they correlated the heat transfer data. However, there was no strong support for the way they correlated the friction factor. Their experimental results were used by Tantakitti and Howell (1986) to simulate the outdoor coil of air-to-air heat pumps operating under frosting conditions.

Neiderer (1976) experimentally studied frosting and defrosting on finned-tube heat exchangers with fin spacings from 2 to 6 fins per inch, including cases with variable fin spacing. He reported that when operating under identical conditions with the same amount of frost accumulation, a heat exchanger with smaller fin spacing was more severely affected than one with larger fin spacing with respect to the air flow. Heat exchangers with a variable fin spacing showed significant improvement in comparison to those with a conventional uniform fin spacing. He also reported that during the defrost cycles, only 15% to 25% of the heat required to defrost was actually used to melt the frost.

Based on a simplified analysis of a frosted fin, Barrow (1985) stated that the insulation resistance of frost was negligible when frost grew on the fin surface of the evaporator coil of a heat pump. He provided an expression for frosted-fin efficiency, but did not provide the derivation of the expression from the basic governing equation for the temperature distribution in a frosted fin. The validity of the expression is questionable, and hence impacts the credibility of the conclusions derived from the expression.

Kondepudi and O'Neal (1989) experimentally investigated the effects of frost growth on the performance of heat exchangers with louvered fins and round tubes. They presented frost mass, pressure drop across the heat exchanger, and energy transfer coefficient based on the logarithmic mean enthalpy difference (LMED), as they depend on air humidity, face velocity, and fin spacing. They found that the amount of frost accumulation, pressure drop, and energy transfer coefficient were higher under higher humidity, higher face velocities, and smaller fin spacing. They reported that the overall energy transfer coefficient dropped as frost accumulated on the heat exchanger.

Emery and Siegel (1990) described a series of experiments to measure the effects of frosting when subfreezing air passed through a finned, round-tube heat exchanger with a fin spacing of 6.35 mm. They found that the thermal performance was a function of time and specific humidity levels, while the pressure drop was a function only of the frost thickness and surface roughness.

Kondepudi and O'Neal (1993) developed an expression of fin efficiency for pin fin heat exchangers under frosting conditions. Importantly, in order to derive their expression for fin efficiency, they assumed there was no heat transfer in the frost layer along the direction of fin length; however, they did not quantify how much difference it would make if the heat transfer in that direction was considered.

In order to improve the performance of heat exchangers under frosting conditions, Ogawa *et al.* (1993) proposed a method of mitigating frost formation at the leading edges of fins and guiding fresh air to the downstream portions of the heat exchanger. To accomplish this redistribution of frost, they used front fin staging (wider fin spacing at the entrance face of the heat exchanger), side fin staging (wider fin spacing in the airflow direction by arranging fins of different sizes or by cutting away parts of the fins), and partial cutting of fins. Their method was

experimentally proved to be effective in decreasing air pressure drop and increasing the heat transfer rate under conditions corresponding to heavily frosted heat exchanger surfaces.

Chen *et al.* (2000a and 2000b) developed a numerical model for predicting frost growth on plate-fin heat exchangers with turbulent air flow at a constant flow rate for conditions typical to those of refrigeration. The model combined the transient one-dimensional governing equations for frost layer as a porous medium, and the transient two-dimensional heat conduction in the fins. The model produced acceptable predictions for frost height, density, and heat transfer rate, but model predictions of the pressure drop across a heat exchanger were not very successful, because of the extreme sensitivity of the pressure drop to frost height. Small errors in predicting frost height could result in relatively much larger errors in predicting pressure drop. In Chen *et al.* (2003), they modified the model to simulate a fan-supplied heat exchanger. They showed that coupling an accurate frost model for finned surfaces with selected fan performance curve would be essential for the optimal design of refrigeration heat exchangers. They also demonstrated the variation in the frost growth time (time between defrosts) with different selections of the fan type, fin spacing, and fin thickness.

Watters *et al.* (2001a and 2001b) conducted experiments with three two-row round-tube heat pump evaporators to determine whether fin staging would improve frosting and defrosting performance under standard test conditions and heavily frosted conditions. The baseline coil had a uniform fin pitch of 20 fins per inch, while the other two coils had a fin pitch of 15 fins per inch on the front row, and 20 and 25 fins per inch on the second row, respectively. They reported that the staged coils produced a moderate improvement in COP, and a significant improvement in frost cycle time.

Wu and co-workers (2001) obtained heat transfer, pressure drop, and frost thickness measurements for a plain-fin-and-tube heat exchanger. The heat exchanger was eight rows deep. They observed the distribution of frost and developed a model to predict performance under frosting conditions.

Mago and Sherif (2002) formulated a method to calculate the air flow path on an industrial-sized, finned-tube, multi-row coil operating under frosting conditions. They correlated the air flow path with the prevailing psychrometric conditions in the freezer, and used this information to identify the location in the coil where the moist air reached supersaturated conditions. Entering the supersaturated zone was identified as the demarcation between forming an unfavorable ‘snow-like’ frost and the more traditional and more favorable frost formation patterns. They employed the enthalpy driving potential to calculate the overall heat transfer coefficient based on the enthalpy difference, but their method for computing the fin efficiency neglected heat transfer in the frost layer parallel to the length of the fin.

Yan *et al.* (2005) experimentally investigated the performance of frosted finned-tube heat exchangers with plain fins, single-bank louvered fins, and multi-louvered fins. They discussed the effects of the air flow rate, the air relative humidity, the refrigerant temperature, and the fin type on the thermal-hydraulic characteristics of the heat exchangers. They found that under frosted-surface conditions, the heat transfer rate, the overall heat transfer coefficient, and the pressure drop for multi-louvered fins were higher than the others.

1.2.2.2 Frost Formation on Louvered-Folded-Fin, Flat-Tube Heat Exchangers

Itoh *et al.* (1996) experimentally studied the effect of air-side configurations on the thermal-hydraulic performance of microchannel heat exchangers during frosting. They investigated the pressure drop, the flow rate,

and the heat transfer rate of three different heat exchangers, of which two had fins that protruded in the front of tubes. Their experiments were conducted at inlet air dry-bulb, wet-bulb and refrigerant temperatures of 2 ˚C, 1 ˚C and –8 ˚C, respectively, with R-22 as the refrigerant. They concluded that the significant changes in the air-side configuration were required in order to use the microchannel heat exchangers in heat-pump applications.

Kim and Groll (2002) studied the performance of microchannel heat exchangers as an outdoor coil under frosting and defrosting conditions, and they discussed the effects of using different fin orientation and spacing on the system heat transfer rates, capacity, power consumption, efficiency, and frosting and defrosting times. However, the air-side thermal-hydraulic data and quantities of frost and water retention were not provided.

1.2.3 Other Research Related to Frost Growth

The effects of chemical, physical, and electrical surface treatments and electric field effects on frost growth have been of particular interest over the past few years. Work addressing the effects of surface energy (surface treatments) on frost formation and defrost includes that of Östin and Johannesson (1991), O'Neal *et al.* (1997), Dyer *et al.* (2000), Hoke *et al.* (2000), Okoroafor and Newborough (2000), Wu and Webb (2001), Jhee *et al.* (2002), Na and Webb (2003), and Shin *et al.* (2003). Related experimental work to study vibration effects on frost formation and frost release (Wu and Webb, 2001, and Cheng and Shiu, 2003), and the influence of electric field effects on frost formation (Wang *et al.*, 2004) has also been reported.

1.2.4 Summary

It is widely accepted that a common frost formation process includes a crystal growth (or early growth) period, and a frost layer growth (or mature growth) period. Under the conditions common to heat-pump and refrigeration applications, the frost layer growth period begins at roughly the 5^{th} minute, and spans up to 1 to 2 hours. During this period, frost columns generated in the crystal growth period branch out to form a more uniform frost layer. Often, the early growth period is preceded by a condensation period, and the frost layer growth period will be followed by a frost layer full growth period, during which the frost-layer shape does not change until melting occurs on the frost surface.

Most work on frost properties has been conducted experimentally, and a range of experimental methods have been used to obtain the frost thickness, frost density, thermal conductivity, surface temperature, and heat flux. Many researchers reported that the frost density and thermal conductivity are related, and these are perhaps the two most important properties to thermal-hydraulic performance. Some researchers have suggested that in addition to frost density, other factors such as the average frost temperature and vapor sublimation-diffusion-ablimation inside the frost layer, could also influence the effective thermal conductivity. O'Neal (1985) pointed out that the macroscopic structure of frost layer, *i.e.* the crystal orientation and the shape of the frost crystals, "would potentially affect the thermal conductivity and/or density," and this viewpoint is now widely held. When melting and refreezing occurs at a frost surface that reaches a temperature of 0 ˚C, the structure of the frost layer becomes even more complex. These phenomena might explain the wide variation in the density and thermal conductivity predicted by the simple correlations developed in earlier work. However, the complex structure of a frost layer is not easily measured or described, and a universally applicable correlation based on generalized "structural" parameters is not currently available. Although some extant work, such as Dietenberger (1983), provides theoretical expressions for

thermal conductivity based on a simplified model of frost structure, the accuracy of this approach depends on how well the structural parameters in the model represent the real frost structure, and how accurately those parameters are determined from the experimental data. Therefore, wherever a frost property is needed, generalized correlations developed from experimental data are widely (and almost blindly) adopted, sometimes with too little care directed toward choosing a correlation appropriate for the particular parameter space.

Many empirical and theoretical models have been developed to predict frost growth in simple geometries. The methodologies can be roughly divided into two types: one relies on solving the boundary layer equations for continuity, momentum, energy, and species, while updating frost layer properties using empirical correlations; the other type focuses on the growth of the frost layer, while quantifying the heat and mass transfer using correlations and the analogy between convective heat and mass transfer. The first type may not be well suited for application in complex geometries. The second type, which is more commonly used, faces problematic issues of how to solve the vapor diffusion and/or ice-phase continuity equations inside the frost layer–the solution requires good knowledge of the effective water vapor diffusion inside the frost layer, as well as the initial values of parameters such as the void fraction or the initial size of frost nuclei.

As to the effects of frost growth on extended surfaces and heat exchangers, it is commonly reported that frost formation is detrimental to heat exchanger performance, because it causes increased pressure drop across the heat exchanger, reduced air flow, and decreased heat transfer. Although some investigators observed an initial increase in heat transfer, which was attributed to the increased surface area and surface roughness upon the onset of frosting, the effect is so limited in duration and magnitude that its value in application is probably insignificant.

Among the experimental work evaluating heat exchanger performance under frosting conditions, it is surprising to note that reported values for UA are commonly based on the logarithmic mean temperature difference (LMTD), despite the fact that for simultaneous heat and mass transfer an overall energy transfer coefficient HA based on the logarithmic mean enthalpy difference (LMED) is more appropriate. Only a few studies report the overall energy transfer coefficient. It should also be mentioned that, with appropriate modifications for mass transfer, it is possible to formulate a rigorously appropriate UA-LMTD approach. A similar gap in the literature exists with respect to frosted fin efficiency. Some of the existing models are simple extensions of the fin efficiency for an unfrosted fin; others are based on energy balances, neglecting heat transfer in the frost layer along the direction of fin length. No empirical results have been reported to validate the existing expressions, and longitudinal conduction in a frosted fin can be important. More accurate expressions for frosted-fin efficiency can be developed by modeling heat transfer in the frost layer. Finally, when it comes to comparing heat exchanger performance, metrics more complete than overall heat or energy transfer coefficients and the pressure drops (and their dimensionless representations) are needed to fully characterize system impact.

1.3 Objectives

Research is necessary to study the thermal-hydraulic performance of folded-louvered-fin, microchannel heat exchangers under frosting conditions, with the following specific objectives:

1) Design an experimental apparatus, test procedure, and data interpretation method to study frost accumulation effects on louvered-fin, microchannel heat exchangers. In particular, rational and generalized

measures of the air-side convective heat transfer coefficient and pressure drop, represented as Colburn *j*-factor and friction factor, respectively, are needed. There are three main tasks to reaching this objective: the first is to tailor an experimental approach for obtaining thermal-hydraulic performance data under frosting conditions; the second is to develop a more accurate and generalized expression for frosted-fin efficiency; the third is to rigorously formulate and compare the *UA*-LMTD and *HA*-LMED methods to determine which is preferred (or propose an alternative).

2) Obtain heat transfer and pressure-drop data for a range of louvered-fin designs, which can be used as a basis for developing design guidelines and correlation development. Using these data, heat exchanger performance can be assessed, considering such criteria as the defrost cycle, and *j* and *f* under frosted conditions. In a qualitative sense, the data will provide early design guidance; quantitatively, they might yield (along with the other very limited data already available) a generalized method for predicting the effect of frost growth on *j* and *f* factors. In particular, it might be possible to develop frosted-surface multipliers that are a function of the nondimensional frost thickness (and thus an indirect function of environmental conditions and time) for each heat exchanger.

3) Formulate a model to predict the transient performance of folded-louvered-fin heat exchangers under frosting conditions. The model can use as a basis the correlations developed from the experimental data. It will require a method for predicting the outlet humidity and frost properties. It can also rely on temporal discretization, marching the heat exchanger along the frosting process.

Completion of this work will advance our understanding of frosted-surface heat exchanger performance in general, the folded-fin microchannel heat exchanger in particular and will provide a useful simulation of the transient performance of a heat exchanger that can be used for design and generalized for other geometries.

Chapter 2. An Exact Solution to Steady Heat Conduction in a Two-Dimensional Slab on a One-Dimensional Fin

Nomenclature

B_i	Biot number, as defined by Eqn. (2.1)
h	convective heat transfer coefficient ($Wm^{-2}\,ºC^{-1}$)
k	thermal conductivity ($Wm^{-1}\,ºC^{-1}$)
L	fin length; half the distance between tubes, see Figure 2.1 (m)
M	dimensionless group defined in Eqn. (2.17)
R	ratio of thermal resistance defined by Eqn. (2.2)
t	half fin thickness , see Figure 2.1 (m)
T	temperature (ºC)

Subscripts and Superscripts

1	in the material of the fin
2	in the material of the frost
b	at the fin base
e	in the environment
B	per Barker (1958)

Greek Symbols

δ	frost thickness (m)
ε	a small parameter, see Equation (2.10)
η	fin efficiency, see Equation (2.27)
η'	fin efficiency approximation, from a one-term approximation, see Equation (2.35)

2.1 Introduction

This work is motivated by a desire to have a convenient expression for fin efficiency, spanning operating conditions which cause frost to form on the air-side surface of a heat exchanger (in particular, flat-tube heat exchangers with constant-area fins). Using an effective conductivity for the frost, the frost and fin material can be considered as a composite medium. Although the study was directed at the problem of frost on a metallic fin, the mathematical analysis is presented in a general fashion and is applicable to a wide range of related problems.

Exact solutions for heat conduction in composite slabs have been provided by several authors. Tittle (1965) formulated a one-dimensional orthogonal expansion for composite media, and Padovan (1974) developed a general procedure for solving Sturm-Liouville problems arising from transient heat conduction in composite and anisotropic domains. Using a Green's function approach, Huang and Chang (1980) provided exact solutions for unsteady, periodic, and steady conduction in composites of infinite, semi-infinite, and finite laminates. Feijo *et al.* (1979) analytically solved for temperature distributions in a composite fin for a slab with a symmetric internal heat source. Yan *et al.* (1993) obtained series solutions for three-dimensional temperature distributions in two-layer composites, for a range of boundary conditions. Aviles-Ramos *et al.* (1998) provided an exact solution to the temperature distribution in a two-layer body: one orthotropic and the other isotropic. In most cases, the two- or three-dimensional solution converges slowly, and the computation can be difficult.

More closely related to the current work, the analytical solution for heat conduction in a composite fin under the usual conditions of constant heat transfer coefficient and uniform ambient temperature has also been studied. Barker (1958) considered a two-layer composite, and obtained an analytical solution for the two-dimensional temperature distribution within the fin and the coating material. Chu *et al.* (1983) used the Laplace transform and eigenfunction expansions to analyze transient conduction in a composite fin. The resulting expressions were complex, and the inverse transform was difficult to find. The complexity in these two solutions—

that of Barker and that of Chu *et al.*—would be much reduced if one-dimensional heat conduction prevails within one of the two slabs. In a recent study, Mokheimer and co-workers (1997) considered a one-dimensional slab on a two-dimensional fin and obtained numerical and analytical solutions for heat conduction in the composite. They did not explore the limitations of their analysis or assess the potential effects of transverse temperature gradients in a two-dimensional slab.

An exact solution for a two-dimensional slab on a one-dimensional fin has not appeared in the open literature, nor has the applicability of such an approximation been explored for cases such as the one of interest. For most heat exchangers operating under frosting conditions, the fin is thinner than the frost, and both the fin and frost thicknesses are much smaller than the fin length. Furthermore, the frost thermal conductivity is much smaller than the fin conductivity (less than 1% for an aluminum fin). Thus, it is expected that in some cases it will be appropriate to simplify the problem to a two-dimensional slab on a one-dimensional fin; moreover, such an approach is anticipated to yield simpler expressions for temperature and fin efficiency than the case of a two-dimensional slab on a two-dimensional substrate.

In this chapter, a numerical solution to conduction within the composite medium comprised of a fin and coating material is used to conduct a parametric study of the effects of geometry, thermal conductivity of the fin and coating material, and convection coefficient on the temperature profiles. In particular, the applicability of assuming a one-dimensional fin with a two-dimensional coating is explored. Next, the exact solution under the assumption of one-dimensional heat flow in the fin and two-dimensional heat flow within the coating is obtained by the method of separation of variables—an unusual eigenvalue problem is obtained, for which a new scalar product is defined for orthogonality. The new solution converges rapidly and its eigenvalues are easily calculated. The exact solution is useful in gaining physical insights into the problem, and it is simple, accurate, and less costly to use than numerical solutions. Furthermore, it will be shown that for many cases, such as for frost on a metallic fin, a simple one-term approximation is often valid. Using the one-term approximation, a simple expression for fin efficiency is developed, and this expression is much easier to use than a computational model of the system.

2.2 Problem Description

The physical situation of interest, frost on a metallic fin is shown in Figure 2.1(a), where a frosted, flat-tube heat exchanger with constant-area fins is shown in the schematic. The fin depth in the z-direction is large in comparison to lengths in the x- and y-directions. Because temperatures, geometry, and properties in the z-direction are constant, a two-dimensional analysis is used. The dashed box, enlarged in Figure 2.1(b), shows in more detail the physical system to be analyzed. The metallic fin and the frost slab form a composite medium. The convection coefficient, free-stream temperature, base temperature, and thermophysical properties are considered as constant. The latent heat effect at the frost surface can be accounted for by absorbing it into the convective transfer coefficient, as explained in more detail later (in Chapter 3 and Appendix B).

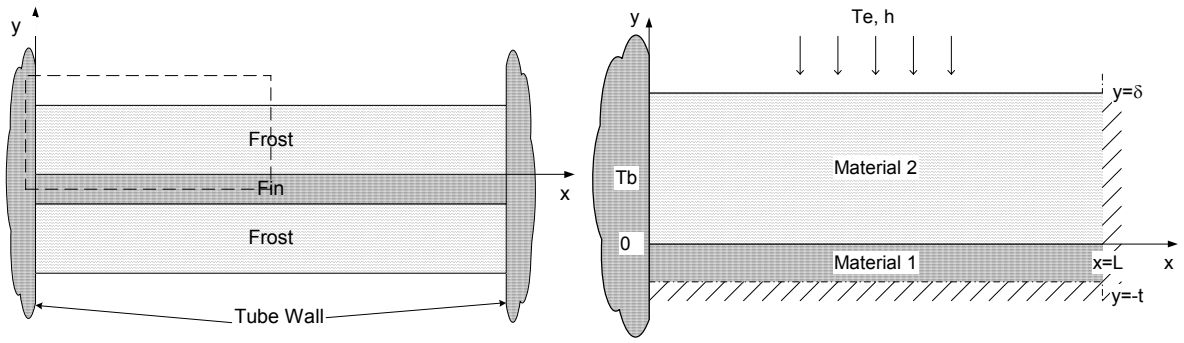

Figure 2.1 Schematic of the composite slab, with the one-dimensional fin Material 1, and the two-dimensional slab Material 2: (a) the complete physical system, showing a fin between two flat tubes, and (b) simplified system from symmetry.

2.3 Numerical Parametric Analysis

The problem of two-dimensional heat flow both for the fin and coating material is solved numerically using well-known finite-difference methods. Consider a Biot number defined as the ratio of internal conduction resistance to the external convection resistance, namely

$$Bi = \frac{h\delta}{k_2}\left(1+R\right) \quad , \tag{2.1}$$

where R is the ratio of the transverse thermal resistance of the fin material (t/k_1A, where A is an arbitrary area) to that of the coating material (δ/k_2A), i.e

$$R = \frac{t/k_1}{\delta/k_2} \quad . \tag{2.2}$$

Although somewhat arbitrary, it was assumed that one-dimensional conduction prevailed if the maximum temperature difference between the outer and inner surfaces was less than 5% of the maximum temperature difference, i.e.,

$$\max_{0\le x\le L}\left|T_1(x,0)-T_1(x,-t)\right| < 5\%\left|T_e-T_b\right|$$

or (2.3)

$$\max_{0\le x\le L}\left|T_2(x,0)-T_2(x,\delta)\right| < 5\%\left|T_e-T_b\right| \quad ,$$

The geometries of the composite slab (L, t and δ), the base and ambient temperature (T_b and T_e), and the convective heat transfer coefficient h, were fixed, in order to study the temperature profiles within the two slabs under different combinations of k_1 and k_2 (or B_i and R). The results of this wide-ranging numerical study are provided in Table 2.1: it gives the parametric range for a valid one-dimensional approximation in either or both slabs. The decision on validity is based on Equation (2.3). As an example case, consider Bi=10, and t=δ=0.1L, then the table shows that an approximation of a one-dimensional fin with a two-dimensional coating is appropriate when $0<R<0.2$, or when $32<R<63$.

From the results provided in Table 2.1, the following conclusions are drawn: when $B_i < 0.05$, heat conduction within the fin and the coating can both be approximated as one-dimensional in x, for the entire geometrical range studied. For almost all cases in the table, if $B_i > 0.05$, then when $R < 0.1$ the fin can be approximated as one-dimensional, with a two-dimensional coating. This situation represents the parametric range of most importance for frost on a metallic fin. The case of a two-dimensional substrate, with a one-dimensional coating occurs when the fin is thicker than the coating and R is within a certain region (depending on the geometries); however, such cases are not common for the application that motivates this study.

Table 2.1 Temperature profile behavior, under the criteria of Equation (2.3), for different combinations of B_i and R

B_i	Geometry t, δ, L	Required R for the modeling approach designated			
		1-D fin; 1-D coating	1-D fin; 2-D coating	2-D fin; 1-D coating	2-D fin; 2-D coating
<0.05	$t=\delta=0.1L$	(0, ∞)	-	-	-
0.1	$t=\delta=0.1L$	(~0.35, ∞)	(0, ~0.35)	-	-
1.0	$t=\delta=0.1L$	(~6.5, ∞)	(0, ~6.5)	-	-
1.45	$t=\delta=0.1L$	(~9.0, ∞)	(0, ~1.15) ∪ (~1.85, ~9.0)	-	(~1.15, ~1.85)
10	$t=\delta=0.1L$	(~63, ∞)	(0, ~0.25) ∪ (~32, ~63)	-	(~0.25, ~32)
∞	$t=\delta=0.1L$	(~$6.3B_i$, ∞)	(0, ~0.25) ∪ (~$3.2B_i$, ~$6.3B_i$)		(~0.25,~$3.2B_i$)
<~0.05	$t=0.1\delta=0.01L$	(0, ∞)	-	-	-
0.1	$t=0.1\delta=0.01L$	(~0.01, ∞)	(0, ~0.01)	-	-
1.0	$t=0.1\delta=0.01L$	(~5.4, ∞)	(0, ~5.4)	-	-
10	$t=0.1\delta=0.01L$	(~63, ∞)	(0, ~63)	-	-
100	$t=0.1\delta=0.01L$	(~630, ∞)	(0, ~630)	-	-
∞	$t=0.1\delta=0.01L$	(~$6.3B_i$, ∞)	(0, ~$6.3B_i$)	-	-
<~0.05	$\delta=0.1t=0.01L$	(0, ∞)	-	-	-
0.1	$\delta=0.1t=0.01L$	(~0.7, ∞)	(0, ~0.7)	-	-
1.0	$\delta=0.1t=0.01L$	(~370, ∞)	(0, ~0.4)	(~10, ~370)	(~0.4, ~10)
10	$\delta=0.1t=0.01L$	(~4,400, ∞)	(0, ~0.18)	(~58, ~4,400)	(~0.18, ~58)
100	$\delta=0.1t=0.01L$	(~44,000, ∞)	(0, ~0.16)	(~330, ~44,000)	(~0.16, ~330)
∞	$\delta=0.1t=0.01L$	(~$440B_i$,∞)	(0, ~0.16)	(~$3.3B_i$, ~$440B_i$)	(~0.16, ~$3.3B_i$)
<~0.05	$\delta=t=0.01L$	(0, ∞)	-	-	-
0.1	$\delta=t=0.01L$	(~0.2, ∞)	(0, ~0.2)	-	-
1.0	$\delta=t=0.01L$	(~3.6, ∞)	(0, ~3.6)	-	-
3.5	$\delta=t=0.01L$	(~11.0, ∞)	(0, ~1.4) ∪ (~2.8, ~11.0)	-	(~1.4, ~2.8)
10	$\delta=t=0.01L$	(~29, ∞)	(0, ~0.65) ∪ (~15, ~29)	-	(~0.65, ~15)
∞	$\delta=t=0.01L$	(~$2.7B_i$, ∞)	(0, ~0.45) ∪ (~$1.7B_i$, ~$2.7B_i$)	-	(~0.45, $1.7B_i$)

2.4 Analytical Solution for the Two-Dimensional Slab on a One-Dimensional Fin

In consideration of the motivating problem, the following assumptions are invoked: steady-state, two-dimensional conduction in a slab on a one-dimensional fin, with no internal generation, and constant properties. The frost layer is assumed to be of uniform thickness. The base temperature is held at T_b, and there is no contact resistance between the frost and the fin. With these assumptions, the fin temperature T_1 is a function of x only, and the frost temperature is $T_2(x,y)$. The governing equation for the temperature distribution along the fin, material 1, is

$$k_1 t \frac{d^2 T_1}{dx^2} + k_2 \left. \frac{\partial T_2}{\partial y} \right|_{y=0} = 0 \qquad \text{in } 0 < x < L \,. \tag{2.4}$$

The diffusion equation in the frost layer, material 2, is

$$\frac{\partial^2 T_2}{\partial x^2} + \frac{\partial^2 T_2}{\partial y^2} = 0 \qquad \text{in } 0 < x < L \,,\ 0 < y < \delta \,. \tag{2.5}$$

Equations (2.4) and (2.5) are subject to the following boundary conditions:

$$\left. \frac{dT_1}{dx} \right|_{x=L} = 0 \ , \ \left. \frac{\partial T_2}{\partial x} \right|_{x=L} = 0 \tag{2.6a}$$

$$T_1(0) = T_b \ , \ T_2(0, y) = T_b \tag{2.6b}$$

$$T_1(x) = T_2(x, 0) \ , \text{ and} \tag{2.6c}$$

$$\left. \frac{\partial T_2}{\partial y} \right|_{y=\delta} = \frac{h}{k_2} \left(T_e - T_2(x, \delta) \right) \ . \tag{2.6d}$$

Combining Equations (2.4)-(2.6), we obtain the four boundary conditions for $T_2(x,y)$:

$$\left. \frac{\partial T_2}{\partial x} \right|_{x=L} = 0 \ , \tag{2.7a}$$

$$T_2(0, y) = T_b \ , \tag{2.7b}$$

$$k_1 t \left. \frac{\partial^2 T_2}{\partial x^2} \right|_{y=0} + k_2 \left. \frac{\partial T_2}{\partial y} \right|_{y=0} = 0 \ , \text{ and} \tag{2.7c}$$

$$\left. \frac{\partial T_2}{\partial y} \right|_{y=\delta} = \frac{h}{k_2} \left(T_e - T_2(x, \delta) \right) \ . \tag{2.7d}$$

Now, we define the dimensionless variables as

$$\theta = \frac{T_2 - T_e}{T_b - T_e}, \quad x^* = \frac{x}{L}, \text{ and } \quad y^* = \frac{y}{\delta} \,. \tag{2.8}$$

After changing variables, the boundary value problem for $T_2(x,y)$ is

$$\frac{\partial^2 \theta}{\partial x^{*2}} + \frac{L^2}{\delta^2} \frac{\partial^2 \theta}{\partial y^{*2}} = 0 \qquad \text{in } 0 < x^* < 1,\ 0 < y^* < 1, \text{ with} \tag{2.9}$$

$$\frac{\partial \theta}{\partial x^*} = 0 \qquad \text{at } x^* = 1 \ , \tag{2.10a}$$

$$\theta = 1 \qquad \text{at } x^* = 0 \ , \tag{2.10b}$$

$$\frac{k_1 t}{L^2} \frac{\partial^2 \theta}{\partial x^{*2}} + \frac{k_2}{\delta} \frac{\partial \theta}{\partial y^*} = 0 \qquad \text{at } y^* = 0 \ , \text{ and} \tag{2.10c}$$

$$\frac{\partial \theta}{\partial y^*} + \frac{h\delta}{k_2} \theta = 0 \qquad \text{at } y^* = 1 \ . \tag{2.10d}$$

From this point forward, the "*" superscript will be dropped from the spatial coordinates for convenience, with x and y taken as dimensionless unless otherwise noted. Notice that the boundary condition (2.10b) conflicts with (2.10d) at $(x,y)=(0,1)$. In order to remove the singularity, replace (2.10b) with the following at $x=0$:

$$\theta = f(y) = \begin{cases} 1, & 0 \le y < (1-\varepsilon) \\ 1 - \dfrac{\left[y-(1-\varepsilon)\right]^2}{\left[(2\varepsilon k_2 / h\delta) + \varepsilon^2\right]} & (1-\varepsilon) \le y \le 1 \end{cases} , \tag{2.10e}$$

where $0<\varepsilon<<1$. We have $(\partial\theta/\partial y)_{(0,1)} + (h\delta/k_2)\theta(0,1) = 0$ and Equation (2.10e) → Equation (2.10b) as $\varepsilon \to 0$. Moreover, $f(y)$ is twice differentiable on $0 \le y \le 1$. The boundary condition at $x=0$ can be generalized to be any twice-differentiable function $f(y)$ on $0 \le y \le 1$. Because only the boundary condition given by Equation (2.10e) is nonhomogeneous, separation of variables is pursued. That is, assume

$$\theta(x,y) = X(x)Y(y) , \tag{2.11}$$

then $X(x)$ should satisfy:

$$X'' - \left(\frac{L\lambda}{\delta}\right)^2 X = 0 \qquad \text{in } 0 < x < 1 \text{ , with} \tag{2.12}$$

$$X' = 0 \qquad \text{at } x = 1 , \tag{2.13}$$

and $Y(y)$ satisfies

$$Y'' + \lambda^2 Y = 0 \qquad \text{in } 0 < y < 1 \text{ , with} \tag{2.14}$$

$$Y' + (h\delta/k_2)Y = 0 \qquad \text{at } y = 1 \text{ , and} \tag{2.15}$$

$$\frac{k_1 t}{L^2} X''Y + \frac{k_2}{\delta} XY' = 0 \qquad \text{at } y = 0 . \tag{2.16}$$

Together with Equation (2.12), the boundary condition of Equation (2.16) becomes

$$Y' + M\lambda^2 Y = 0 \qquad \text{at } y = 0 \text{ , with} \tag{2.17a}$$

$$M = \frac{k_1 t}{k_2 \delta} \tag{2.17b}$$

The second-order ordinary differential equations for $X(x)$ and $Y(y)$ are solved, and three of the four constants are determined using the boundary conditions of Equations (2.13), (2.15) and (2.17). The solution is

$$\theta(x,y) = \sum_{n=1}^{\infty} C_n Y(\lambda_n; y) \cosh\left(\frac{\lambda_n L}{\delta}(1-x)\right) , \tag{2.18}$$

where the eigenfunctions $Y(\lambda_n; y)$ are

$$Y(\lambda_n; y) = \cos(\lambda_n y) - M\lambda_n \sin(\lambda_n y) , \tag{2.19}$$

and the eigenvalues λ_n satisfy the following eigencondition:

$$\tan\left(\lambda_n\right)=\frac{k_1k_2t}{\delta\left(k_2^2+hk_1t\right)}\left[\left(\frac{h\delta^2}{k_1t}\right)\frac{1}{\lambda_n}-\lambda_n\right] \quad n=1,2,3,... \tag{2.20}$$

The last boundary condition of Equation (2.10e) gives

$$f(y)=\sum_{n=1}^{\infty}C_n\left[\cos\left(\lambda_n y\right)-M\lambda_n\sin\left(\lambda_n y\right)\right]\cosh\left(\frac{\lambda_n L}{\delta}\right) \ . \tag{2.21}$$

According to the sense of orthogonality derived in Appendix A,

$$C_m = \frac{\int_0^1 f\left(y'\right)Y\left(\lambda_m;y'\right)dy'+Mf\left(0\right)Y\left(\lambda_m;0\right)}{\cosh\left(\frac{\lambda_m L}{\delta}\right)\left\{\int_0^1\left[Y\left(\lambda_m;y'\right)\right]^2dy'+M\left[Y\left(\lambda_m;0\right)\right]^2\right\}} \ , \tag{2.22}$$

then as $\varepsilon\to 0$

$$C_m=\frac{\int_0^1 Y\left(\lambda_m;y'\right)dy'+MY\left(\lambda_m;0\right)}{\cosh\left(\frac{\lambda_m L}{\delta}\right)\left\{\int_0^1\left[Y\left(\lambda_m;y'\right)\right]^2dy'+M\left[Y\left(\lambda_m;0\right)\right]^2\right\}} \ ; \tag{2.23}$$

thus,

$$C_m=\frac{2\left(\frac{\sin\left(\lambda_m\right)/\lambda_m}{\cosh\left(\lambda_m L/\delta\right)}+M\frac{\cos\left(\lambda_m\right)}{\cosh\left(\lambda_m L/\delta\right)}\right)}{1+\frac{\sin\left(2\lambda_m\right)}{2\lambda_m}+M^2\lambda_m^2\left[1-\frac{\sin\left(2\lambda_m\right)}{2\lambda_m}\right]+M\left[1+\cos\left(2\lambda_m\right)\right]} \ . \tag{2.24}$$

Finally, the temperature distribution inside the two-dimensional slab—using dimensional variables—is

$$\frac{T_2(x,y)-T_e}{T_b-T_e}=\sum_{n=1}^{\infty}C_n\left[\cos\left(\frac{\lambda_n y}{\delta}\right)-M\lambda_n\sin\left(\frac{\lambda_n y}{\delta}\right)\right]\cosh\left(\frac{\lambda_n(L-x)}{\delta}\right) \ , \tag{2.25}$$

where λ_n and C_n are given by Equations (2.20) and (2.24), respectively. An expression for the temperature along the one-dimensional fin is obtained by evaluating Equation (2.25) at y=0

$$\frac{T_1(x)-T_e}{T_b-T_e}=\sum_{n=1}^{\infty}C_n\cosh\left(\frac{\lambda_n(L-x)}{\delta}\right) \ . \tag{2.26}$$

The fin heat transfer can be calculated by differentiating Equation (2.26) and using Fourier's law at x=0 to find the heat flowing from material 1; likewise, we differentiate Equation (2.25), apply Fourier's law at x=0, and integrate from y=0 to $y=\delta$ to find the heat flowing from material 2. Dividing the fin heat transfer by the convective

heat transfer that would occur if the frost surface temperature were equal to the base temperature gives the fin efficiency

$$\eta = \frac{1}{\delta h L}\sum_{n=1}^{\infty} C_n \lambda_n \sinh\left(\frac{\lambda_n L}{\delta}\right)\left\{k_1 t + \delta k_2\left(\frac{\sin(\lambda_n)}{\lambda_n} + M(\cos(\lambda_n)-1)\right)\right\} \quad . \tag{2.27}$$

The calculation of the temperature profile and fin efficiency using the above solutions is much easier than the solution for two-dimensional heat flow both for the fin and its coating material, especially when calculating the eigenvalues, λ_n . According to Barker (1958), the solution to that more complex case results in the following eigencondition

$$\frac{k_1}{k_2}\tan\left(\lambda_n^B\right) = \frac{1-\lambda_n^B \frac{k_2}{ht}\tan\left(\lambda_n^B\left(\frac{\delta}{t}-1\right)\right)}{\tan\left(\lambda_n^B\left(\frac{\delta}{t}-1\right)\right)+\lambda_n^B\frac{k_2}{ht}} \quad . \tag{2.28}$$

The behavior of Equation (2.28) is complex, depending on δ/t, and this complexity makes it difficult to develop an initial guess for the distribution of the roots of Equation (2.28); therefore, calculation of eigenvalues through a Newton-Raphson iteration—or by any other method—is difficult. In contrast, by designating the left-hand side of Equation (2.20) as $f_1(\lambda)$ and the right-hand side as $f_2(\lambda)$ the eigencondition for the simplified problem always behaves as shown in Figure 2.2. A clear expectation for the distribution of the roots is possible, and solution by Newton-Raphson is more likely to converge.

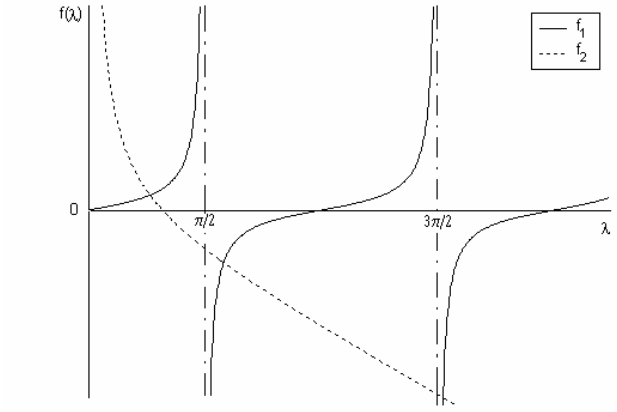

Figure 2.2 The roots of Equation (2.20) are shown as the intersection of the left-hand side (f_1) and the right-hand side (f_2) of the equation.

2.5 An Example Application to Frost on an Aluminum Fin

The temperature distribution along a fin is calculated for frost on a metallic fin using the realistic parameters given in Table 2.2. The conditions of Table 2.2 make $B_i = 0.18$, $R = 8.2(10^{-4})$, and $t \approx 0.1\delta \approx 0.01L$. According to Table 2.1, the temperature differences between y=0 and y=-t are less than 5% of T_e-T_b, and the fin can be assumed one-dimensional; thus, the analytical solution applies.

Table 2.2 Parameters of an example

T_e	°C	-2.8
T_b	°C	-5.0
L	mm	4.14
δ	mm	0.45
H	$Wm^{-2}K^{-1}$	70.4
k_1	$Wm^{-1}K^{-1}$	237
k_2	$Wm^{-1}K^{-1}$	0.175
T	mm	0.05

Temperature results for this practical case were also obtained using a numerical solution to the fully two-dimensional case and a comparison of the numerical and analytical results of Equations (2.20), and (2.24)-(2.26) is given in Figure 2.3. It is demonstrated that the full analytical solution matches the numerical solution very well. It is also evident that for y=0, a one-term approximation is valid, but for $y=\delta$ an additional term is required to predict the temperature along the frost-air interface.

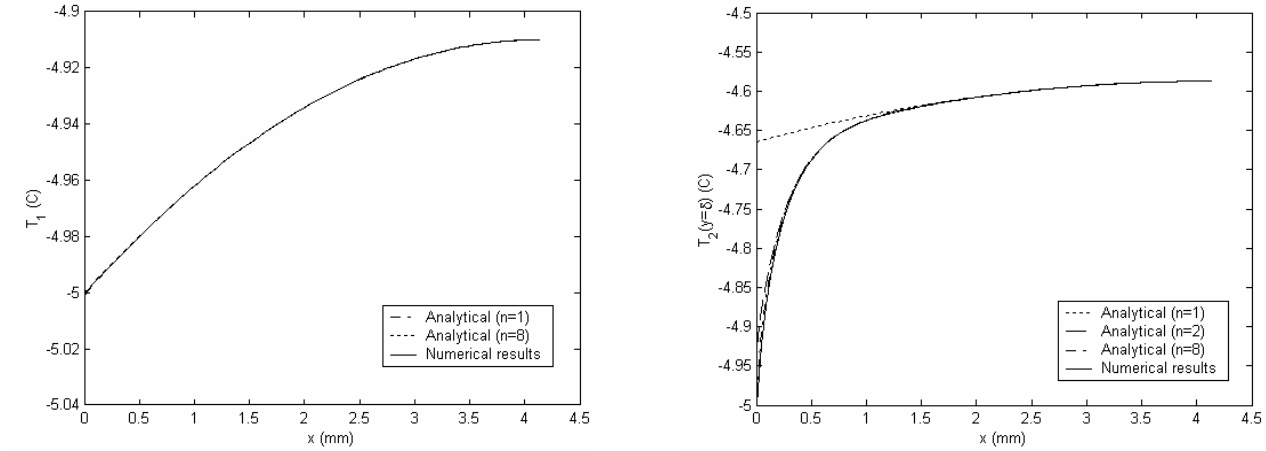

(a) (b)

Figure 2.3 A comparison of the numerical results to the analytical solution for the test conditions given in Table 2.2. Results are calculated using different numbers of terms in the series, for (a) $T_2(x,0)=T_1(x)$ and (b) $T_2(x,\delta)$.

The fin efficiency is shown in Figure 2.4, for two different values of the convection coefficient, h=50.4 $Wm^{-2}\,°C^{-1}$ and h=70.4 $Wm^{-2}\,°C^{-1}$, with a range of frost thicknesses, to expand the conditions of Table 2.2. These results were obtained with Equations (2.20), (2.24) and (2.27). The fin efficiency does not go to unity for a zero-thickness frost layer, because the metallic substrate is not a perfect conductor of heat. It should be noted that while the fin efficiency depends on t, δ, L, h, k_1 and k_2, it does not depend on the temperatures T_e and T_b.

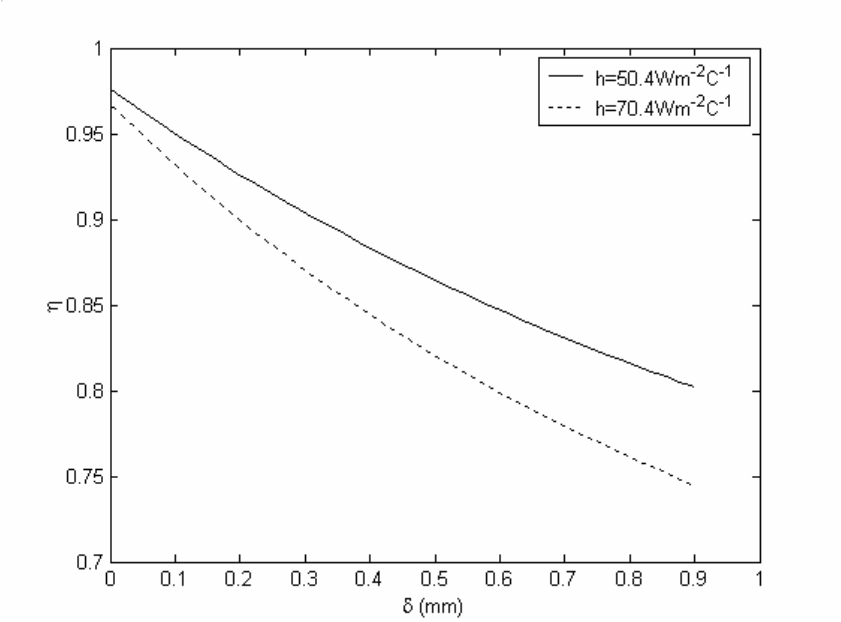

Figure 2.4 Using the conditions of Table 2.2, for a range of frost thicknesses and two values of convective heat transfer coefficient, example fin efficiency results are provided.

2.6 One-Term Approximation

It is possible to consider a special case for which a one-term approximation to the series solution is sufficient by exploiting the behavior of the eigencondition. The first eigenvalue is always less than the positive root of $f_2(\lambda)=0$. That is,

$$0 < \lambda_1 < \sqrt{\frac{h\delta^2}{k_1 t}} \quad . \tag{2.29}$$

When

$$\sqrt{\frac{h\delta^2}{k_1 t}} << 1 \ , \tag{2.30}$$

we have $\tan(\lambda_1) \approx \lambda_1$, and the first root of Equation (2.20) can be approximated by

$$\lambda_1 \approx \delta \sqrt{\frac{h}{k_1 t + \delta\left(k_1 h t / k_2 + k_2\right)}} \quad . \tag{2.31}$$

Furthermore, it can be shown from Equation (2.24) that when

$$\frac{k_1 k_2 t}{\delta\left(k_2{}^2 + h k_1 t\right)} >> 1, \tag{2.32}$$

we have

$$C_1 \approx \left[\cosh\left(\frac{\lambda_1 L}{\delta}\right)\right]^{-1}, \tag{2.33}$$

with $C_n \approx 0$ for n=2,3…

The one-term approximation to the series solution in material 2 is then

$$\frac{T_2(x,y)-T_e}{T_b-T_e} \approx \left[1-\frac{M\lambda_1^2 y}{\delta}\right]\frac{\cosh\left(\frac{\lambda_1(L-x)}{\delta}\right)}{\cosh\left(\frac{\lambda_1 L}{\delta}\right)} \quad , \tag{2.34a}$$

and in material 1

$$\frac{T_1(x)-T_e}{T_b-T_e} \approx \frac{\cosh\left(\frac{\lambda_1(L-x)}{\delta}\right)}{\cosh\left(\frac{\lambda_1 L}{\delta}\right)} \quad , \tag{2.34b}$$

where λ_1 is given by Equation (2.31). Under the one-term approximation, the fin efficiency is

$$\eta' = \frac{\lambda_1}{hL\delta}\frac{\sinh\left(\frac{\lambda_1 L}{\delta}\right)}{\cosh\left(\frac{\lambda_1 L}{\delta}\right)}\left(k_1 t + k_2\delta\right) \quad . \tag{2.35}$$

In Figure 2.5, the difference between η and η' is shown as a function of the frost thickness for the conditions of Table 2.2. The one-term approximation under-predicts the fin efficiency by up to a few percent at the lowest fin efficiency. For fin efficiency larger than 80%, the series solution and its one-term approximation, Equations (2.27) and (2.35) respectively, differ by less than 1%. It is noteworthy that if the heat conducted into the base through the frost is neglected, then the $\eta - \eta$' is as high as 20% for some conditions used in Figure 2.5. The error in neglecting conduction through the frost is pronounced for thick frost layers. Thus, Equation (2.35) which accounts for conduction through both the frost and the metallic fin is preferred to an expression neglecting such effects.

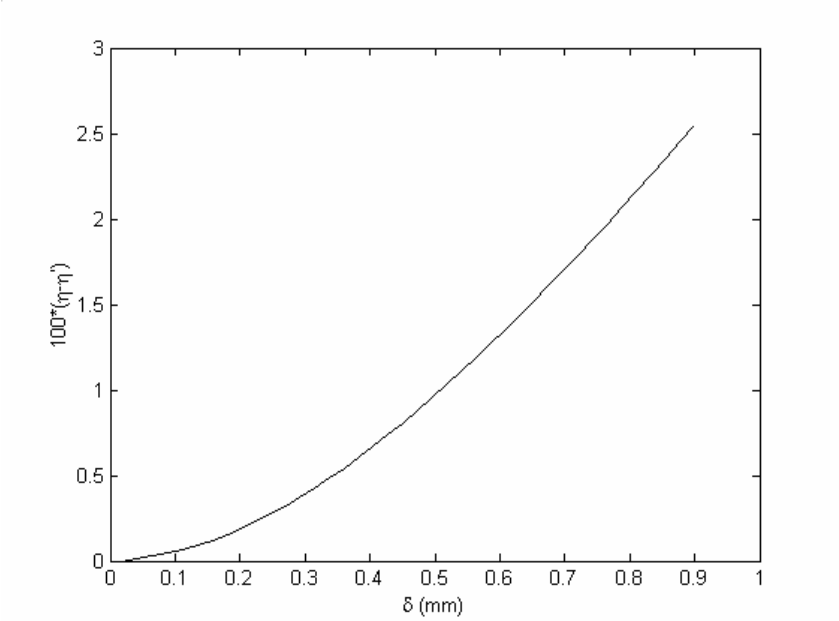

Figure 2.5 The difference between fin efficiency accounting for conduction in the frost layer and fin efficiency assuming negligible conduction from the frost to the tube is shown. The plot is constructed using the conditions of Table 2.2.

2.7 Conclusions

The temperature distribution within a two-dimensional composite fin is analyzed. A numerical parametric analysis shows that when $B_i > 0.05$ and $R < 0.1$, the problem can be approximated as a two-dimensional slab on a one-dimensional fin. Under this approximation, an exact solution is obtained by the separation of variables, exploiting orthogonality in the sense defined in Appendix A. In comparison to prior fully two-dimensional solutions, this new solution has the advantages of rapid convergence and relatively simple calculation. Moreover, conditions are developed under which a one-term approximation to the solution is sufficient, and it is found that frost on a metallic fin often falls into this range. The analytical solution presented in this chapter, and the one-term approximation, have broad applicability in addition to their use for calculating fin efficiency for frost-coated fins.

Chapter 3. Air-Side Data Interpretation and Performance Analysis for Heat Exchangers with Simultaneous Heat and Mass Transfer: Wet and Frosted Surfaces

Nomenclature

A	area (m^2)
c_p	specific heat (J kg^{-1} $°C^{-1}$)
g_m	mass transfer conductance (kg m^{-2} s^{-1})
h	convective heat transfer coefficient (W m^{-2} $°C^{-1}$)
h_{sg}	latent heat of ablimation (for water) (J kg^{-1})
H_f	fin height (m)
i	enthalpy (J kg^{-1})
Δi_{lm}	logarithmic-mean enthalpy difference (J kg^{-1})
k	thermal conductivity (Wm^{-1} $°C^{-1}$)
L_f	fin width (m)
$\dot{m}$	mass flow rate (kg s^{-1})
q	heat transfer rate (W)
R	heat transfer resistance (°C W^{-1}), or energy transfer resistance (s kg^{-1})
t	half fin thickness , see Figure 2.1 (m)
T	temperature (°C)
T_{dew}	dewpoint temperature (°C)
ΔT_{lm}	logarithmic-mean temperature difference (°C)

Greek Symbols

δ	frost thickness (m)
η	fin efficiency
ω	humidity ratio

Subscripts and Superscripts

1d	one-dimensional conduction effects in frost layer
a	moist air (i.e., dry air plus water vapor)
b	base
c	cold-fluid side
cond	conduction
conv	convection
f	frost
f-f	frosted-fin
fi	fin
fs	frost surface (fin surface in case of wet-surface condition)
h	hot-fluid side
i	inside/inlet
l	latent heat
o	outside/overall
r	refrigerant or coolant-side
s	sensible heat
sat	saturated
unf	unfinned
vs	accounting for variable sensible heat effects
w	tube wall

3.1 Introduction

When designing or predicting the performance of a heat exchanger, it is essential to relate the total heat transfer rate to the overall heat conductance and driving potential. In many air-cooling applications, condensation or frost forms on the air-side surface of a heat exchanger. For operating conditions with simultaneous sensible and latent heat transfer, two analysis methods are commonly adopted: one uses an overall heat conductance UA based on the logarithmic-mean temperature difference (LMTD), the other uses the so-called overall energy conductance HA based on the logarithmic-mean enthalpy difference (LMED). There are significant differences in these approaches and their variations reported in the literature, and these differences can lead to large differences in the heat transfer coefficient inferred from heat exchanger data, or to large departures from performance predictions. In this chapter we consider data reduction and interpretation methods for heat exchangers under conditions of simultaneous heat and mass transfer. The focus is on heat exchangers used in air-conditioning, heat pumping, and refrigeration systems.

Data reduction methods based on enthalpy potential have been widely used for condensing conditions, and several investigators have derived and used these methods for heat exchangers operating under frosting conditions. Sander (1974) presented a convincing derivation of the overall energy conductance based on an enthalpy potential.

However, his expression for calculating fin efficiency unnecessarily neglects heat transfer in the frost layer parallel to the length of the fin[1]. Kondepudi and O'Nea (1989) derived an energy transfer coefficient in terms of the logarithmic-mean enthalpy difference, but they did not attempt to obtain the air-side convective heat transfer coefficient using the enthalpy difference. Ogawa *et al.* (1993) used a logarithmic enthalpy difference to calculate the air-side heat transfer coefficient, but they did not separate the fin- and frost-conduction effects from the convective heat transfer coefficient. Mago and Sherif (2002) calculated the overall heat transfer coefficient based on an enthalpy potential, but their method for computing the fin efficiency also neglected heat transfer in the frost layer parallel to the length of the fin.

Data interpretation using the LMED is based on several tacit assumptions, as discussed in detail later. However, the usually small error introduced by these assumptions has not been carefully quantified in earlier work. Moreover, there is a major limitation to the LMED method: it fails when the heat exchanger surface is partially wet or partially frosted. This failure occurs because mass transfer does not take place when the saturated humidity ratio corresponding to the surface temperature is higher than the humidity ratio of the moist air. The problem can be surmounted if the heat exchanger area is partitioned into wet or frosted and dry areas, but such area partitioning can be problematic.

The overall energy conductance *HA* is commonly used to interpret heat exchanger performance for simultaneous heat and mass transfer; however, the overall heat conductance *UA* has been more widely adopted and often misapplied. Under frosting conditions, for example, Stoecker (1960), Barrow (1985), Huffman and Sepsy (1967), and Niederer (1976) all adopted a *UA*-based approach, but their use of *UA* follows that for dry-surface conditions (as do others). As shown later, this approach is invalid and can lead to large errors when latent heat effects are important.

In addition to difficulties in interpreting *UA* or *HA* from an LMTD or LMED analysis, respectively, the issue of wet- or frosted-fin efficiency is also not clearly resolved in the literature. Assuming a linear relation between the saturated humidity ratio and the dry-bulb temperature over the temperature range from fin tip to base, Wu and Bong (1994) provided analytical solutions for fin efficiency of a straight fin operating under fully wet and partially wet conditions. For frosting conditions, some researchers, such as Stoecker (1960) and Huffman and Sepsy (1967), simply add another series resistance to account for the conductive resistance of the frost. However, such a model neglects temperature variations along the frost surface, and the effects of such a simplification can be profound (see Xia and Jacobi, 2004). Similar to the work of Sander (1974), Kondepudi and O'Neal (1993) assumed no heat transfer in the frost layer along the fin length, and they developed an expression for fin efficiency for pin-fin heat exchangers under frosting conditions. They used an effective heat transfer coefficient, including latent and sensible heat transfer in the air-side convection coefficient.

The technical literature is replete with methods for reducing heat exchanger data under conditions of simultaneous heat and mass transfer. While the conventional approaches of *UA*-LMTD and *HA*-LMED and simple adaptations to dry-fin efficiency calculations are appropriate under some conditions, they can introduce large errors

[1] As shown in Chapter 2, this assumption can cause errors in calculating fin efficiency; moreover, it will be demonstrated in this chapter that there is an error in the fin efficiency expression developed by Sander (1974).

under other conditions. In this chapter, valid LMTD and LMED approaches for wet- and frosted-surface heat transfer will be clearly formulated—with attention to errors in conventional application of the methods—and expressions for fin efficiency that account for latent heat effects will be provided for both methods. With improved formulations for data interpretation in place, the two methods will be compared and evaluated using a numerical simulation of a simplified heat exchanger. A rational and consistent approach to reducing heat exchanger data might resolve (and avoid) disagreement over the behavior of the heat transfer coefficient under wet- and frosted-surface conditions.

3.2 Problem Description

The purpose is to formulate rational, general, and convincing methods for data reduction and interpretation applicable for wet- or frosted-surface heat exchangers. The development will focus on constant-area (straight) fins; however, an extension to other fins is obvious. The purpose of the data reduction is to obtain the air-side convective heat transfer coefficient from measurements of air inlet and outlet dry- and wet-bulb temperatures, coolant inlet and outlet temperatures, and air and coolant mass flow rates. The tube-wall conduction resistance is neglected, because it is almost always negligible, and the focus is now on the air-side resistance. The formulation of both the *UA*-LMTD and *HA*-LMED methods is presented in the sections that follow.

3.3 Logarithmic-Mean Enthalpy Difference Method

The energy transfer network for a heat exchanger working under wet or frosting conditions is shown in Figure 3.1(a). The form of this network, and part of the appeal of this formulation, is that it is directly analogous to the dry-surface network, with a series of resistors between two enthalpies, analogous to a series of resistors between two temperatures.

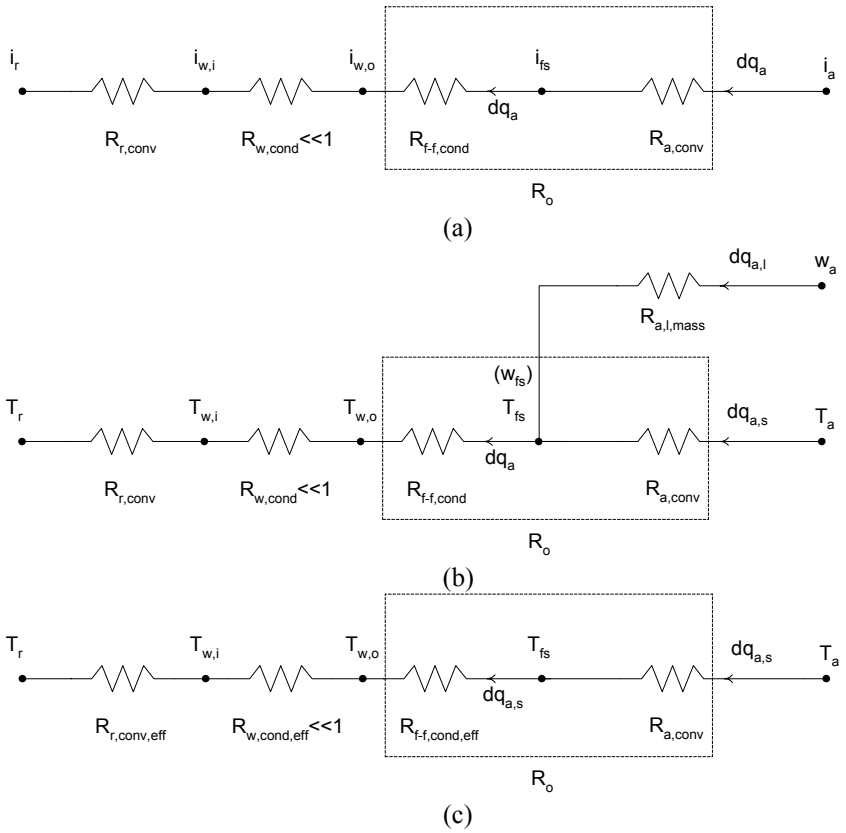

Figure 3.1 The energy transfer network (a), heat and mass transfer network (b), and analogous heat transfer network (c) with respect to an infinitesimal heat transfer area dA_h (or corresponding dA_c) for a heat exchanger operating under wet or frosting conditions.

In this network, the widely accepted concept of enthalpy potential is used, as described in Stoecker and Jones (1982). The heat transfer from the free-stream air to the wet surface is expressed in the form of enthalpy potential, i.e.

$$dq_a = dA\frac{h}{c_{p_a}}\left(i_a - i_{fs}\right). \tag{3.1}$$

In developing Equation (3.1), the analogy between heat and mass transfer is used with $Le^n \approx 1$, and with $i_f(\omega_{fs}-\omega_a)$ neglected, where Le is Lewis number (Pr/Sc) and i_f is the enthalpy of saturated liquid water (see Stoecker and Jones, 1982). By assuming $Le^n \approx 1$, an error in dq_a of about 8% can be introduced at a latent heat ratio of 50% (with $Le \approx 1.25$); this approximation is the major source of error in the LMED method.

In Equation (3.1), the enthalpy at the wet surface, i_{fs}, is taken as that of saturated moist air at the surface temperature. Also, in Figure 3.1(a), all the enthalpies except the enthalpy of the free-stream air, i_a, are evaluated as the enthalpy of saturated air at each corresponding temperature. In order to derive an expression for fin efficiency and the convective resistance of the coolant flow, $R_{r,conv}$, a linearization between the saturation enthalpy and the temperature of moist air is utilized, following Sander (1974):

$$i = a + bT\ , \tag{3.2}$$

where *a* and *b* are the coefficients for the linearization. This linearization, within the range of the operating temperatures, approximates the value of saturation enthalpy, and introduces another source of error. Based on the above assumptions, an overall energy conductance *HA* can be derived, as shown by Kondepudi and O'Neal (1989):

$$HA = \frac{q_a}{\Delta i_{lm}}, \tag{3.3}$$

where Δi_{lm} is the logarithmic-mean enthalpy difference. Δi_{lm} takes different forms for different heat exchanger flow arrangements (e.g., parallel flow and counter flow). Neglecting the conduction resistance of the tube wall, we have

$$\frac{1}{HA} = R_{r,conv} + R_o = \frac{1}{A_c h_c / b} + \frac{1}{\eta_h A_h h_h / c_{p_a}}. \tag{3.4}$$

Equations (3.3) and (3.4) constitute *HA*-LMED method. It should be noted that if the humidity ratio corresponding to the surface temperature is higher than that of the air, no mass transfer occurs, because there is no condensate or frost on the surface. Thus, Equation (3.1) is restricted to having mass transfer to occur only *from* the moist air stream *to* the surface. Neglecting this restriction causes the heat transfer calculated from Equation (3.1) to erroneously include latent heat associated with impossible mass transfer from the (dry) surface to the air; as shown later, this error can result in unrealistically high values of the heat transfer coefficient to be inferred from heat exchanger performance data. The *HA*-LMED method is applicable only when the surface is fully wet or frosted, and application to a partially wet or frosted surface requires area partitioning and a *UA*-LMTD analysis of the dry portion.

Next, expressions for fin efficiency and overall surface efficiency will be developed. The overall surface efficiency and fin efficiency, respectively, are

$$\eta_h = \frac{q_a}{A_h \left(h_h / c_{p_a}\right)\left(i_a - i_{w,o}\right)}, \text{ and} \tag{3.5}$$

$$\eta = \frac{q_{fi,b}}{A_{fi} \left(h_h / c_{p_a}\right)\left(i_a - i_{w,o}\right)}, \tag{3.6}$$

where $q_{fi,b}$ is the total heat (sensible and latent heat) flowing through the base of the fin, or the composite fin (fin plus frost) for the cases of frosting conditions. The derivations of η and η_h for frosting conditions are provided in Appendix B. The final expression for fin efficiency under frosting conditions is

$$\eta = \frac{2}{h_h \left(b / c_{pa}\right) H_f \delta_f} \sum_{n=1}^{\infty} C_n \lambda_n \sinh\left(\frac{\lambda_n H_f}{2\delta_f}\right)\left\{k_{fi} t + k_f \delta_f \left[\frac{\sin\left(\lambda_n\right)}{\lambda_n} + \frac{k_{fi} t}{k_f \delta_f}\left(\cos\left(\lambda_n\right) - 1\right)\right]\right\} \tag{3.7a}$$

with

$$C_n = \frac{2\left(\dfrac{\sin\left(\lambda_n\right)/\lambda_n}{\cosh\left(\lambda_n H_f / 2\delta_f\right)} + \dfrac{k_{fi} t}{k_f \delta_f}\dfrac{\cos\left(\lambda_n\right)}{\cosh\left(\lambda_n H_f / 2\delta_f\right)}\right)}{1 + \dfrac{\sin\left(2\lambda_n\right)}{2\lambda_n} + \left(\dfrac{k_{fi} t}{k_f \delta_f}\right)^2 \lambda_n^2 \left[1 - \dfrac{\sin\left(2\lambda_n\right)}{2\lambda_n}\right] + \dfrac{k_{fi} t}{k_f \delta_f}\left[1 + \cos\left(2\lambda_n\right)\right]}, \tag{3.7b}$$

and λ_n is the root of

$$\tan\left(\lambda_n\right)=\frac{k_{fi}k_f t}{\delta_f\left(k_f^2+\left(h_h b/c_{p_a}\right)k_{fi}t\right)}\left[\left(\frac{\left(h_h b/c_{p_a}\right)\delta_f^2}{k_{fi}t}\right)\frac{1}{\lambda_n}-\lambda_n\right]. \tag{3.7c}$$

A one-term approximation to the fin efficiency is (see Xia and Jacobi, 2004)

$$\eta=\frac{2\lambda}{h_h\left(b/c_{pa}\right)H_f\delta_f}\tanh\left(\frac{\lambda H_f}{2\delta_f}\right)\left(k_{fi}t+k_f\delta_f\right),\ \text{with} \tag{3.8a}$$

$$\lambda=\delta_f\sqrt{\frac{h_h\left(b/c_{p_a}\right)}{k_{fi}t+\delta_f\left[k_{fi}h_h\left(b/c_{p_a}\right)t/k_f+k_f\right]}}\ ; \tag{3.8b}$$

Alternately, if conduction heat transfer in the frost layer parallel to the length of the fin is neglected, the expressions of η and λ can be shown to reduce to

$$\eta_{1d}=\frac{2\lambda_{1d}}{h_h\left(b/c_{pa}\right)H_f\delta_f}\tanh\left(\frac{\lambda_{1d}H_f}{2\delta_f}\right)\left(k_{fi}t\right),\ \text{with} \tag{3.9a}$$

$$\lambda_{1d}=\delta_f\sqrt{\frac{h_h\left(b/c_{p_a}\right)}{k_{fi}t+\delta_f\left[k_{fi}h_h\left(b/c_{p_a}\right)t/k_f\right]}}\ . \tag{3.9b}$$

Finally, the surface efficiency is

$$\eta_h=\eta\frac{A_{fi}}{A_h}+\left(\frac{k_f/\delta_f}{h_h\left(b/c_{p_a}\right)+k_f/\delta_f}\right)\frac{A_h-A_{fi}}{A_h}. \tag{3.10}$$

Comparing Equation (3.9) to the expression of Sander (1974) as presented by Kondepudi and O'Neal (1987), it can be seen that the fin efficiency as developed by Sander is incorrect; the error leads to the misleading conclusion that fin efficiency increases with increasing frost thickness. In Figure 3.2, η and η_{1d} are compared using the parameteric values of Table 3.1 and (b/cp_a)=1.3, representing moist air at -20 < T < 0ºC and 0 < RH < 80%. The values obtained by numerically solving the governing equations given in Appendix B (Equations B.5 and B.6), are also shown in Figure 3.2, providing the 'true' fin efficiency.

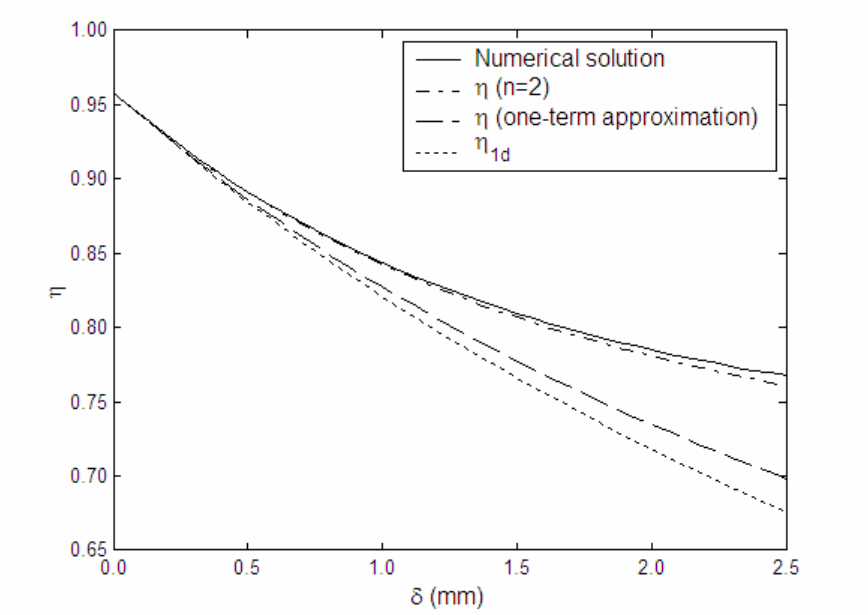

Figure 3.2 A comparison of frosted fin efficiency, η, as calculated by a finite-difference numerical solution (see Xia and Jacobi, 2004), the analytical solution given by Equation (3.7) with n=2, the one-term approximation to the analytical solution given by Eq (3.8), and the one-dimensional approximation given by Equation (3.9) for η_{1d}.

Table 3.1 Parameters used in Figures 3.2 and 3.3

H_f	mm	8.28
h_h	$Wm^{-2}K^{-1}$	70.4
k_{fi}	$Wm^{-1}K^{-1}$	237
k_f	$Wm^{-1}K^{-1}$	0.525
t	mm	0.05

Figure 3.2 demonstrates that as frost grows, the frosted-fin efficiency decreases, and the error in η_{1d} (Equation 3.9) becomes larger, because of neglected heat conduction in the frost layer parallel to the fin length. The error exceeds 2% for frost thicker than δ=1 mm. For frost layers with δ<1 mm, the one-term approximation (Equation 3.8) may be used, but for δ>1 mm at least two terms in Equation (3.7) are required to keep errors in η below 2%.

A derivation similar to that outlined in Appendix B results in expressions for condensing conditions that can be obtained by replacing h with hb/c_{pa} in the expressions for dry-fin efficiency; thus for condensing conditions

$$\eta = \frac{\tanh\left(\lambda H_f / 2\right)}{\lambda H_f / 2}, \text{ with (see Sanders, 1974)} \tag{3.11}$$

$$\lambda = \sqrt{\frac{h_h\left(b / c_{p_a}\right)}{k_{fi} t}}, \text{ and} \tag{3.12}$$

$$\eta_h = 1 - \frac{A_{fi}}{A_h}\left(1-\eta\right). \tag{3.13}$$

3.4 Logarithmic-Mean Temperature Difference Method

A valid heat and mass transfer network for a heat exchanger operating under wet- or frosted-surface conditions is shown in Figure 3.1(b). We can cast the network of Figure 3.1(b) into a form analogous to that of Figure 3.1(a) if we define an *effective* heat transfer resistance to be the temperature difference over sensible heat transfer. The resulting network is then reduced to the one shown in Figure 3.1(c); this form of resistor network is convenient and appealing because of its similarity to the dry-surface and LMED networks. As an example of an effective resistance, consider the effective convective heat transfer resistance on the coolant side, $R_{r,conv,eff}$:

$$R_{r,conv,eff} = \frac{T_{w,i} - T_r}{q_{a,s}}. \tag{3.14}$$

Then, following the approach used in dry-surface heat exchanger analysis, an overall heat transfer coefficient is defined as

$$U = \frac{dq_{a,s}}{dA_h \Delta T} = \frac{dq_{a,s}}{dA_h\left(T_a - T_r\right)}. \tag{3.15}$$

Based on Figure 3.1(c), the resistance components in the network are

$$\frac{1}{UdA_h} = R_{r,conv,eff} + R_o = \frac{1}{dA_c h_c\left(dq_{a,s}/dq_a\right)} + \frac{1}{\eta_h dA_h h_h}. \tag{3.16}$$

The appropriate *UA*-LMTD method is derived by relating the heat transfer rates to the temperature changes on the air and the refrigerant side,

$$dq_a = \dot{m}_r c_{p_r} dT_r, \text{ and} \tag{3.17}$$

$$dq_{a,s} = -\dot{m}_a c_{p_a} dT_a. \tag{3.18}$$

Noting $\Delta T = T_a - T_r$, we have

$$d\left(\Delta T\right) = dT_a - dT_r. \tag{3.19}$$

Substituting from Equations (3.17) and (3.18) into Equation (3.19):

$$d\left(\Delta T\right) = -dq_{a,s}\left[\frac{1}{\dot{m}_a c_{p_a}} + \frac{1}{\dot{m}_r c_{p_r}\left(dq_{a,s}/dq_a\right)}\right]. \tag{3.20}$$

From the definition of U, recognizing we will base the overall conductance on the air-side area (i.e., UA_h), we have

$$dq_{a,s} = UdA_h\Delta T. \tag{3.21}$$

Substituting into Equation (3.20), rearranging, and noting that $d(\Delta T)/\Delta T = d(\ln \Delta T)$,

$$d\left(\ln \Delta T\right) = -U dA_h \left[\frac{1}{\dot{m}_a c_{p_a}} + \frac{1}{\dot{m}_r c_{p_r} \left(dq_{a,s} / dq_a \right)} \right]. \tag{3.22}$$

In general, the local sensible heat ratio $dq_{a,s}/dq_a$ can be expected to vary over the surface area, and expressing it analytically to pursue a closed-form integration of Equation (3.22) requires assumptions that vitiate the generality of the resulting solution. However, when the variation in $dq_{a,s}/dq_a$ is negligible the local sensible heat ratio is equal to $q_{a,s}/q_a$, and Equations (3.20) and (3.22) can be easily integrated, and combining by eliminating the term in the square bracket gives

$$UA = \int U dA_h = \frac{q_{a,s}}{\Delta T_{lm}} \ , \tag{3.23}$$

where ΔT_{lm} is the logarithmic-mean temperature difference. ΔT_{lm} takes a form dependent on flow arrangement of the heat exchanger. Because this convenient form results, we will adopt the assumption that $dq_{a,s}/dq_a = q_{a,s}/q_a$ (equivalent to assuming variations in $dq_{a,s}/dq_a$ negligible); in evaluating the method later in the chapter, we will explore the impact of deviations from that assumption on the inferred heat transfer coefficient. Under this assumption, Equation (3.16) yields

$$\frac{1}{UA} = \frac{1}{A_c h_c \left(q_{a,s} / q_a \right)} + \frac{1}{\eta_h A_h h_h} . \tag{3.24}$$

Equations (3.23) and (3.24) constitute the method of *UA*-LMTD. The method also applies to dry-surface conditions, where $dq_{a,s}/dq_a = q_{a,s}/q_a = 1$ and Equations (3.23) and (3.24) reduce to those of dry test conditions. The particularly interesting cases of partially wet- or frosted-surface conditions will also be assessed in the next section—those cases represent extreme departures from the $dq_{a,s}/dq_a = q_{a,s}/q_a$.

The remaining task is to develop expressions for fin efficiency and overall surface efficiency. The overall surface efficiency is defined as

$$\eta_h = \frac{q_a}{A_h h_h \left(q_a / q_{a,s} \right) \left(T_a - T_{w,o} \right)} . \tag{3.25}$$

For frosting conditions, the fin efficiency is defined as the ratio of the total heat flowing through the base of the composite fin (fin plus frost), to the maximum possible total heat that can be exchanged were the surface temperature of the composite fin at the fin base temperature. Invoking the assumption of constant sensible heat ratio again, the definition of this frosted-fin efficiency can be reduced to

$$\eta = \frac{q_{fi,b}}{A_{fi} h_h \left(q_a / q_{a,s} \right) \left(T_a - T_{w,o} \right)} . \tag{3.26}$$

The derivation of η and η_h are provided in Appendix B. The final expressions for frosting conditions are:

$$\eta = \frac{2}{h_h\left(q_a / q_{a,s}\right) H_f \delta_f} \sum_{n=1}^{\infty} C_n \lambda_n \sinh\left(\frac{\lambda_n H_f}{2\delta_f}\right)\left\{k_{fi} t + k_f \delta_f \left[\frac{\sin\left(\lambda_n\right)}{\lambda_n} + \frac{k_{fi} t}{k_f \delta_f}\left(\cos\left(\lambda_n\right) - 1\right)\right]\right\}, \tag{3.27a}$$

with C_n calculated using Equation (3.7b), and λ_n being the root of

$$\tan\left(\lambda_n\right) = \frac{k_{fi} k_f t}{\delta_f\left(k_f^2 + \left(h_h q_a / q_{a,s}\right) k_{fi} t\right)}\left[\left(\frac{\left(h_h q_a / q_{a,s}\right)\delta_f^2}{k_{fi} t}\right)\frac{1}{\lambda_n} - \lambda_n\right]. \tag{3.27b}$$

A one-term approximation to the fin efficiency is (see Xia and Jacobi, 2004)

$$\eta = \frac{2\lambda}{h_h\left(q_a / q_{a,s}\right) H_f \delta_f} \tanh\left(\frac{\lambda H_f}{2\delta_f}\right)\left(k_{fi} t + k_f \delta_f\right), \text{ where} \tag{3.28a}$$

$$\lambda = \delta_f \sqrt{\frac{h_h\left(q_a / q_{a,s}\right)}{k_{fi} t + \delta_f\left[k_{fi} h_h\left(q_a / q_{a,s}\right) t / k_f + k_f\right]}}. \tag{3.28b}$$

Finally, the surface efficiency is

$$\eta_h = \eta \frac{A_{fi}}{A_h} + \left(\frac{k_f / \delta_f}{h_h\left(q_a / q_{a,s}\right) + k_f / \delta_f}\right)\frac{A_h - A_{fi}}{A_h}. \tag{3.29}$$

Similarly, the expressions of η and η_h for condensing conditions are:

$$\eta = \frac{\tanh\left(\lambda H_f / 2\right)}{\lambda H_f / 2}, \text{ where} \tag{3.30}$$

$$\lambda = \sqrt{\frac{h_h\left(q_a / q_{a,s}\right)}{k_{fi} t}}, \text{ and} \tag{3.31}$$

$$\eta_h = 1 - \frac{A_{fi}}{A_h}\left(1 - \eta\right). \tag{3.32}$$

In the above expressions for fin efficiency, the mass transfer effects are absorbed into the air-side heat transfer coefficient by assuming a constant sensible heat ratio. More accurate expressions can be developed if the mass transfer effects are isolated by assuming a linear relation between the saturated humidity ratio ω_{sat} and moist-air temperature T over the temperature range from fin tip to fin base, i.e.

$$\omega_{sat} = c + eT. \tag{3.33}$$

where c and e are constants for the linearization. Invoking this assumption is equivalent to assuming a linear relationship between the sensible heat and the total heat over the fin surface. Wu and Bong (1994) used this assumption to develop fin efficiency expressions for condensing conditions. Our new derivation for frosting conditions is given in Appendix B; the resulting expressions for fin efficiency are

$$\eta_{vs} = \frac{2}{h_h^{'} H_f \delta_f} \sum_{n=1}^{\infty} C_{n,vs} \lambda_{n,vs} \sinh\left(\frac{\lambda_{n,vs} H_f}{2\delta_f}\right)\left\{k_{fi} t + k_f \delta_f \left[\frac{\sin\left(\lambda_{n,vs}\right)}{\lambda_{n,vs}} + \frac{k_{fi} t}{k_f \delta_f}\left(\cos\left(\lambda_{n,vs}\right) - 1\right)\right]\right\}, \tag{3.34a}$$

with $C_{n,vs}$ calculated using Equation (3.7b) and $\lambda_{n,vs}$, and $\lambda_{n,vs}$ is the root of

$$\tan\left(\lambda_{n,vs}\right) = \frac{k_{fi}k_f t}{\delta_f\left(k_f^2 + h_h^{'}k_{fi}t\right)}\left[\left(\frac{h_h^{'}\delta_f^2}{k_{fi}t}\right)\frac{1}{\lambda_{n,vs}} - \lambda_{n,vs}\right], \text{ and} \tag{3.34b}$$

$$h_h^{'} = h_h\left(1 + \frac{h_{sg}g_m e}{h_h}\right). \tag{3.35}$$

A one-term approximation is (see Xia and Jacobi, 2004)

$$\eta_{vs} = \frac{2\lambda_{vs}}{h_h^{'}H_f\delta_f}\tanh\left(\frac{\lambda_{vs}H_f}{2\delta_f}\right)\left(k_{fi}t + k_f\delta_f\right), \text{ with} \tag{3.36a}$$

$$\lambda_{vs} = \delta_f\sqrt{\frac{h_h^{'}}{k_{fi}t + \delta_f\left[k_{fi}h_h^{'}t/k_f + k_f\right]}}. \tag{3.36b}$$

In Figure 3.3, the values of η and η_{vs} are compared for the parametric values given in Table 3.1, with a frost thickness of 1 mm for various values of relative humidity. The values of mass transfer conductance, g_m, are related to the convective heat transfer coefficients, h_h, through the Lewis analogy. The values obtained by numerically solving the governing equations for the temperature distribution in the frosted fin, as given in Appendix B (Equations B.1, B.2, and B.3 as appropriate), which closely represents the true fin efficiency, are also shown in Figure 3.3. In Figure 3.3(a), results from using Equations (3.27) and (3.34) with n=2 are shown, and the one-term approximations given by Equations (3.28) and (3.36) are shown in Figure 3.3(b). Clearly, the use of η_{vs} is superior to that of η: it predicts fin-efficiency and trends better, because it accounts for the variation of saturation state on the fin. The relative-humidity conditions for which no mass transfer occurs, and for which the fin is partially frosted are also shown. In application, if a fin is partially frosted, a portion of the fin area is frost-coated, and the coverage would change in time. If it is desired to reduce heat exchanger data with insensitivity to partially frosted or partially wet conditions, and with fin efficiency errors of less than 1%, then the Equation (3.34) should be adopted. It should be noted, however, that the errors associated with the much simpler Equations (3.28) or (3.36) are less than about 2%, and not much accuracy is sacrificed by their use.

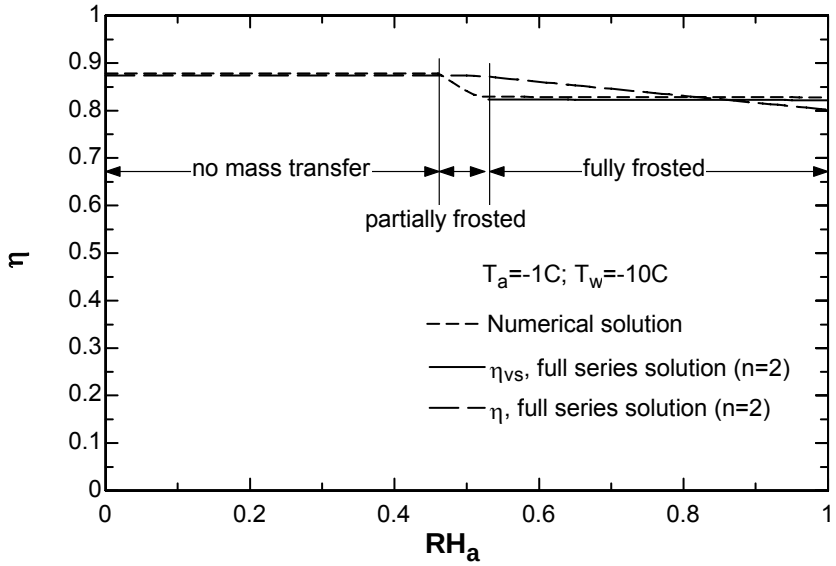

(a)

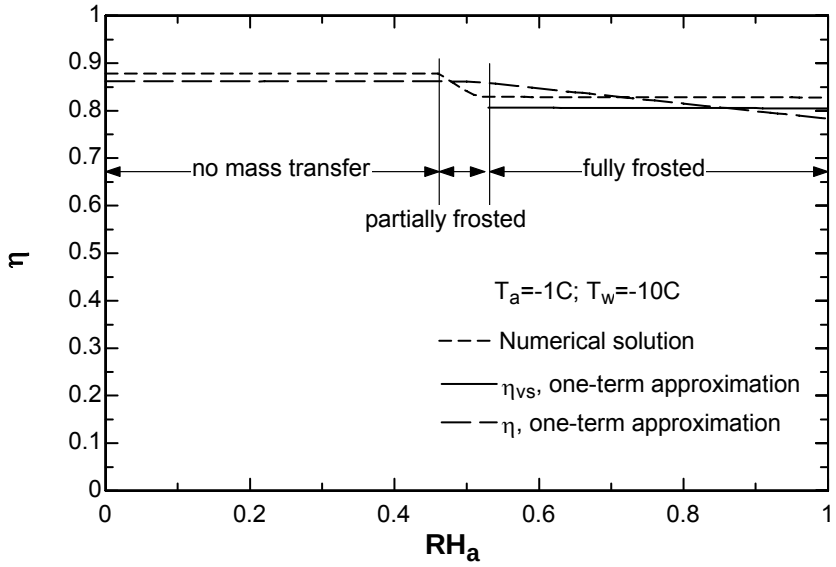

(b)

Figure 3.3 A comparison between η, η_{vs} and the numerical solution of fin efficiency: (a) using the series solutions with n=2, and (b) using a one-term approximation.

3.5 An Evaluation of the Two Methods

An evaluation of the two methods, *HA*-LMED and *UA*-LMTD, will be conducted using a numerical model of a parallel-plate heat exchanger operating in a parallel-flow configuration. This approach is adopted because the fin-efficiency models have been validated, and the focus is now on assessing the impact of the fundamental assumptions of the two methods. For simplicity, the simulation of frosting conditions is conducted at the quasi-steady-state condition corresponding to the start of frosting; i.e., there is not a resistance due to frost in the numerical model. In addition to the conservation of energy, as expressed by Equations (3.17) and (3.18), the rate equations for simultaneous heat and mass transfer are needed. They are

$$dq_{a,s} = dA_h h_h \left(T_a - T_w\right) , \tag{3.37}$$

$$dq_{a,l} = \begin{cases} dA_h h_{sg} g_m \left(\varpi_a - \varpi_w\right), & \varpi_a > \varpi_w \\ 0, & \varpi_a \le \varpi_w \end{cases} , \tag{3.38}$$

$$dq_a = dA_c h_c \left(T_w - T_r\right) , \tag{3.39}$$

$$dq_a = dq_{a,s} + dq_{a,l} \text{ , and} \tag{3.40}$$

$$dq_{a,l} = -\dot{m}_a h_{sg} d\varpi_a . \tag{3.41}$$

Equations (3.17), (3.18), and (3.37)-(3.41) are the governing equations, and a real-mixture psychrometric relationship gives the saturated humidity ratio as a function of the local plate temperature, $\omega_w(T_w)$, at one atmosphere. Noting dA_c=dA_h, the inlet air and coolant temperatures and the inlet humidity, along with air- and coolant-side convection coefficients and flow rates are prescribed. The governing equations are solved numerically to find the outlet temperatures, humidity, sensible, latent, and total heat transfer. The numerical solution was based on a central-difference approximation to the derivatives, with a varying discretization of the heat transfer area.[2]

With the inlet and outlet temperatures and humidity taken as known, along with the flow rates and the coolant-side convection coefficient, the air-side heat transfer coefficient is calculated using the *HA*-LMED and *UA*-LMTD methods developed in the prior sections. The results are in turn compared to the value prescribed in the numerical model (taken as the 'true' value). These tests were conducted over a range of temperatures, relative humidities, and coolant-side convection coefficients. The parameters taken as fixed in all the simulations are provided in Table 3.2. The coolant properties were taken as those of ethyl alcohol. The conditions for these numerical tests were adopted to mimic application; restrictions notwithstanding, the results are general as a basis for understanding and evaluating the *HA*-LMED and *UA*-LMTD methods.

Table 3.2 Parameters used in the numerical simulation

h_h	$Wm^{-2}K^{-1}$	50
$\dot{m}_a$	kg/s	0.15
$\dot{m}_r$	kg/s	0.105
A_h	m^2	3
A_c	m^2	3

The calculated air-side heat transfer coefficient for varying inlet humidity is shown in Figure 3.4 for two different h_c/h_h ratios under air-conditioning conditions; the corresponding variations in local sensible heat ratio are shown in Figure 3.5. The air-side convective heat transfer coefficient calculated using the method of *UA*-LMTD for dry-surface conditions, i.e., with Equation (3.24) replaced by

$$\frac{1}{UA} = \frac{1}{A_c h_c} + \frac{1}{\eta_h A_h h_h} , \tag{3.42}$$

[2] In Figures 3.4-3.6, six area elements were used (to allow easy interpretation of the local sensible heat ratio). In Table 3.3, fifty area elements were used. The numerical uncertainty is less than ±0.3 $Wm^{-2}K^{-1}$ for the six-element case and less than $\pm 10^{-5}$ $Wm^{-2}K^{-1}$ for the results in Table 3.3.

is also shown in Figure 3.4. As described earlier, it is not uncommon for this approach to be adopted in interpreting wet- and frosted-surface heat exchanger data. However, it is clear from the results that misapplication of Equation (3.42) can result in very large errors, especially at high relative humidity. It is also evident that if the *HA*-LMED method is used for dry or partially wet conditions, unrealistic predictions result. Under dry-surface conditions, the heat transfer coefficient calculated using the *UA*-LMTD method developed in this chapter approaches the true value (50 $Wm^{-2}K^{-1}$). For partially or fully wet conditions, although the variation in the local sensible heat ratio can be significant—as shown in Figure 3.5(a)—the error in the calculated heat transfer coefficient is small (less than 3%). The tolerance of the UA-LMTD method to variation in $dq_{a,s}/dq_a$ is probably because $q_{a,s}/q_a$ is weighted by the local heat transfer rates integrated over area. This weighting is apparent in Fig 3.5(a), where $q_{a,s}/q_a$ is closer to the local values near the heat exchanger inlet, where heat transfer rates are higher. This natural weighting by heat transfer rate, when extracting a rate coefficient, mitigates the impact of local variations, because the local values of $dq_{a,s}/dq_a$ departing the most from $q_{a,s}/q_a$ are weighted the least. Nevertheless, by comparing Figure 3.4(a) and 3.5(a) to 3.4(b) and 3.5(b), it is evident that the smaller the variation in $dq_{a,s}/dq_a$, the smaller the error in the calculated heat transfer coefficient by *UA*-LMTD.

Example results for frosting conditions are provided in Figure 3.6, where the calculated air-side heat transfer coefficients and variation in local sensible heat ratio are given for h_c/h_h=10. For all the conditions shown, the *UA*-LMTD method provides much more accurate results than the *HA*-LMED method.

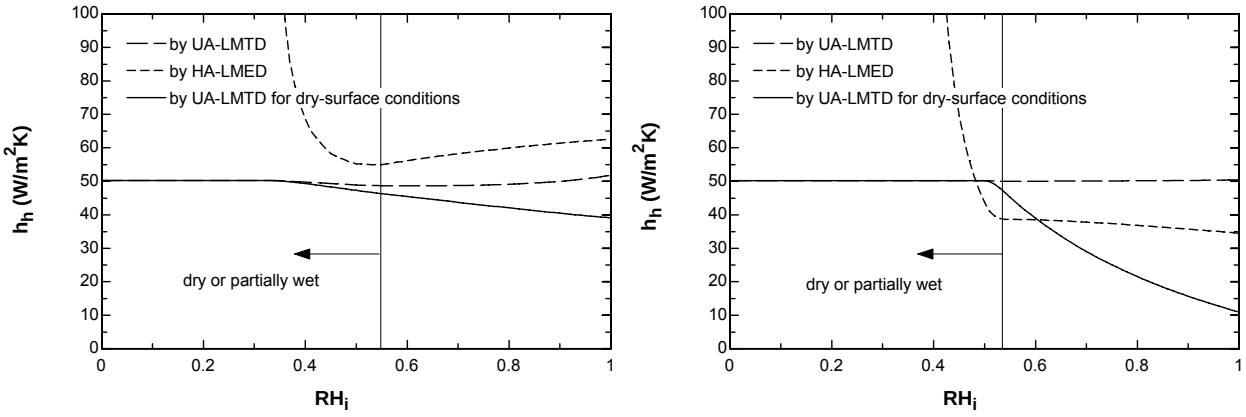

Figure 3.4 A comparison between the inferred air-side convective heat transfer coefficients from the methods of *HA*-LMED and *UA*-LMTD for air-conditioning conditions, when the true value is h_h=50 W/m^2K (with $T_{a,i}$ =27 ^oC and $T_{r,i}$ =7 ^oC): (a) h_c/h_h=10; (b) h_c/h_h=1.

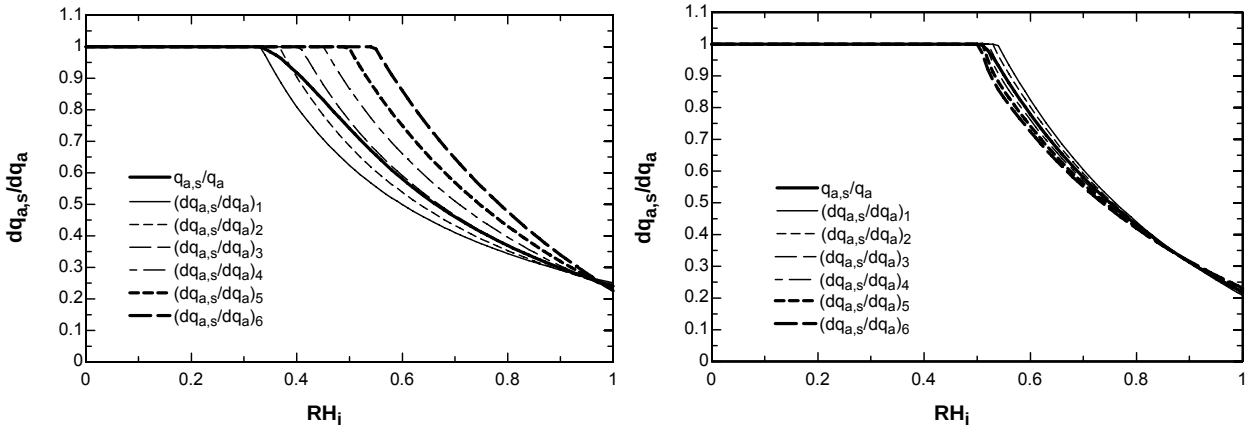

Figure 3.5 The variation in local sensible heat ratios corresponding to Figure 3.4.

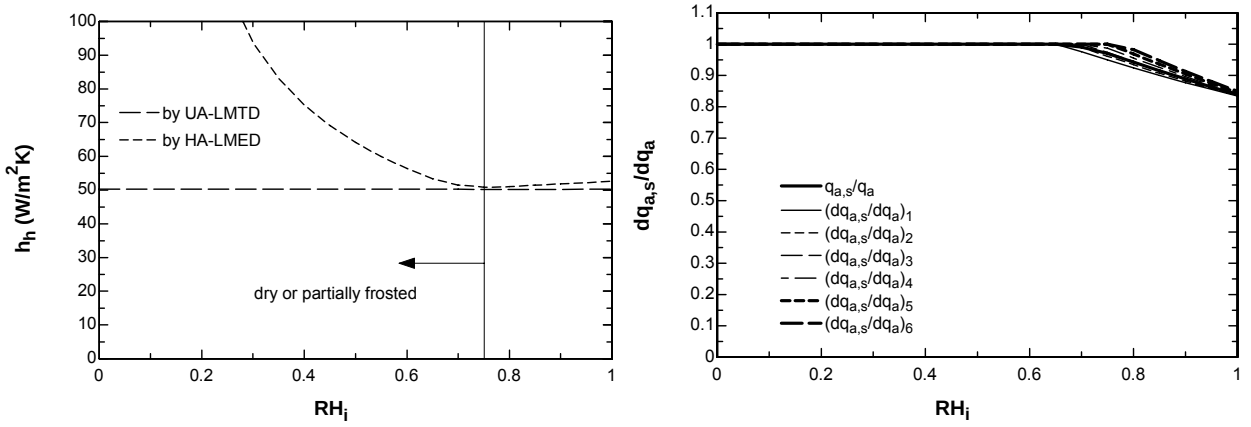

Figure 3.6 The calculated air-side convective heat transfer coefficients, when the true value is h_h=50 W/m^{2}K (a), and the variation in local sensible heat ratio (b) for low-refrigeration conditions ($T_{a,i}$ = -18 ^{o}C and $T_{r,i}$ = -23 ^{o}C) with h_c/h_h=10.

The maximum relative deviation in local sensible heat ratio with respect to the total sensible heat ratio, and the relative errors in the air-side heat transfer coefficient calculated using *HA*-LMED and *UA*-LMTD for conditions typical to air conditioning, heat pumping, medium-temperature refrigeration (M-R), and low-temperature refrigeration (L-R) are given in Table 3.3. Results are provided for three different h_c/h_h and two different total heat transfer areas. In general, the error in the method of *UA*-LMTD is within 3%, and is smaller than *HA*-LMED for all conditions.

Table 3.3 The relative errors in the air-side heat transfer coefficient calculated using HA-LMED and UA-LMTD for typical evaporator operating conditions (NA denotes partially wet/frosted or dry conditions; parameters provided in Table 3.2 were used unless otherwise specified)

Test conditions ($T_{r,i}$, $T_{a,i}$, $T_{dew,i}$) [°C]		$\frac{h_c}{h_h}$	A_h [m^2]	$\max\left\lvert\frac{dq_{a,s}/dq_a - q_{a,s}/q_a}{q_{a,s}/q_a}\right\rvert$ ×100 [%]	$\left\lvert\frac{h_{h,LMED}-h_h}{h_h}\right\rvert$ ×100 [%]	$\left\lvert\frac{h_{h,LMTD}-h_h}{h_h}\right\rvert$ ×100 [%]
Condensing	A-C (7, 27, 15)	10	0.6	5.5	7.0	0.11
			3	28	NA	2.5
		1	0.6	0	NA	0.0043
			3	0	NA	0.0013
	H-P (0, 8, 4)	10	0.6	3.0	7.2	0.055
			3	28	NA	1.8
		1	0.6	1.1	8.2	0.016
			3	5.9	5.7	0.17
		0.1	0.6	0	NA	0.032
			3	0	NA	0.032
Frosting	M-R (-7, 2, 0)	10	0.6	1.0	9.9	0.013
			3	13	9.5	0.95
		1	0.6	0.089	2.9	0.011
			3	0.36	0.67	0.023
		0.1	0.6	0	NA	0.032
			3	0	NA	0.032
	L-R (-23, -18, -20)	10	0.6	0.50	2.4	0.00021
			3	4.4	1.8	0.30
		1	0.6	0.15	0.37	0.011
			3	0.75	0.074	0.029
		0.1	0.6	0	NA	0.032
			3	0	NA	0.032
	H-P (-17, -8, -9)	10	0.6	0.25	6.8	0.0057
			3	3.5	6.8	0.25
		1	0.6	0.30	1.6	0.0084
			3	1.6	2.5	0.035
		0.1	0.6	0	NA	0.032
			3	9.5	NA	1.3

3.6 Conclusions

Valid *HA*-LMED and *UA*-LMTD methods for wet- and frosted-surface heat transfer were formulated. Fin-efficiency expressions for flat-tube heat exchangers with constant-area fins are provided for both methods, with improved expressions for frosted-surface conditions that consider two-dimensional conduction of heat in the frost layer. The *UA*-LMTD method is shown to provide the best results for dry, partially wet/frosted, and fully wet/frosted conditions. The *HA*-LMED method is only applicable to fully wet/frosting conditions. For all the conditions considered, the *UA*-LMTD method provided the value of the air-side convective heat transfer coefficient within 3% and is more accurate than the method of *HA*-LMED.

Chapter 4. Frost, Defrost, and Refrost and Its Impact on the Air-Side Thermal-Hydraulic Performance of Louvered-Fin, Flat-Tube Heat Exchangers

Nomenclature

A	area (m^2)
c_p	specific heat ($J\ kg^{-1}\ ºC^{-1}$)
D	hydraulic diameter (m)
F	cross-flow correction factor (-)
f	friction factor (-)
G	air-flow mass velocity ($kgm^{-2}s^{-1}$)
HB	heat balance (see Equation 4.3) (-)
H_f	fin height (m)
h	convective heat transfer coefficient ($Wm^{-2}ºC^{-1}$)
h_{sf}	latent heat of freezing (for water) ($kJ\ kg^{-1}$)
h_{sg}	latent heat of ablimation (for water vapor) ($J\ kg^{-1}$)
j	Colburn factor (-)
k	thermal conductivity ($Wm^{-1}ºC^{-1}$)
L_f	fin depth (m)
L_l	louver length (m)
m	mass (kg)
$\dot{m}$	mass flow/deposition rate (kg/s)
Q	defrost heat (J)
q	heat transfer rate (W)
T	temperature (ºC)
T_{dew}	dewpoint temperature (ºC)
t	half fin thickness (m)
UA	overall heat transfer coefficient ($W\ ºC^{-1}$)
V	heat exchanger volume (m^3)
ΔP_{HX}	pressure drop across heat exchanger (Pa)
ΔP_N	pressure drop across nozzle (Pa)
ΔT_{lm}	log-mean temperature difference (ºC)

Greek Symbols

α	absorption factor (-)
δ	thickness (m)
Γ	nondimensional frost thickness (-)
η	frosted-fin efficiency (-)
η_d	defrost efficiency (see Equation 4.25) (-)
η_h	overall surface efficiency (-)
ρ	density (kgm^{-3})

Subscripts

0	initial
a	moist air (i.e., dry air plus water vapor)
avg	average
c	cold-fluid side
corr	by correlation
d	defrost
f	frost
ff	free-flow
fi	fin
fr	frontal
fs	frost surface
h	hot-fluid side
HX	heat exchanger
i	inlet
l	latent heat
o	outlet
r	refrigerant
s	sensible heat
tot	total friction area
w	tube wall

4.1 Introduction

When louvered, folded-fin, flat-tube heat exchangers are used as evaporators, they will be subject to wet- and frosted-surface operating conditions. Under frosting conditions, the normal operation of the system will cause the heat exchanger to frost, defrost, and refrost in a cyclic manner. The thermal-hydraulic performance under such conditions and in particular the tolerance of the design to frosting, defrosting and refrosting must be considered if flat-tube designs are to serve as evaporators in these systems.

The focus of this chapter is on the operation of louvered, folded-fin, flat-tube heat exchangers under frosted-surface conditions. In most systems, the defrost method involves melting the frost while it is on the heat exchanger surface. In this study, a simulated hot-gas or reversed-cycle defrost is considered. Thus, the frost will be melted to liquid water, some of which will drain from the air-side surface during the defrost cycle, and then a new

frosting cycle will begin. This approach is intended to model the prevalent practice in heat-pump or refrigeration applications. In this chapter, thermal-hydraulic data for nine heat exchangers during the first frost growth cycle will be compared, and the performance of two heat exchangers under defrosting and refrosting conditions will be shown to analyze the effects of retained liquid water.

4.2 Experimental Method

4.2.1 Experimental Apparatus and Procedure

The experimental facility used to obtain performance data for microchannel heat exchangers under frosting conditions is shown in Figure 4.1 and was described in detail in an earlier report (Carlson *et al*., 2001). An open wind tunnel was placed inside an environmental chamber. The heat exchanger was positioned at the wind tunnel inlet, suspended on an electronic balance (± 3g) to measure the accumulated frost mass or remaining defrost water. Flexible plastic film was used to connect the heat exchanger to the tunnel, allowing the heat exchanger to move freely in the vertical direction for proper weight measurement, while providing a seal to eliminate mass leakage from the tunnel. A precooler was included in the chamber to set the chamber to the desired temperature prior to the initiation of an experiment.

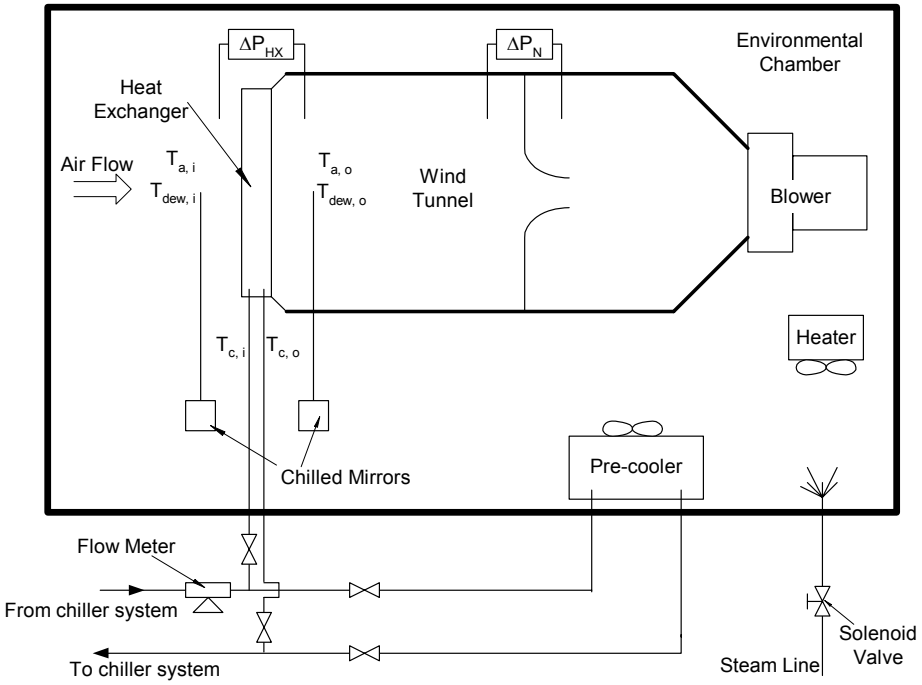

Figure 4.1 Facility schematic.

A variable-speed blower was used to provide the air flow, and the flow rate was measured using the pressure drop across standard nozzles. Pressure taps upstream and downstream of the nozzles were connected to a Setra model 239 pressure transducer (± 0.63 Pa), and allowed the air mass flow rate to be determined (± 1%) using the methods of ASHRAE Standard 33 (2000). The air temperature was controlled by regulating the power supplied to the heater located in the chamber, using a PID controller and type-T thermocouple (± 0.2 ºC) placed at the inlet of the heat exchanger. Humidification was provided by steam injection, and was maintained using a PID controller and

a General Eastern model D-2-SR chilled-mirror dew-point sensor (± 0.2 ºC). Two chilled-mirror sensors of the same model were used to obtain humidity data upstream and downstream of the specimen heat exchanger. Air temperatures were measured using thermocouple grids at the inlet and exit of the heat exchanger. The upstream thermocouple grid consisted of six type-T thermocouples in an evenly spaced array, and it provided upstream temperature data (± 0.2 ºC). The downstream array consisted of nine type-T thermocouples (± 0.2 ºC). The air-side pressure drop across the heat exchanger was measured with a Setra model 239 pressure transducer connected to static pressure taps as shown in Figure 4.1 (± 0.25 Pa).

Ethyl alcohol supplied by a gear pump was used as the coolant in the experimental loop. The alcohol flow was cooled by a chiller system (not shown in the schematic diagram of Figure 4.1), and the coolant temperature was regulated using an electrical heater and a PID controller. The coolant temperatures were measured using immersion thermocouple probes at the inlet and exit of the heat exchanger (± 0.2 ºC). The coolant was a single-phase flow of ethyl alchohol, and for the heat exchangers studied, the average temperature differences between the inlet and exit were 1.5-3.5 ˚C. Visually, the frost formation on the front face was evenly distributed except for heat exchanger #1, #2 and #4, for which more frost accumulated near the inlet header than near the exit header. A Coriolis-effect mass flow meter was used to measure the coolant flow rate (± 0.1 %).

A Campbell Scientific system, comprised of a data logger (CR23X) and a multiplexer (AM416), was used in the experiments. The instruments were sampled at 10-second intervals, and 6 measurements were averaged to provide the results in one-minute intervals, for the entire duration of the experiment. The results were written into a text file for subsequent analysis. Still and video images of frost growth were obtained using a CCD camera. A fiberscope (outer diameter 0.5 mm) was used to obtain images of frost growth on the fins. The fiberscope was inserted between fins and focused on a fixed location in the louver array.

At the initiation of an experiment, coolant was directed to the precooler only until the chamber was cooled to the desired temperature. After that, the coolant was diverted to the specimen heat exchanger, and performance data were collected. Unless otherwise noted, the data shown in this chapter were for frosting experiments conducted at constant air-inlet temperature (–1-2 ºC), refrigerant-inlet temperature (–10ºC), air-inlet humidity (80%), refrigerant mass flow rate, and blower frequency (to provide an initial face velocity of 1.0 m/s). During the course of an experiment the face velocity decreased, owing to the increase in air-side pressure drop associated with frost deposition.

Every refrosting cycle was arbitrarily chosen to last for one hour. After each frosting cycle, coolant was diverted to a bypass loop, where the coolant temperature was raised to 10ºC for defrosting. The defrost was terminated when real-time imaging indicated the frost was completely melted on the front face of the heat exchanger. For the two heat exchangers studied in cyclic experiments, all the defrosting cycles lasted 4 minutes for specimen #5, and 5 minutes for specimen #2. The blower was turned off during defrosting.

4.2.2 Heat Exchanger Geometry

Ten different heat exchangers were used in this study; all were circuited in a cross-flow configuration. The airflow was horizontal and the tubes were vertical. Specimen #3, #5, #7, #8, and #10 had a manifold only at the top of the core; whereas the other specimens had manifolds at the top and bottom of the core. The air-side geometry for

the heat exchangers is described in Table 4.1, with the structure of the heat exchanger and the louvered fin as illustrated in Figure 4.2. All of these specimens were "aged" in the sense that they were exposed to an indoor environment for years. For specimen #2-#10, the receding contact angles were about 30 degrees, and the advancing contact angles were about 100 degrees. Specimen #1 had lower contact angles of about 45 degrees.

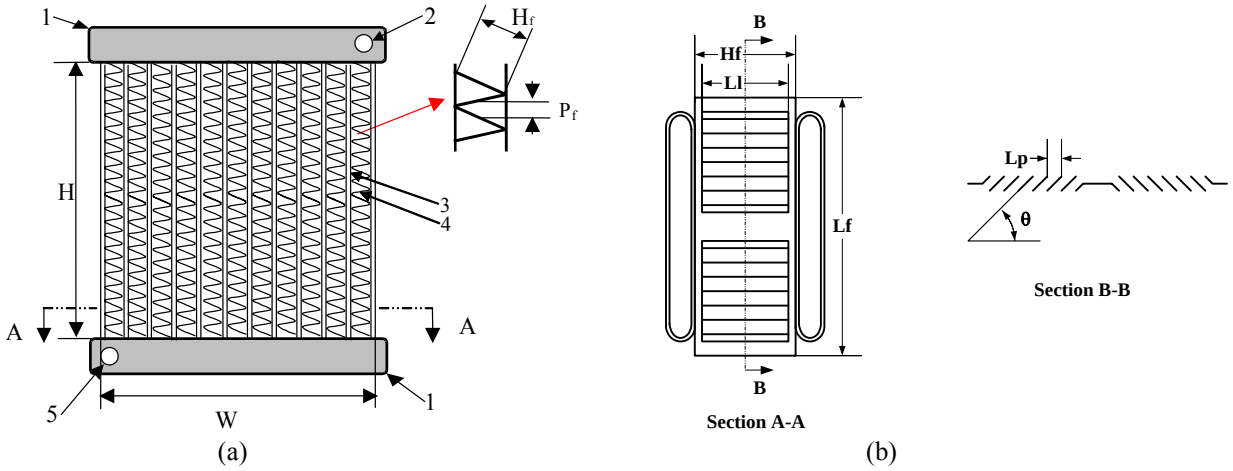

Figure 4.2 Structure of the heat exchanger: (a) a front view, with 1-manifold, 2-coolant inlet, 3-flat tubes, 4-louvered fins, and 5-coolant outlet; the air flow is into the page, and the coolant flow is from top to bottom; and (b) the louvered fin, section A-A illustrates the cross-section of the tubes with flat channels. Some specimens had circular microchannels.

Table 4.1 Heat exchanger geometric parameters

Specimens	**#1**	**#2**	**#3**	**#4**	**#5**	**#6**	**#7**	**#8**	**#9**	**#10**
Total air-side surface, A_o (m^2)	3.0	3.2	2.6	3.3	3.0	2.9	1.5	1.9	1.9	0.8
Heat exchanger width, W (mm)	300	330	216	356	279	300	300	300	300	300
Heat exchanger height, H (mm)	400	356	178	356	171	200	200	200	254	200
Fin depth, L_f (mm)	16.5	27.9	77.0	15.9	70.0	27.9	26.0	26.0	21.1	26.0
Fin pitch, P_f (mm)	1.49	2.12	2.12	1.06	1.95	1.06	2.10	1.40	1.59	5.10
Fin height, H_f (mm)	8.9	8.3	9.1	8.1	9.9	8.1	12.1	12.1	7.7	10.9
Fin thickness, (mm)	0.1	0.2	0.1	0.2	0.1	0.2	0.2	0.2	0.2	0.2
Louver length, L_l (mm)	7.50	5.90	6.25	5.90	8.4	5.9	9.0	9.0	5.9	9.0
Louver angle, θ (°)	23	27	30	27	30	27	26	26	27	26
Louver pitch, L_p (mm)	1.0	1.4	1.5	1.4	1.2	1.4	1.1	1.1	1.4	1.1
Number of louvers	2×6	2×8	2×20	2×4	2×20	2×8	2×7	2×7	2×6	2×7

4.2.3 Data Reduction Method

Basic data analysis includes determining the capacity of the heat exchanger, which is calculated from both the coolant and air streams, using

$$q_r = \dot{m}_r \left(c_{p_{r,o}} T_{r,o} - c_{p_{r,i}} T_{r,i} \right), \text{ and} \tag{4.1}$$

$$q_a = q_{a,s} + q_{a,l}, \text{ with} \tag{4.2a}$$

$$q_{a,s} = \left(\dot{m}_{a,i} c_{p_{a,i}} T_{a,i} - \dot{m}_{a,o} c_{p_{a,o}} T_{a,o} \right), \text{ and} \tag{4.2b}$$

$$q_{a,l} = \dot{m}_f h_{sg}. \tag{4.2c}$$

The heat balance error, as defined in below, was less than 10% for most of the test cases[3]:

$$HB = \frac{\left| q_r - q_a \right|}{\left(q_r + q_a \right)/2}. \tag{4.3}$$

In order to isolate the air-side convective heat transfer coefficient, h_h, two analysis methods are commonly adopted: one uses an overall heat conductance *UA* based on the logarithmic-mean temperature difference (LMTD), the other uses the so-called overall energy conductance *HA* based on the logarithmic-mean enthalpy difference (LMED). According to the analysis in Chapter 3, the *UA*-LMTD formulation is more accurate than the *HA*-LMED method, and thus is used to reduce the data. The *UA-LMTD* method used in this study is summarized below:

$$\frac{1}{UA} = \frac{1}{\eta_h h_h A_h} + \frac{1}{h_c A_c \left(q_{a,s} / q_a \right)}. \tag{4.4}$$

In Equation (4.4), the overall heat transfer coefficient is obtained from

$$UA = q_{a,s} / F \Delta T_{lm}, \tag{4.5}$$

where ΔT_{lm} is the log-mean temperature difference computed under the assumption of counter flow conditions, and F is the cross-flow correction factor to ΔT_{lm}. The values for F are obtained using correlations (see Appendix C) constructed from the plot of LMTD correction factor for a cross-flow heat exchanger developed by Bowman *et al.* (1940). The values are close to unity for all the test cases shown in this work.

On the air side, the overall surface efficiency η_h is obtained using

$$\eta_h = \eta \frac{A_{f\hat{i}}}{A_h} + \left(\frac{k_f / \delta_f}{h_h \left(q_a / q_{a,s} \right) + k_f / \delta_f} \right) \frac{A_h - A_{f\hat{i}}}{A_h}, \tag{4.6}$$

where η is the efficiency of a frosted fin:

$$\eta = \frac{2\lambda}{h_h \left(q_a / q_{a,s} \right) H_f \delta_f} \tanh\left(\frac{\lambda H_f}{2\delta_f} \right) \left(k_{fi} t + k_f \delta_f \right), \text{ where} \tag{4.7}$$

$$\lambda = \delta_f \sqrt{\frac{h_h \left(q_a / q_{a,s} \right)}{k_{fi} t + \delta_f \left[k_{fi} h_h \left(q_a / q_{a,s} \right) t / k_f + k_f \right]}}. \tag{4.8}$$

[3] For the smaller heat exchanger specimens #7, #9, and #10, the average heat balances were within 16%, 17%, and 25%, respectively.

In the above three equations, h_h is determined by iteration. Frost conductivity is obtained using the correlation provided by Lee *et al.* (1997):

$$k_f = 0.132 + 3.13\times10^{-4}\rho_{f,avg} + 1.6\times10^{-7}\rho_{f,avg}^2 . \quad (4.9)$$

The averaged frost density is calculated using

$$\rho_{f,avg} = m_f /(\delta_f A_h) . \quad (4.10)$$

With respect to the coolant side, the flow is laminar with Reynolds numbers between 100-400, and appropriate methods for calculating Nusselt number recommended by Shah and London (1978) are used according to the shape of the ducts and the flow conditions (hydrodynamically/thermally developing/developed flow). For specimen #1, a value of 4.36 for Nu_c is used for fully developed laminar flow in a circular duct[4], under the boundary condition of constant wall heat flux. For specimen #2-#4 and #6, Figure 35 in Shah and London (1978) is used to obtain the local value of *Nu* as a function of the length of thermal entrance region and *Pr*; the local value is in turn used to obtain an average value of Nu_c. The figure, developed from the numerical solution of Hwang and Fan (1964), is for simultaneously developing flow between parallel plates[5] under the boundary condition of constant wall heat flux. For specimen #7, #8, and #10, Table 54 in Shah and London (1978), the mean value of *Nu* as a function of the length of thermal entrance region and *Pr*, is used. The table, developed from the numerical solution of Wibulswas (1966), is for simultaneously developing flow in a rectangular duct (with an aspect ratio of 0.5) under the boundary condition of constant wall heat flux. For specimen #9, Table 63 in Shah and London (1978), the mean value of *Nu* as a function of the length of thermal entrance region and *Pr*, is used. The table, developed from the numerical solution of Wibulswas (1966), is for simultaneously developing flow in an equilateral triangular duct under the boundary condition of constant wall heat flux. Considering the error that might be introduced by the assumed boundary conditions and duct shapes, an uncertainty of ±10% is attributed to the tube-side Nusselt number when calculating the overall experimental uncertainty. Then, the coolant-side convective heat transfer coefficient is obtained by

$$h_c = \frac{Nu_c \cdot k_c}{D_c} . \quad (4.11)$$

Equations (4.1)-(4.11) are closed; i.e., the number of equations equals the number of unknowns, with measured variables taken as known. The data are used with this equation set to iterate to the correct h_h. Next, h_h is used to calculate the Stanton number and *j* factor:

$$\mathrm{St} = \frac{\mathrm{Nu}}{\mathrm{Re}\cdot\mathrm{Pr}} , \quad (4.12)$$

$$j = \mathrm{St}\cdot\mathrm{Pr}^{2/3} , \quad (4.13)$$

[4] The face area of specimen #1 is originally 0.36 m^2, but was reduced to 0.3 meters by 0.4 meters, with the peripheral area blocked and insulated, making the working region fully developed.
[5] For specimen #2-#4 and #6, the coolant flow paths are flat channels with aspect ratios of less than 0.1.

where Pr is Prandtl number. Note that the Reynolds number and Nusselt number in the above equations are all based on the hydraulic diameter, which is adjusted to account for frost deposition on the heat exchanger as time passes. The calculation of *f* factor is relatively simple as compared to *j* factor. It is obtained by

$$f = \frac{2\Delta P_{HX}\rho_{a,avg}}{G^2}\left(\frac{A_{ff}}{A_{tot}}\right) - \left(\frac{A_{ff}}{A_{tot}}\right)\left(\frac{\rho_{a,avg}}{\rho_i}\right)\left[\left(1+\sigma^2\right)\left(\frac{\rho_i}{\rho_o}-1\right)+\left(K_c + K_e\frac{\rho_i}{\rho_o}\right)\right], \tag{4.14}$$

where

$$\sigma = \frac{A_{ff}}{A_{fr}}, \tag{4.15}$$

K_c and K_e are the entrance and exit loss coefficients, and again, A_{ff} is adjusted in time to account for the deposition of frost. Using the plot of entrance and exit pressure loss coefficients provided by Kays and London (1964) for K_c and K_e, the second term on the right hand side of Equation (4.14) is estimated to account for 1% of the first term for a typical case, and is therefore neglected.

4.2.4 Frost Thickness Model

The frost thickness δ_f is measured from frost images captured with the CCD camera (a front view of the heat exchanger). An example image is provided in Figure 4.3(a). A frost thickness model is also developed, which integrates the thickness increment over time:

$$\delta_f = \int_0^\tau (1-\alpha)\dot{m}_f/(A_h\rho_{fs})\mathrm{d}t, \tag{4.16}$$

where τ is the duration of test, and α, the absorption factor, describes the fraction of freezing water vapor contributing to the densification of frost layer. Following Östin and Anderson (1991), an average value of 0.51 for α is used. The frost surface density is calculated using the empirical correlation presented by Hayashi *et al.* (1977),

$$\rho_{fs} = 650\exp(0.277\cdot T_{fs}). \tag{4.17}$$

The frost surface temperature T_{fs} in Equation (4.17) is obtained using the one-term approximation to the full-series solution of the midpoint temperature of the frost surface derived by Xia and Jacobi (2004),

$$T_{fs} = \frac{\left[1-\lambda^2\left(k_{fi}t\right)/\left(k_f\delta_f\right)\right]}{\cosh\left(\lambda H_f/2\delta_f\right)}\left[T_{w,avg}-T_{a,avg}\right]+T_{a,avg}, \tag{4.18}$$

where λ is calculated using Equation (4.8), and $T_{w,avg}$ is the average temperature of the outside tube wall. To calculate $T_{w,avg}$, consider the heat balance based on dA_c (or the corresponding dA_h):

$$\left(T_{w,avg}-T_{r,avg}\right)h_c dA_c = \left(T_{a,avg}-T_{w,avg}\right)h_h\left(q_a/q_{a,s}\right)dA_h\eta_h. \tag{4.19}$$

After collecting and rearranging terms, and consider dA_c/dA_h=A_c/A_h, we have

$$T_{w,avg} = \frac{T_{a,avg}h_h\left(q_a/q_{a,s}\right)\eta_h A_h + T_{r,avg}h_c A_c}{h_h\left(q_a/q_{a,s}\right)\eta_h A_h + h_c A_c}. \tag{4.20}$$

Thus, the two methods for determining frost thickness are from images of the heat exchanger face and from the model described above. The frost thicknesses as obtained from these methods are compared in Figure 4.3(b).

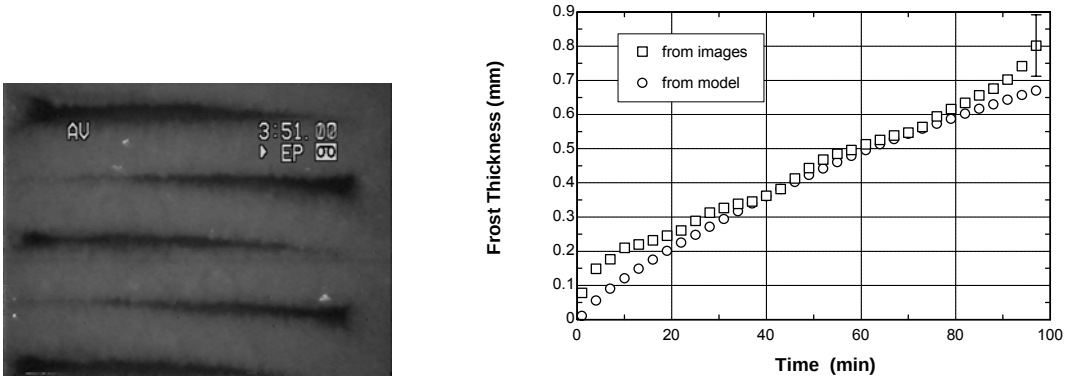

(a) (b)

Figure 4.3 Frost growth: (a) frost image recorded by focusing a CCD camera on the front face of the heat exchanger, and (b) a comparison of the frost thickness obtained with different methods.

In the first method, the exact frost boundary is difficult to determine, contributing to the discrepancy, especially early in the growth cycle. Moreover, images of the leading edge of the fin might not be representative of the entire heat exchanger. The drawback to the second method is that it is dependent on the correlations used for frost density and conductivity, and these properties are generally hard to predict.

4.3 Results

4.3.1 Data for Different Geometries during the First Frost-Growth Cycle

The thermal-hydraulic performances during the first frost-growth cycle are compared for specimen #1-#4 and #6-#10 (specimen #5 is not included in this comparison because the tube-side geometry is unknown). The overall heat transfer coefficient UA, the air-side heat transfer coefficients h_h, the Reynolds number, and j and f factors are normalized with the initial value, as listed in Table 4.2. In the table, j_{corr} is a predicted initial value of j factor obtained using the correlation developed by Chang and Wang (1997): [6]

$$j_{corr} = \mathrm{Re}_{Lp}^{-0.49}\left(\frac{\theta}{90}\right)^{0.27}\left(\frac{P_f}{L_p}\right)^{-0.14}\left(\frac{H_f}{L_p}\right)^{-0.29}\left(\frac{T_d}{L_p}\right)^{-0.23}\left(\frac{L_l}{L_p}\right)^{0.68}\left(\frac{T_p}{L_p}\right)^{-0.28}\left(\frac{F_t}{L_p}\right)^{-0.05} . \quad (4.21)$$

where the geometry is as illustrated in Figure 4.2, and T_d, T_p and F_t are tube depth, tube pitch and fin thickness.

[6] The value for specimen #10 is not listed, since its fin pitch (5.1 mm) far exceeds the maximum value (3.33 mm) among the specimens Chang and Wang used to develop the correlation.

Table 4.2 The initial and average values of performance data

Specimens	#1	#2	#3	#4	#6	#7	#8	#9	#10
UA_0 ($W\ ^oC^{-1}$)	114 ±5	153 ±5	63 ±3	111 ±4	99 ±4	58 ±3	65 ±4	102 ±5	23 ±2
h_{h0} ($Wm^{-2}\ ^oC^{-1}$)	78 ±10	83 ±9	46 ±6	88 ±14	87 ±18	70 ±7	70 ±10	71 ±6	36 ±7
Re_0	200	330	450	175	192	350	284	236	750
j_0	0.040 ±.005	0.034 ±.004	0.016 ±.004	0.037 ±.006	0.032 ±.007	0.035 ±.004	0.028 ±.007	0.033 ±.003	0.018 ±.004
j_{corr}	0.042	0.030	0.020	0.038	0.031	0.038	0.035	0.036	
f_0	0.1343 ±.0002	0.1322 ±.0004	0.1310 ±.0005	0.182 ±.001	0.186 ±.001	0.179 ±.001	0.167 ±.002	0.272 ±.002	0.0533 ±.0002
UA_{avg}/V ($kW\ ^oC^{-1}\ m^{-3}$)	46.8	35.8	10.1	40.1	38.0	29.8	32.1	41.5	14.4

Air-side heat transfer coefficient. The air-side heat transfer coefficients decreased as frost accumulated, as can be seen in Figure 4.4(a), where the normalized coefficients for specimen #1 to #4 are shown. Figure 4.4(b) shows the normalized Reynolds number based on the hydraulic diameter of the air-flow path. The decrease in Reynolds numbers is mainly due to the decrease in air mass flow rate, caused by increasing pressure drop across the heat exchanger with a constant blower speed. The decreasing Reynolds number contributes to the dramatic reduction in the air-side heat transfer coefficient. Equation (4.21) suggests $h_h \propto Re^{\sim 0.5}$, and thus cutting the Reynolds number in half would reduce the convection coefficient by about 30%. For specimen #3 and specimen #4, the Reynolds numbers decreased by 23% and 13%, but a reduction in convection coefficient by 90% and 70%, respectively, was measured. Clearly there are other mechanisms acting to further reduce the air-side convective heat transfer as frost accumulates on the surface.

It is interesting to note that the Reynolds numbers for the four heat exchangers did not change much during the first 20 minutes, but a reduction in the air-side heat transfer coefficient is initiated at the start of the frost-growth cycle. This behavior and images from the fiberscope showing how frost grows on the louvered fin help to explain how frost accumulation modifies the flow and reduces the convection coefficient. A series of three images recorded with the fiberscope is provided in Fig 4.4(c), showing the evolution of the frost layer. From this image it is clear that for this geometry frost grows to completely block the inter-louver gap (normally by the 25th minute). Thus, from the beginning of an experiment, the louver gap is progressively blocked, and the flow becomes less louver directed and more duct directed as time passes—by about the 25th minute the louver gap is closed and the flow is purely duct directed. The change from louver-directed to duct-directed flow is well known to decrease the heat transfer coefficient by vitiating the boundary-layer-restarting effect of the louvers. In support of this explanation, consider that if the flow becomes duct-directed, an estimate of the heat transfer coefficient can be obtained by considering the flow as developing flow in an isothermal rectangular duct. Then, from Wibulswas (1966) (per Shah and London, 1978, Table 52), upon louver-gap blockage the estimated convection coefficients, h_h, for specimens #1 and #2 are 42 and 68 $W/(m^2K)$, respectively. By comparing these values to the dry-surface heat transfer coefficients for these

specimens, we would anticipate that duct-directed flow would reduce h_h by 18% and 56%, respectively, for the two specimens. From Figure 4.4(a), it is clear that the measured reductions were very close to this expectation, at 16% and 40%, respectively. Thus, it appears that frost blockage of the louver gap, and the resulting duct-directed flow, is primarily responsible for the performance reduction.

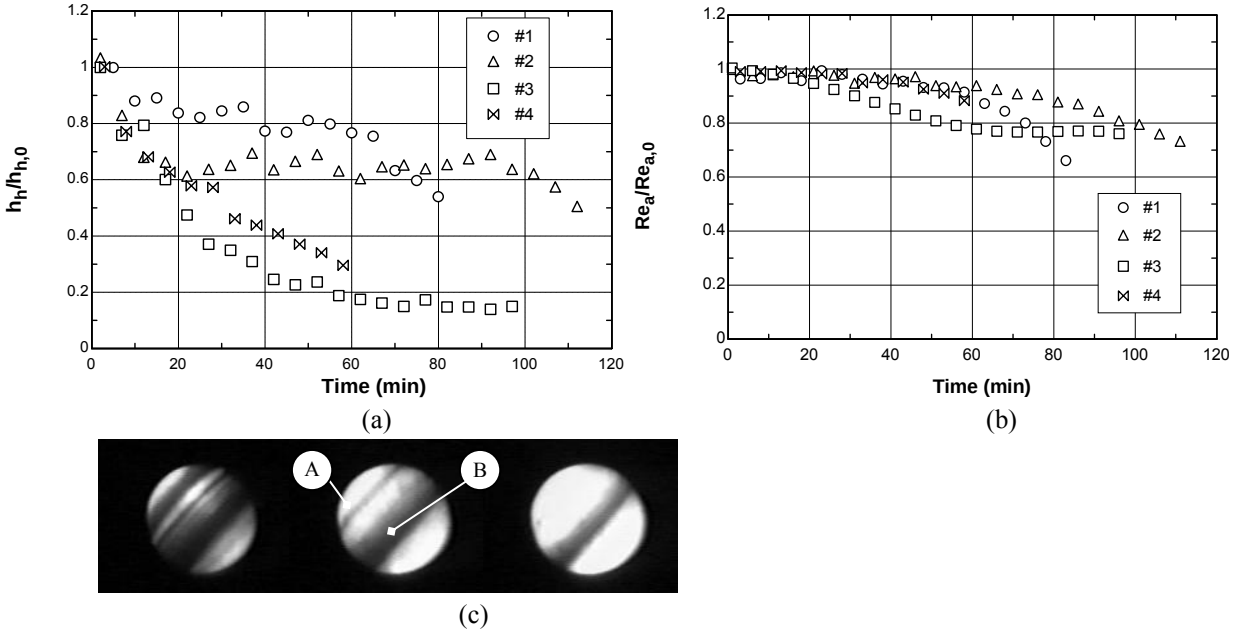

Figure 4.4 Air-side heat transfer coefficient and the main reasons that cause the decrease in the coefficient: (a) Air-side heat transfer coefficient; (b) Reynolds number; (c) images by a 0.5mm fiberscope, where A and B indicate louver gap and fin gap.

Heat transfer and pressure drop. The heat transfer and pressure drop data for eight different fin geometries are shown in Figure 4.5. A decrease in the overall heat conductance and increase in the pressure drop can be observed. The behaviors of the nine heat exchangers are quite different, thus more generalized results are desired (*j* and *f* factors are more general). In Figure 4.5(a), the difference in the trend of pressure drop for specimen #3 is mainly due to its large fin depth. As frost accumulates, the decrease in heat transfer is more significant for large fin depth (see Figure 4.5c), and as expected according to the analogy between heat and mass transfer, its frost growth rate decreases dramatically (not shown here). As a consequence, the pressure drop increase rate decreases because of the lower frost growth rate. For specimens #6 and #9, the pressure drop increase rates also start to decrease towards the end when the reduction in their heat transfer rates has become large. The other heat exchangers might have the similar behavior if they were kept operating long enough and their heat transfer rates dropped low enough.

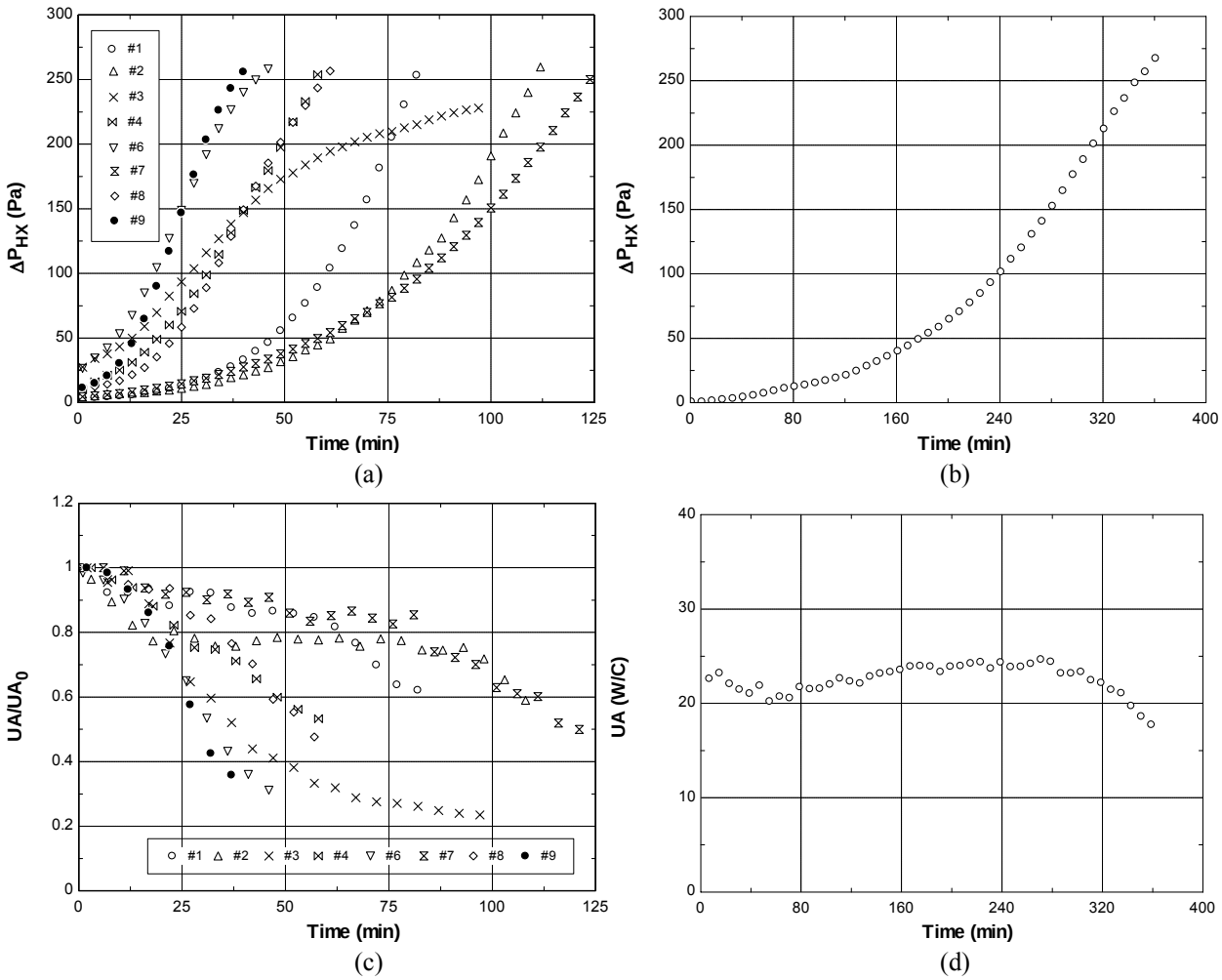

Figure 4.5 Heat transfer and pressure drop data for nine different fin geometries: (a) pressure drop for a fin pitch within 1.06-2.12 mm; (b) pressure drop for a fin pitch of 5.1 mm (specimen #10); (c) heat transfer for a fin pitch within 1.06-2.12 mm; (d) heat transfer for a fin pitch of 5.1 mm (specimen #10).

The average values of UA per unit volume of heat exchanger are also listed in Table 4.2, where V is the volume of the heat exchanger, and UA_{avg} is calculated as

$$UA_{avg} = \frac{1}{\tau}\int_0^{\tau} UA\,\mathrm{d}t\,, \tag{4.22}$$

where τ is the duration of the frost-growth period. Specimen #3, with a significantly larger heat exchanger depth, has the lowest UA_{ave}/V. The less compact specimen #10 has the second smallest UA_{ave}/V. Among the other seven heat exchangers, specimen #7 has a slightly lower UA_{ave}/V; however, it should be noted that if the initiation of defrost were determined by the pressure drop reaching a preset value (a common control strategy), specimen #7 would require the fewest defrost cycles over a specified time period. For the purpose of comparison, a copper-tube, aluminum-finned evaporator with a fin pitch of 7.9 mm, operating under similar conditions (with the same blower, see Carlson *et al*. 2001), had a UA_{ave}/V of only 4 kW/(ºC m^3). For both the plain-fin and louver-fin geometry UA decreases in time, and the less compact geometry is more frost tolerant; however, the more compact geometry starts

a cooling cycle with a *UA* that is significantly higher. The plain-fin heat exchanger with a 7.9 mm fin pitch had a pressure drop of 50 Pa after 10 hours of operation, and in general less compact heat exchangers (such as specimen #10) show a lower rate of pressure drop increase than do more compact ones under similar conditions.

j and *f* factors. The *j* and *f* factors for specimen #1, 2, 4-9 are provided in Figure 4.6. Generalized results for specimen #3 and #10 are not attempted due to their low heat transfer performance. The x-coordinate is the nondimensional frost thickness Γ, which is defined as frost thickness over fin pitch. The uncertainty of *j* factor is less than ±0.007, and the uncertainty of *f* factor is less than ±0.001 initially, and increases to ±0.02 at a Γ of 0.1. As frost grows, the normalized *j* factor decreases, with similar behavior for a fin pitch within 1.40-2.12 mm. This behavior is encouraging with respect to developing a generalized correlation for this type of heat exchanger operating under frosting conditions—the widely disparate geometries and *UA* performances notwithstanding, j/j_o versus Γ appears to 'collapse' fairly well. For more compact geometries (specimen #4 and #6 with a fin pitch of 1.06 mm), the behavior is slightly different. Based on the data, correlations were developed for these two groups as following (the intercepts were forced to be 1.0):

$$j/j_0 = 1.0 - 3.020\Gamma + 2.719\Gamma^2 \quad , P_f = 1.40\text{-}2.12 \text{ mm } (R^2 = 0.91); \text{ and} \qquad (4.23a)$$

$$j/j_0 = 1.0 - 6.870\Gamma + 14.336\Gamma^2 \quad , P_f = 1.06 \text{ mm } (R^2 = 0.99). \qquad (4.23b)$$

The effects on *f* factor are difficult to analyze, especially under very heavy frosting conditions, because the uncertainty in *f*-factor measurement (mainly due to the uncertainty in frost thickness measurement) is magnified about 100 times by the increasing pressure drop. However, the behavior of the heat exchanger under very heavy frosting conditions is less important than at other times, because it operates with heavy frost for short period of time.

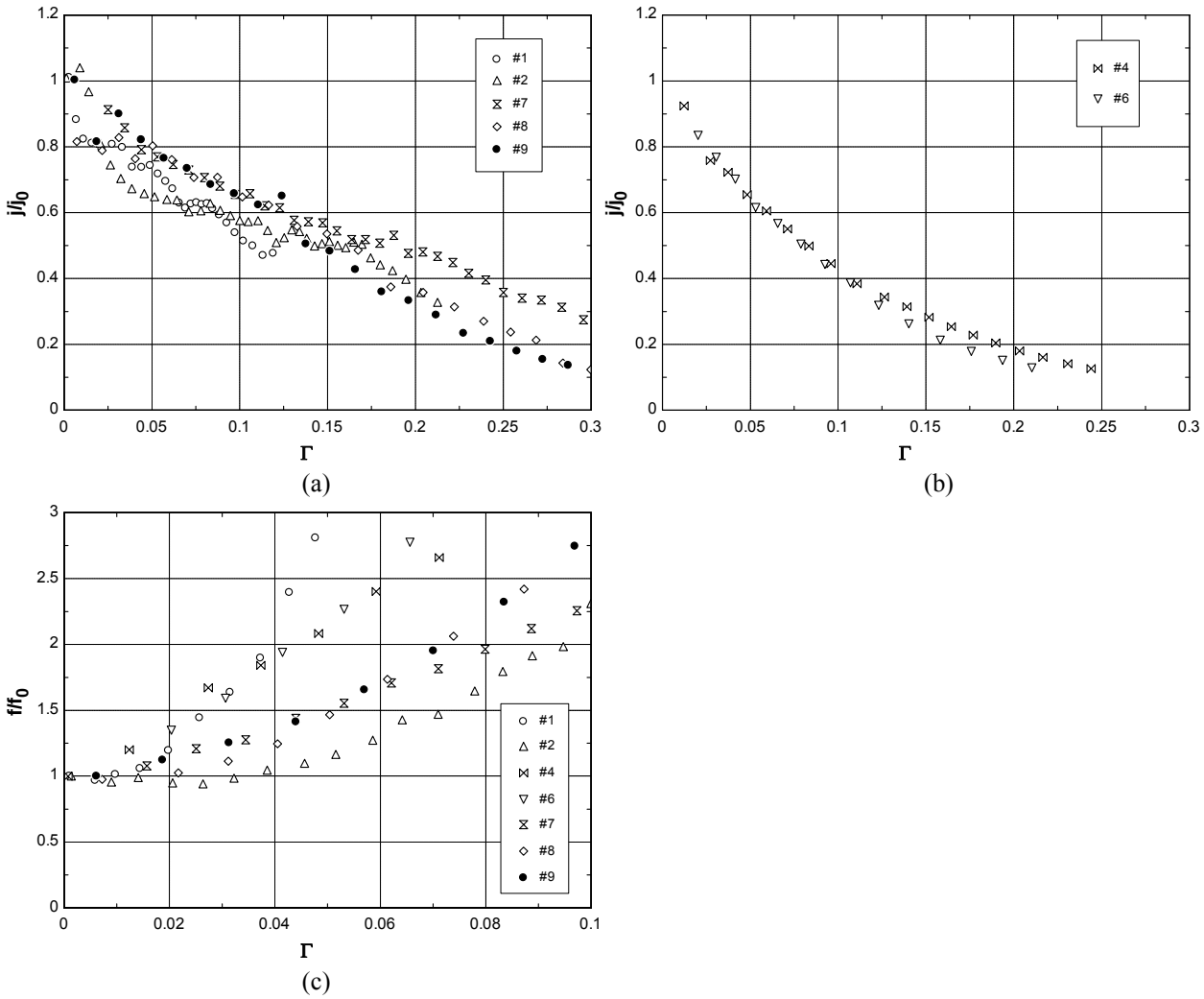

Figure 4.6 Thermal-hydraulic performance for different fin geometries: (a) *j* factor for a fin pitch within 1.40-2.12 mm; (b) *j* factor for a fin pitch of 1.06 mm; (c) *f* factor.

4.3.2 Data for Sequential Frost-Growth Cycles

In this section, the heat transfer, pressure drop, and frost/water retention data for heat exchangers #2 and #5 during sequential frost-growth cycles will be analyzed. The experiments were conducted at the same constant air- and refrigerant-inlet temperature, inlet humidity, refrigerant mass flow rate, and blower frequency.

Amount of frost accumulation and water retention. The weight of the heat exchanger was measured using an electronic balance. The total frost mass on the heat exchanger at the end of each frosting cycle ($t_{i,f}$, i=1-5) and the liquid water retained at the end of each defrosting cycle ($t_{i,d}$, i=1-5) are shown in Figure 4.7. The data are presented in terms of mass per unit of heat transfer area, in order to facilitate more direct comparisons between the heat exchangers. As shown in Figure 4.7, the water retention at the end of a defrost reached an asymptotic value after the fourth cycle, and the water retention per unit area of specimen #5 was about 25% higher than that of #2 after the second cycle. The frost accumulation per unit area reached an asymptote after the fourth cycle. The accumulated frost per unit area of specimen #5 was higher than that of #2 after the third cycle. The accumulated frost is

composed of the newly deposited frost and the frozen water from the previous defrosting cycle. By comparing the values at $t_{i,f}$'s and at $t_{i,d}$'s, it is apparent the differences in the total accumulated frost mass were mainly due to differences in water retention. The difference in water retention could be a combined effect of the different fin geometry and the different construction of coil at the bottom. As shown later, although specimen #2 retained less water than specimen #5, specimen #2 exhibited much more significant performance degradation than did specimen #5 in the subsequent frosting cycles as compared to the first frosting cycle.

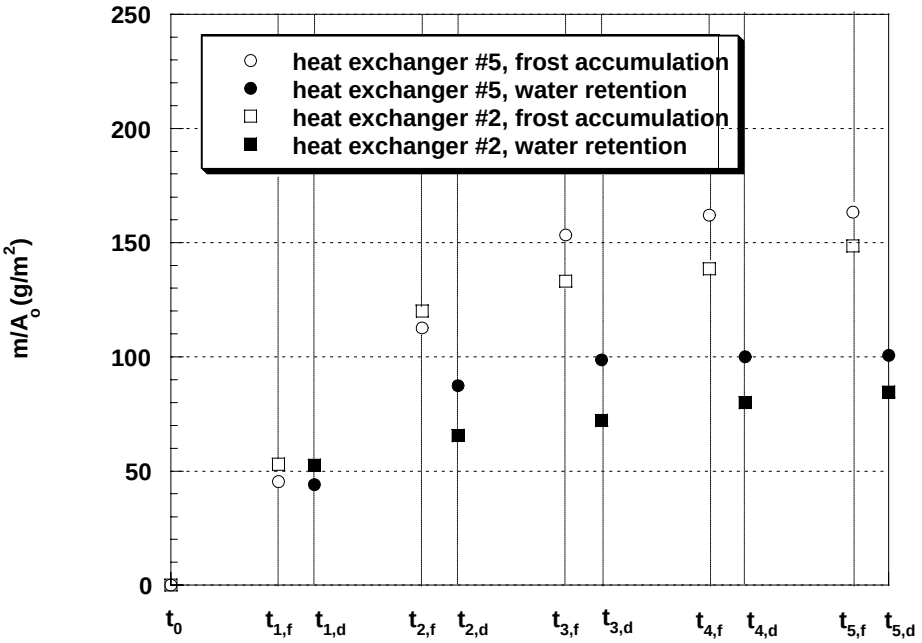

Figure 4.7 Added weight per unit area on the heat exchangers.

Images of heat exchanger during defrost and refrost. Images of the heat exchanger face were captured using a CCD camera. Images of the heat exchangers between two successive defrosting cycles are shown in Figure 4.8, with three complete fins and the tube on one side of the fins appearing in the field of view. Bright spots in the images (Figure 4.8a) are reflections from water droplets in the melting frost. The corner formed by two adjacent fins hindered the drainage of the droplets, as can be seen in Figure 4.8(b), where a droplet was held in a corner at the end of the defrosting cycle. As the next frosting cycle ensued, the droplets froze directly into ice, and their volume expanded (see Figure 4.8c). Later, frost grew on that frozen ice. At the end of the frosting cycle, the accumulated frost almost totally blocked the air-flow passage (as can be seen in Figure 4.8d). The melting of the ice shown in Figure 4.8(e) (the substance that is slush-like in appearance) was much slower than the melting of the frost. At the end of this cycle (Figure 4.8f), no droplets were held in the fin corners in the field of view, but it is possible that some droplets were held at other places out of view.

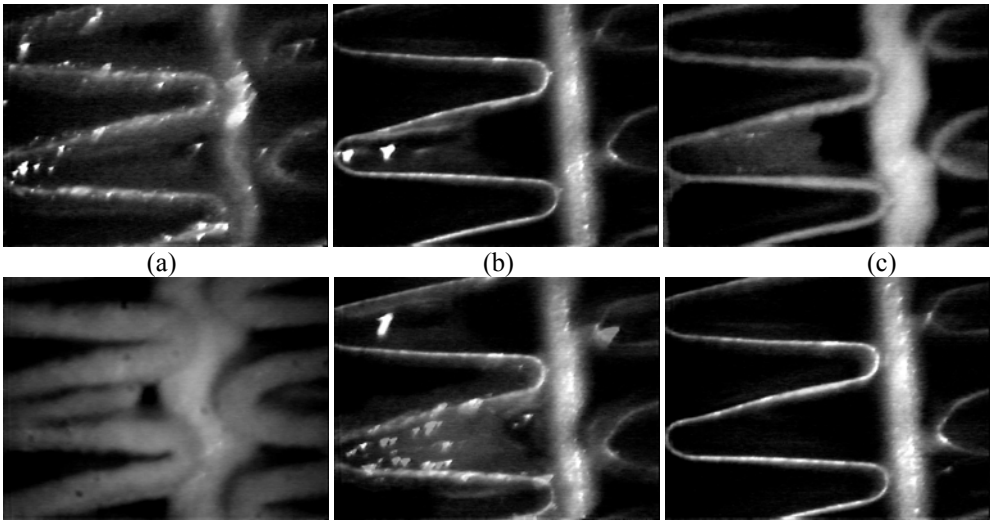

Figure 4.8 Images of fins between two successive defrosting cycles: (a) melting frost; (b) end of defrost; (c) refrost; (d) end of refrost; (e) re-melting; (f) end of second defrost.

In addition to providing a site for future frost growth, droplets retained during the defrost cycle increase the pressure drop across the heat exchanger. Figure 4.9 shows images selected from each frosting cycle, corresponding to the same pressure drop across the heat exchanger. At the same pressure drop, the frost of the first frosting cycle (starting from a dry surface) appears thicker than in subsequent frost cycles. As demonstrated in Figure 4.7, after the third cycle the amount of water remaining on the heat exchanger at the end of a defrost does not change markedly. As seen in Figure 4.9, the differences in the frost thickness were also small after the third cycle. The pressure drop in the refrosting cases must have been deleteriously affected by the retained water and resulting frost distribution.

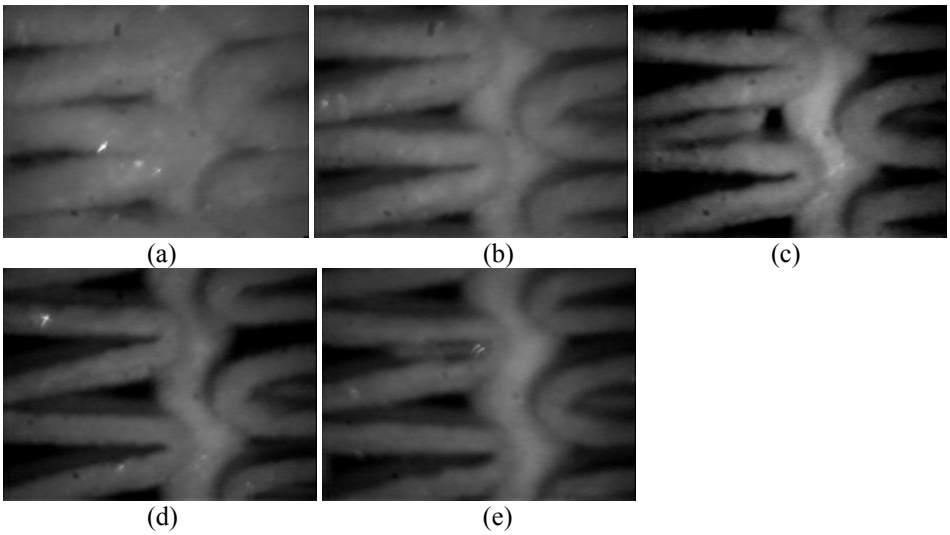

Figure 4.9 Frost thickness corresponding to the same pressure drop across the heat exchanger during each frosting cycle: (a) 1st; (b) 2nd; (c) 3rd; (d) 4th; (e) 5th.

Defrost heat and efficiency. The defrost heat was supplied by circulating warm liquid through heat exchangers. The total defrost heat was calculated using Equation (4.1), integrated over the time period of defrost.

The defrost heat supplied per unit of heat transfer area in each defrosting cycle is shown in Figure 4.10. The required heat does not change much after the third cycle. The heat supplied is mainly used to melt the frost, with small amounts consumed in warming up the heat exchanger and the frost layer, and a small amount lost to the ambient air by convection, i.e.

$$Q_d = Q_{f,l} + Q_{HX} + Q_{f,s} + Q_a \,. \tag{4.24}$$

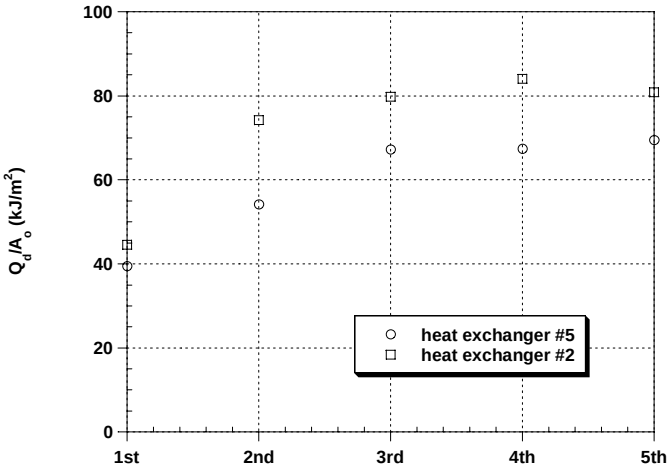

Figure 4.10 Defrost heat supplied in each defrosting cycle.

Take specimen #5 as an example, during the fifth defrosting cycle, $Q_{f,l}$, Q_{HX}, $Q_{f,s}$ and Q_a are estimated to account for 78%, 17%, 4%, and 1% of Q_d, respectively. In order to compare the effectiveness of defrost on the two heat exchangers, a defrost efficiency is defined as the ratio of total melting latent heat of frost at 0ºC to the defrost heat, i.e.

$$\eta_d = \frac{m_f h_{sf}}{Q_d} \,. \tag{4.25}$$

The defrost efficiencies for each defrosting cycle for the two specimens are shown in Figure 4.11. The defrost efficiency of specimen #5 is about 20% higher than #2 after the third defrosting cycle. The weight of heat exchanger #5 is 13% smaller than that of #2, which implies that the heat consumed in warming up the metal of heat exchanger #5 is about 13% less than that for #2. That smaller core mass could be the main reason for a higher defrost efficiency. Easier drainage and slush sliding from the heat exchanger could also contribute.

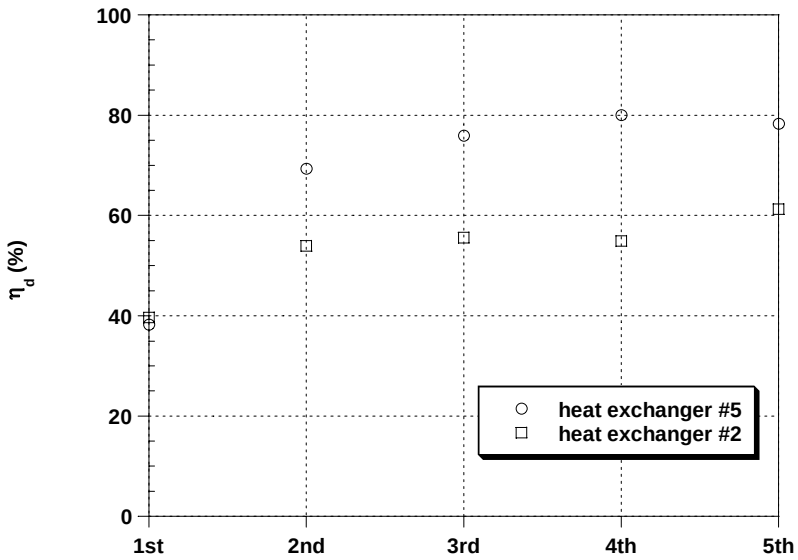

Figure 4.11 Defrost efficiency for each defrosting cycle.

Pressure drop during frosting cycles. The pressure drop data for each frosting cycle for the two heat exchangers are shown in Figure 4.12. For specimen #5, the end pressure drop of the second cycle is higher than the first cycle. The pressure drop increase rate is even higher in the third cycle, after which the data of each cycle are highly periodic. The situation is similar for specimen #2, but the differences in the first 3 cycles are more profound. The results, along with the discussion of Figure 4.9, suggest retained water and the redistribution of frost with cycling is more important for specimen #2, perhaps because it has a much shorter flow depth.

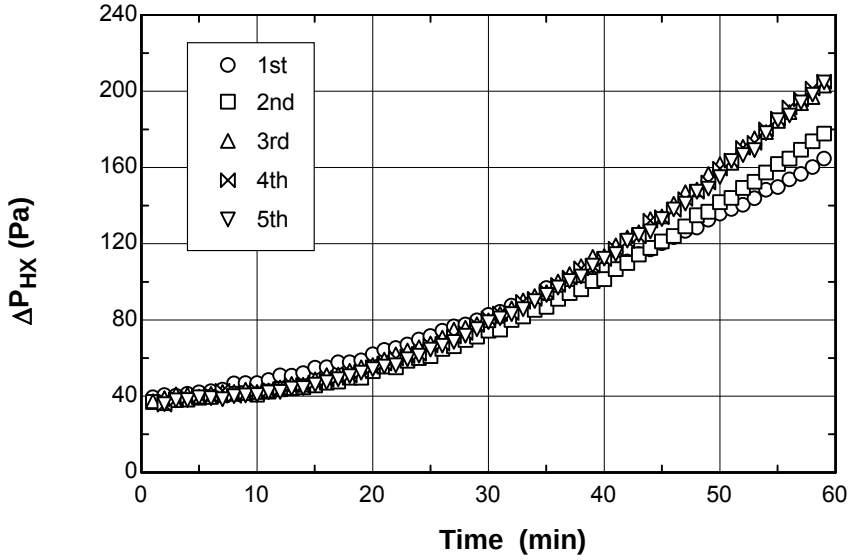

(a)

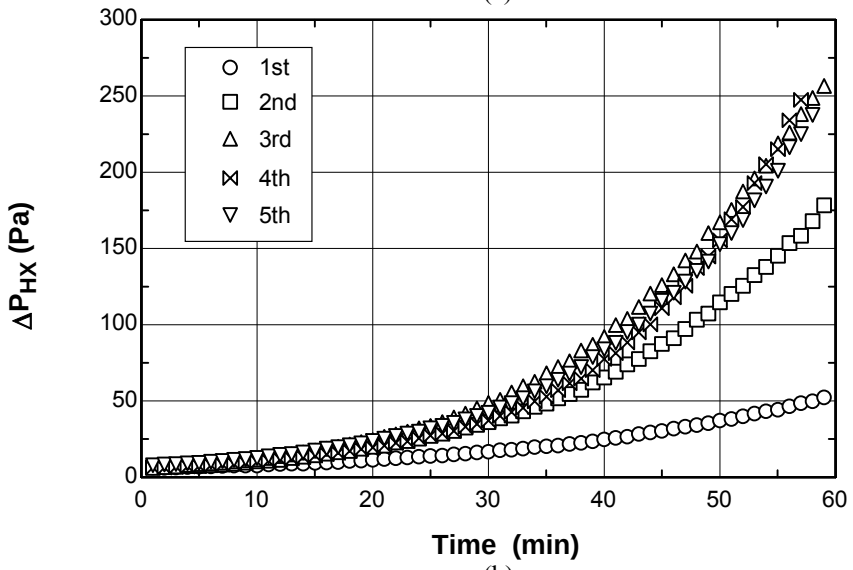

(b)

Figure 4.12 Pressure drop data for 5 successive frosting cycles: (a) heat exchanger #5; (b) heat exchanger #2.

Heat transfer during frosting cycles. The overall heat transfer coefficient during each frosting cycle is shown in Figure 4.13. For clarity, the figure only shows data at five-minute intervals. For specimen #5, the heat transfer coefficient did not change much between each frosting cycle. For specimen #2, the overall trend during the first four cycles shows a reduction in the heat transfer coefficient. Very little change occurs after the fourth cycle. It is clear that the heat transfer performance of specimen #2 is also greatly impacted by retained water and changes in the frost deposition pattern associated with water redistribution. Again, these effects may be due to the short flow length of specimen #2. Overall, the flow is less developed for this shorter flow depth—the boundary layers are on average thinner for specimen #2 than for specimen #5. Thus, protuberances of a fixed size, say retained droplets and growing frost, have a much more profound effect than for the more developed flow of specimen #5.

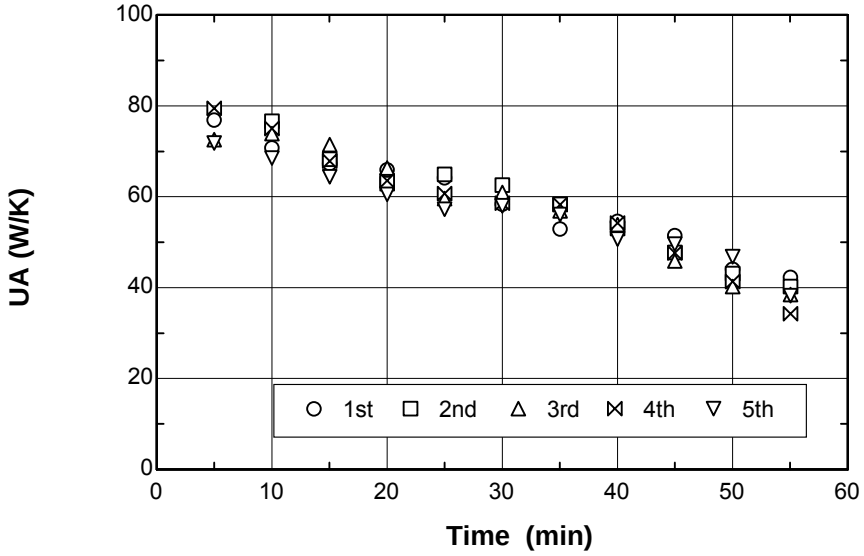

(a)

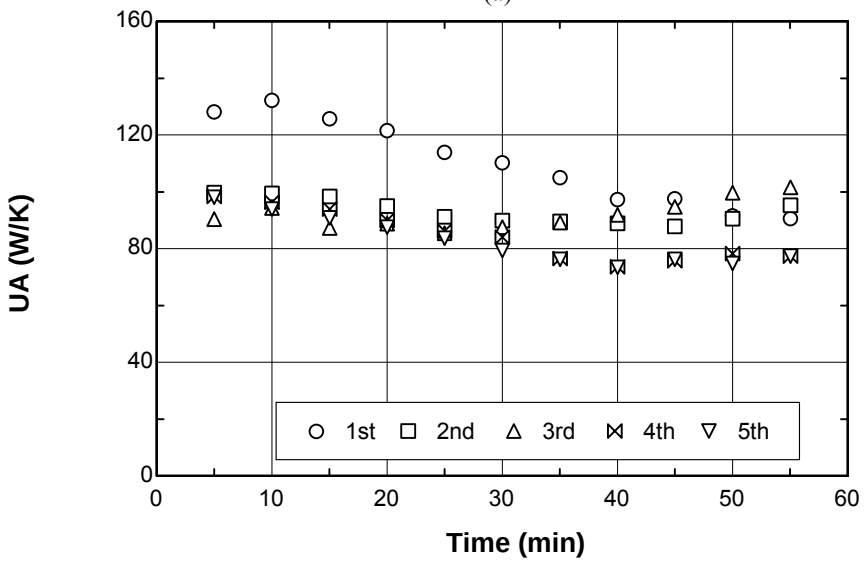

(b)

Figure 4.13 Heat transfer data for 5 successive frosting cycles: (a) heat exchanger #5; (b) heat exchanger #2.

4.3.3 Data for Different Environmental Conditions

Some frosting tests were conducted under several different environmental conditions on specimen #7-9, as listed in Table 4.3, with the air inlet temperature at -1 ºC. Data for Condition A have been shown in Section 4.3.1. The *j* factors for Condition B, C, and D are shown in Figure 4.14 in a similar way as in Section 4.3.1. Correlations were also developed for these conditions (for a fin pitch of 1.4-2.1 mm):

$$j/j_0 = 1.0 - 2.804\Gamma + 4.233\Gamma^2 \text{, Condition B } (R^2=0.89); \quad (4.26a)$$

$$j/j_0 = 1.0 - 4.612\Gamma + 11.343\Gamma^2 \text{, Condition C } (R^2=0.93); \text{ and} \quad (4.26b)$$

$$j/j_0 = 1.0 - 5.527\Gamma + 12.093\Gamma^2 \text{, Condition D } (R^2=0.96). \quad (4.26c)$$

Table 4.3 Environmental conditions

	Refrigerant-inlet temperature (°C)	Air-inlet humidity	Initial air face velocity (m/s)
A	-10	80%	1.0
B	-15	80%	2.0
C	-10	80%	2.0
D	-10	70%	2.0

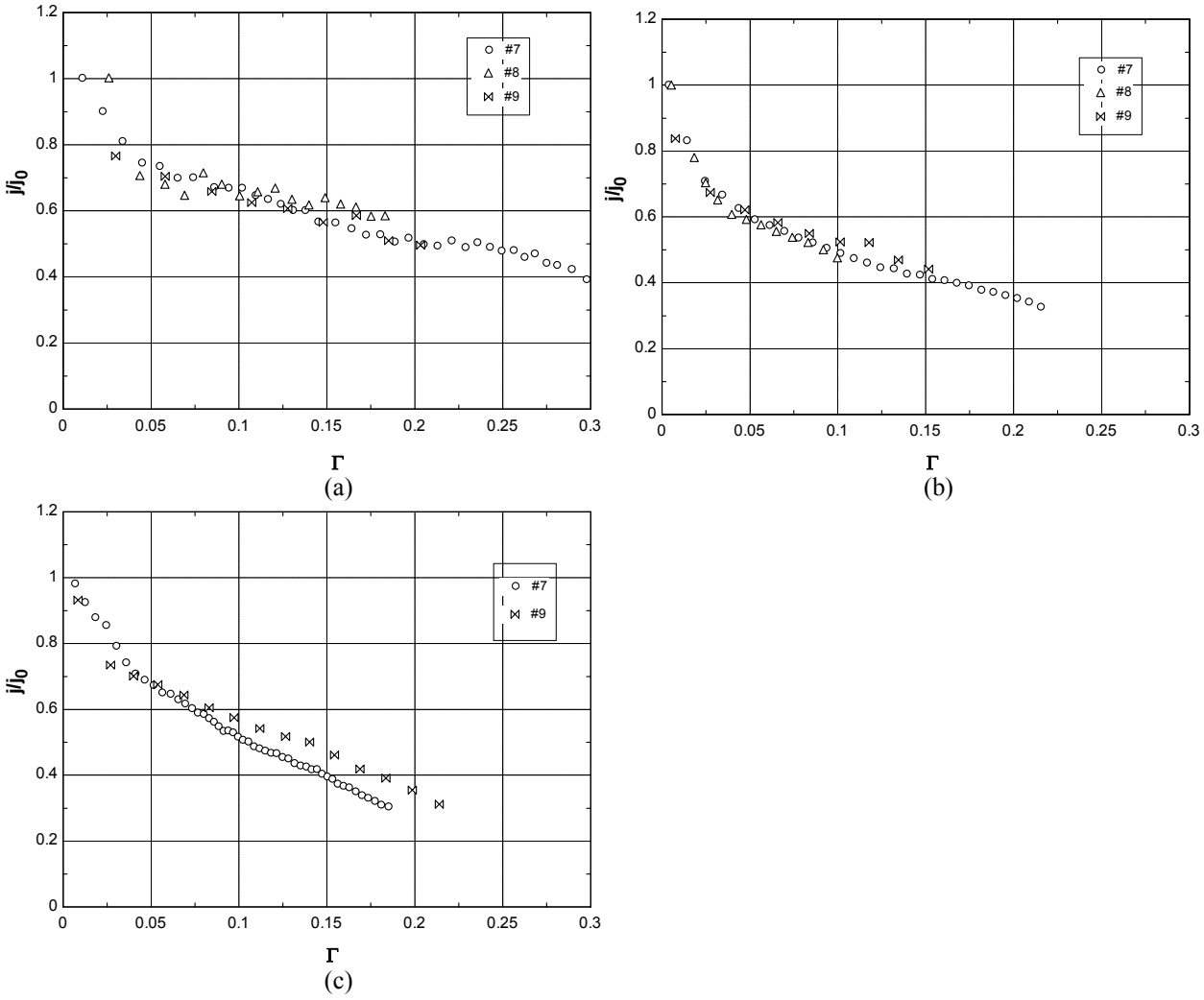

Figure 4.14 *j* factors for different environmental conditions: (a) Condition B; (b) Condition C; (c) Condition D.

To study the effect of decreasing air mass flow rate, some tests were conducted at constant air mass flow rate. Figure 4.15 compares the *j* factors under constant blower speed (i.e. decreasing air mass flow rate) and constant air mass flow rate for specimen #7 as an example. The initial air face velocities were the same 2 m/s. The trends of j/j_0 with the nondimensional frost thickness Γ are the same no matter whether the air mass flow rate was decreasing or not.

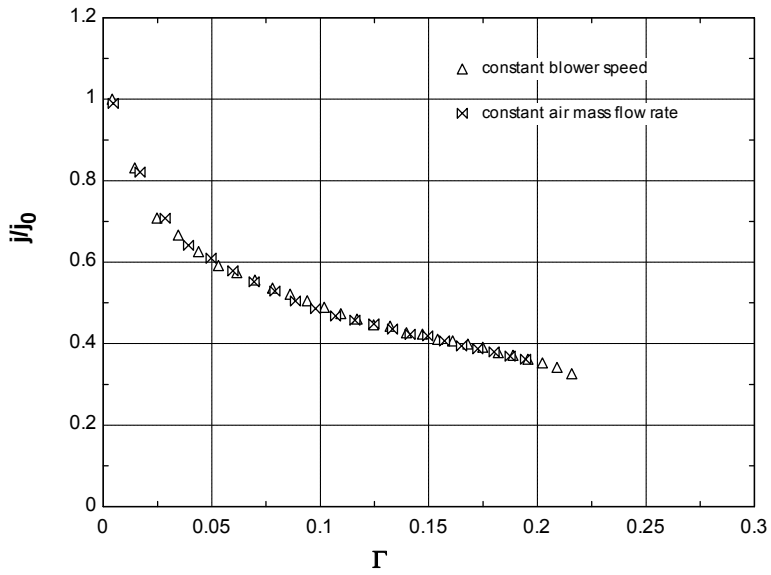

Figure 4.15 A comparison of constant blower speed and constant air mass flow rate.

4.4 Conclusions

The thermal-hydraulic behavior of folded-louvered-fin, microchannel heat exchangers was explored under conditions of air-side frosting, defrosting, and refrosting. The heat transfer and pressure drop data for nine different fin geometries were presented, and a decrease in the overall heat transfer coefficient and increase in the pressure drop was observed with the accumulation of frost. A reduction in air-side flow rate and bridging of louver gaps by frost significantly reduced the air-side heat transfer coefficient. For heat exchangers with a large fin depth and/or a large fin pitch, the average *UA* per unit volume is much lower. Correlations were developed for thermal performance prediction, and because they are cast in terms of frosted performance divided by dry-surface performance, these correlations might be useful for other louvered-fin heat exchangers.

The refrosting behavior became periodic after the third or fourth cycle. Due to the fin geometry, the corner formed by two adjacent fins tended to hold droplets during a defrost. The droplets froze in subsequent refrosting cycles with significant effects on pressure drop and heat transfer. Although the cyclic data were limited to two coils, the shallow coil was more susceptible to these droplets and frost re-distribution. This sensitivity might be related to disturbance of the developing boundary layer. Unfortunately, it is impossible to isolate fin geometry and flow-depth effects from the data obtained in this limited study.

Chapter 5. A Model for Predicting the Thermal-Hydraulic Performance of Louvered-Fin, Flat-Tube Heat Exchangers under Frosting Conditions

Nomenclature

A	area (m^2)
c_p	specific heat (J kg^{-1} $^oC^{-1}$)
D	hydraulic diameter (m)
ΔP_{HX}	pressure drop across heat exchanger (Pa)
ΔT_{lm}	log-mean temperature difference (^oC)
F	cross-flow correction factor (-)
f	friction factor (-)
g_m	mass transfer conductance (kg m^{-2} s^{-1})
H_f	fin height (m)
h	convective heat transfer coefficient ($Wm^{-2}{}^oC^{-1}$)
j	Colburn factor (-)
k	thermal conductivity ($Wm^{-1}{}^oC^{-1}$)
Le	Lewis number (Pr/Sc) (-)
L_l	louver length (m)
L_p	louver pitch (m)
m	mass (kg)
$\dot{m}$	mass flow/deposition rate (kg/s)
Pr	Prandtl number (-)
q	heat transfer rate (W)
Re	Reynolds number (-)
Sc	Schmidt number (-)
T	temperature (^oC)
t	half fin thickness (m)
UA	overall heat transfer coefficient (W $^oC^{-1}$)

Greek Symbols

Γ	nondimensional frost thickness (-)
θ	louver angle ($^\circ$)
ω	humidity ratio (kg/kg)

Subscripts

0	initial
a	moist air (i.e., dry air plus water vapor)
f	frost
fi	fin
h	hot-fluid side
i	inlet
m	middle
o	outlet
r	refrigerant
s	sensible heat
w	tube wall

5.1 Introduction

Very few models to predict the transient performance of extended-surface heat exchangers under frosting conditions have been reported in the literature, and no model of folded-louvered-fin, microchannel heat exchangers under these conditions has appeared. In this chapter, a simple numerical model will be formulated to predict the transient performance of folded-louvered-fin heat exchangers. The model will utilize the correlations developed from the experimental data, and incorporate a new method for predicting the outlet humidity and a sub-model for frost properties.

5.2 Problem Description

The purpose of the model is to predict the thermal-hydraulic performance of folded-louvered-fin heat exchangers under frosting conditions. That is, given a certain operation condition and the particular geometry of a heat exchanger, the model should be able to predict the heat transfer rate and pressure drop as frost accumulates on the heat exchanger with passing time. The operating conditions to be prescribed are air inlet temperature and humidity, coolant inlet temperature, coolant mass flow rate (or coolant side convection coefficient), and air mass flow rate.

5.3 Methods

The numerical model consists of a temporal discretization, marching the heat exchanger along the frosting process, assuming quasi-steady conditions prevail at each time step. At the very first time step, the air-side surface is dry, and the initial *j* factor is predicted using the correlation of Chang and Wang (1997), i.e. Equation (4.21). Then, the air-side convection coefficient is calculated using

$$h_h = j \cdot \frac{\mathrm{Re}\,\mathrm{Pr}^{1/3}\, k_h}{D_h}. \tag{5.1}$$

In order to determine the outlet properties of the air and the coolant, the model first guesses an outlet air temperature, $T_{a,o}$ (normally 3-4°C below the inlet temperature). Next, the model calculates the air outlet humidity ratio, ω_o, using

$$\omega_o = \left[\varpi_i - \frac{\left(g_m / \dot{m}_a\right)K^{''}}{K + \left(g_m / \dot{m}_a\right)} - K^{'''}\right]\exp\left(-\frac{g_m}{\dot{m}_a}A_{h,f}\right) + \frac{\left(g_m / \dot{m}_a\right)K^{''}}{K + \left(g_m / \dot{m}_a\right)}\exp\left(KA_{h,f}\right) + K^{'''}. \tag{5.2}$$

Equation (5.2) is based on the governing equations for heat and mass transfer rates and conservation of energy on both sides of the heat exchanger, as shown in Appendix D. In the equation, constants *K*, *K''*, and *K'''* are calculated using Equations (D.21), (D.27), and (D.28); and the value of mass transfer coefficient, g_m, is related to the convective heat transfer coefficients, h_h, through the Lewis analogy, i.e., $g_m = h_h/(c_p Le^{-2/3})$, where *Le* is Lewis number (*Pr*/*Sc*). For now, the airside surface is assumed to be fully frosted (i.e. $A_{h,f}=A_h$). Note that for the first time step (starting from frostless surface), instead of using Equation (D.14), the constant *M* should be calculated using:

$$M = \frac{1}{\cosh\left(\lambda H_f / 2\right)}, \text{ with} \tag{5.3a}$$

$$\lambda = \sqrt{\frac{h_h\left(q_a / q_{a,s}\right)}{k_{fi}t}}. \tag{5.3b}$$

Once ω_o is obtained, the frost deposition rate is calculated using

$$\dot{m}_f = \dot{m}_a\left(\varpi_i - \varpi_o\right). \tag{5.4}$$

Then, the latent and sensible heat transfer rates are calculated using Equation (4.2), and the outlet coolant temperature is determined using Equation (4.1). Next, the overall heat transfer coefficient *UA* is calculated using Equation (4.4) (with the fin efficiency and surface efficiency calculated using Equations 3.30-3.32), and the sensible heat transfer rate is updated using

$$q_{a,s} = F \cdot UA \cdot \Delta T_{lm}. \tag{5.5}$$

Finally, the updated value of $T_{a,o}$ is calculated using

$$T_{a,o} = T_{a,i} - \frac{q_{a,s}}{\dot{m}_a c_{p_a}}. \tag{5.6}$$

Iteration continues until convergence, and with the converged solution the thickness of deposited frost is determined using Equations (4.16) and (4.17), as described in Chapter 4.

For each subsequent time step, the model first determines the *j* factor using Equation (4.23) or (4.26) according to the given environmental conditions. Calculations similar to those described above are then undertaken, except that the fin efficiency and surface efficiency are calculated using Equations (4.6)-(4.10). The procedure continues step by step, until a preselected criterion is met, such as the overall heat transfer coefficient *UA* decreases to a certain prescribed percentage of the initial level.

In order to predict the hydraulic performance, Figure 4.6(c) is used for the *f* factor and Equation (4.14) allows direct calculation of the pressure drop across the heat exchanger. This method, however, is not recommended for $I^*>0.1$ where the uncertainty in *f*-factor measurement exceeds ±0.5. Because of uncertainties in the *f* factor, predictions of pressure drop are much less accurate than predictions of heat transfer and frost accumulation.

The above procedure is complete for the case of constant air mass flow rate. As for the case of a heat exchanger operating in accordance with a typical fan-duct arrangement, an extra equation for calculating the air mass flow rate is needed, which will require a model representing the system fan curve, such as the air mass flow rate that the fan can provide as a function of the pressure drop across the heat exchanger.

The other ancillary procedures (such as the one for calculating the air properties) are detailed in Appendix C.

5.4 Results and Discussion

The numerical model was first applied to specimens #2 and #6 to predict their performances under the operation conditions described in Section 4.2.1. In order to evaluate the model predictions of the thermal performance while isolating the effect of changing air mass flow rate, the Reynolds number as a function of time (in min) was obtained from a curve fit to the test data, namely:

$$\mathrm{Re} = 322+1.21\cdot \mathrm{time}\text{-}0.0127\cdot \mathrm{time}^2 \text{, for specimen \#2; and} \tag{5.8}$$

$$\mathrm{Re} = 197\text{-}0.91\cdot \mathrm{time}\text{-}0.0188\cdot \mathrm{time}^2 \text{, for specimen \#6.} \tag{5.9}$$

Model predictions are compared to test data in Figures 5.1 and 5.2 where heat transfer rate and frost accumulation are calculated assuming that the airside surface was totally frosted for specimen #2 and #6. Note that Equations (4.23a) and (4.23b) are used for specimens #2 and #6, respectively.

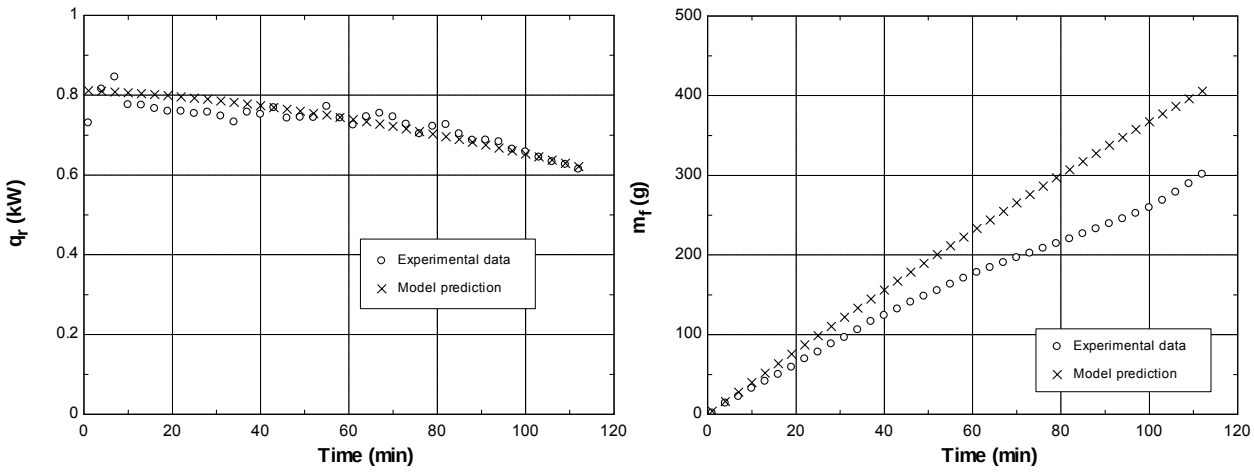

(a) (b)

Figure 5.1 A comparison of the model prediction to experimental data for specimen #2 ($A_{h,f}$= A_h): (a) heat transfer rate; (b) frost accumulation.

For specimen #6, the model provides good predictions of the heat transfer rate, and slightly over predicts the frost accumulation. However, for specimen #2, the model over predicts the frost accumulation by 33%, while predicting heat transfer rates to within 10% of the measurements. Specimen #2 has a significantly larger heat transfer area and coolant flow length than does #6, and thus specimen #2 has a higher coolant temperature rise and higher surface temperature near the coolant exit; thus, it may be expected that specimen #2 was not operating under fully frosted conditions. Therefore, it is likely that assuming $A_{h,f}$=A_h for specimen #2 causes an over prediction of frost accumulation.

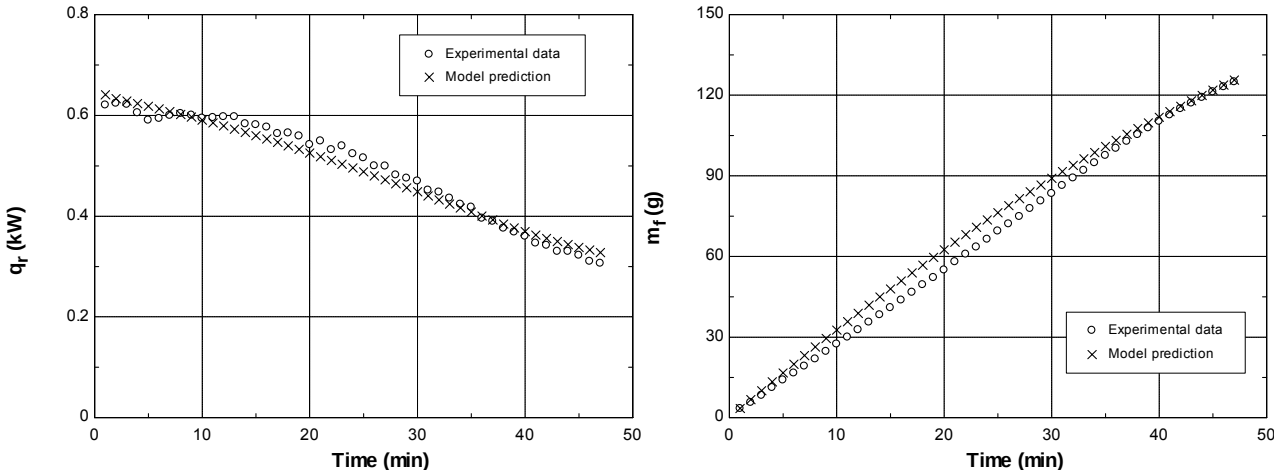

(a) (b)

Figure 5.2 A comparison of the model prediction to experimental data for specimen #6 ($A_{h,f}$= A_h): (a) heat transfer rate; (b) frost accumulation.

A simple method for predicting the frosted surface area was developed from the governing equations (see Appendix E), but the method fails to provide a reliable prediction of the frosted area for the test cases in this study. The method assumes counter-flow conditions and takes the position where the humidity ratio of the air equals the

humidity ratio corresponding to saturation at the surface temperature as the location where frost accumulation ceases. In this way, $A_{h,f}$ is established as a function of the measured ω_o. Unfortunately, less than ±10% uncertainty in ω_o will result in a ±1 ˚C uncertainty in $T_{a,m}$, which is the air temperature at the demarking location. Since the total air temperature difference between the inlet and outlet is typically 2-4 ˚C in this study, the approach described above can result in an uncertainty in the predicted $A_{h,f}$ as large as ±50%. Such sensitivity also makes convergence of the time-marching calculations problematic. Therefore, this analytical method was not adopted. Although it is not suitable for conditions with small air temperature drops, it might be useful for other conditions.

Because, as described above, an analytical approach is unlikely to give a reliable prediction of the frosted area, a semi-empirical method is adopted. Using experimental measurements of the outlet humidity ratio for specimens #2 and #6, along with the values of heat transfer coefficient already determined, a direct calculation of $A_{h,f}$ is possible for each heat exchanger using Equation (5.2). The uncertainty in the measured outlet humidity ratio is ± 4%, and this results in ±20% uncertainty in the calculated $A_{h,f}$. The calculated values (averaged over time) are $A_{h,f}/A_h$ = 75% for specimen #2 which has a larger face area, and 100% for specimen #6, which means the airside surface was fully frosted. Adopting these average values, Equation (5.2) is then used to calculate the outlet humidity ratio for specimen #2 and #6. The calculation is compared to the test data in Figure 5.3, where $A_{h,f}$ denotes the area of the frosted surface. The comparison supports the conjecture that specimen #2 was not fully frosted. Moreover, it suggests that changes in area partitioning (the fraction of area participating in mass transfer) with time are not significant for the duration of these experiments.

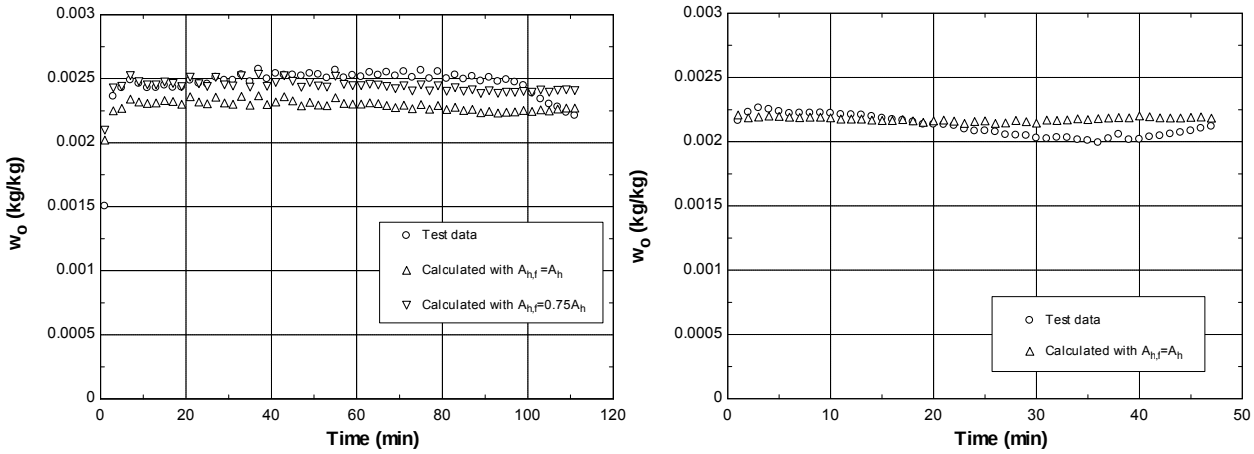

Figure 5.3 A comparison of the outlet humidity ratio calculated using Equation (5.2) to the test data: (a) specimen #2; (b) specimen #6.

Extending this approach, the model was then used to predict the performance of specimen #2 with 75% of the total airside surface assumed to be frosted, under the same operating conditions used earlier. As shown in Figure 5.4, both the heat transfer rate and frost accumulation are predicted well.

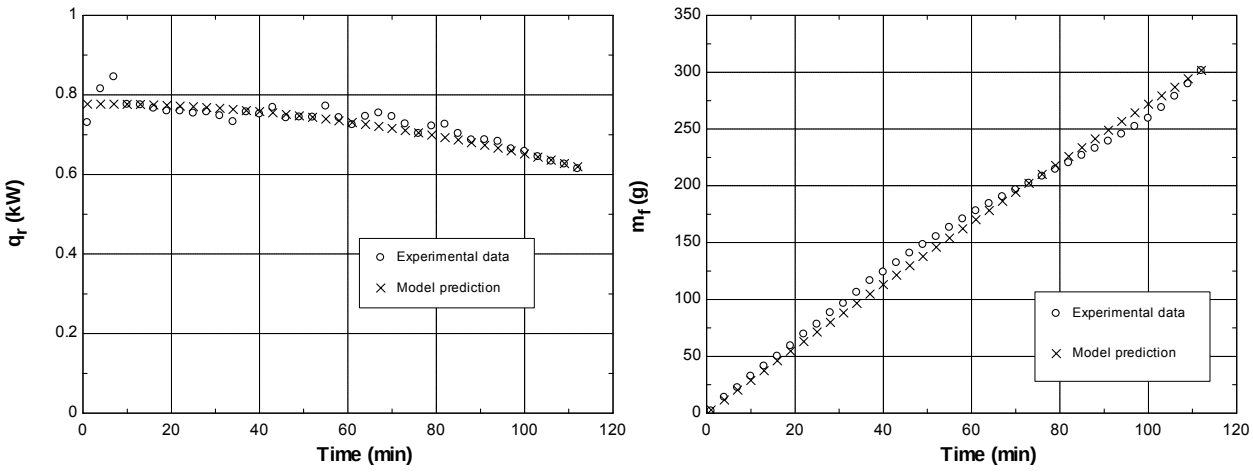

(a) (b)

Figure 5.4 A comparison of the model predictions to experiments for specimen #2 ($A_{h,f}$=0.75 A_h): (a) heat transfer rate; (b) frost accumulation.

Heat exchangers with relatively large face areas are more prone to partial air-side frosting, because the coolant flow length is relatively large, creating a potential for large coolant temperature rises. The degree of the frosting will depend on both the geometry of the heat exchanger and the operating conditions. Due to the limitations of the current data and heat exchanger samples, no attempt was made to develop a generalized empirical relationship. Applying the model to cases of partial frosting, assuming the heat exchanger to be fully frosted, will result in significant over prediction of frost accumulation, but the heat transfer predictions remain fairly accurate. For some cases in this study, frost accumulation was over predicted by 100%, but predictions of heat transfer remained within 20% of the measurements. Although *a priori* knowledge of partial frosting is difficult, whenever the modeled outlet humidity ratio approaches the humidity ratio corresponding to saturation at the coolant outlet temperature, the model predictions should be regarded with caution.

Next, the model is evaluated for other operation conditions. Taking condition D as listed in Table 4.3 as an example, model predictions are compared to the experimental data for specimen #9 in Fig 5.5. Correlation (4.26c) is used in this case. Figure 5.6 shows a comparison for specimen #9 under condition C, but with constant air mass flow rate. Since as shown in Section 4.3.3, the trends of j/j_0 with the nondimensional frost thickness Γ are the same no matter whether the air mass flow rate was decreasing or not, correlation (4.26b) is used for this case. Good agreement is achieved for both cases.

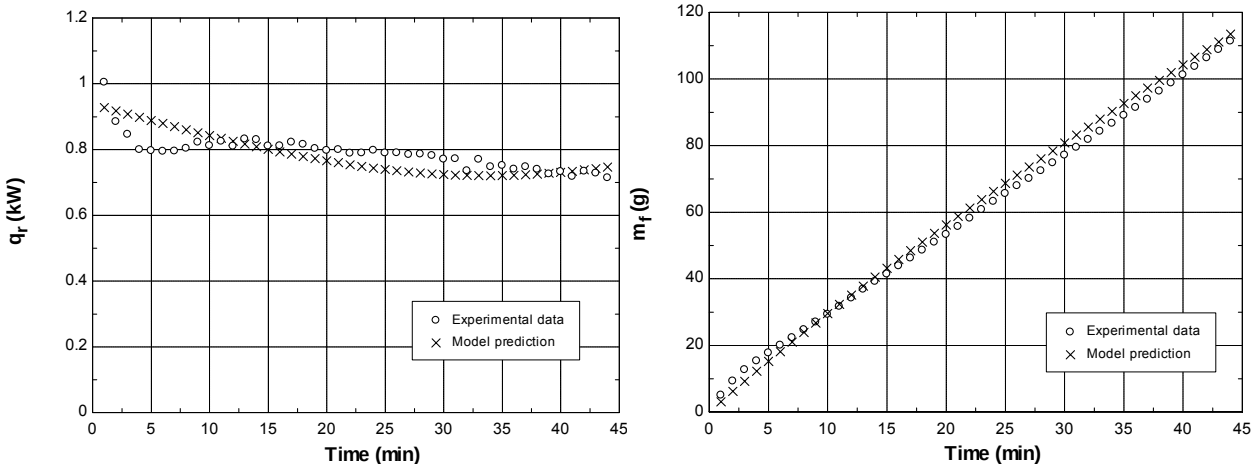

(a) (b)

Figure 5.5 A comparison of the model predictions to experiments for specimen #9 under condition D ($A_{h,f}$=A_h): (a) heat transfer rate; (b) frost accumulation.

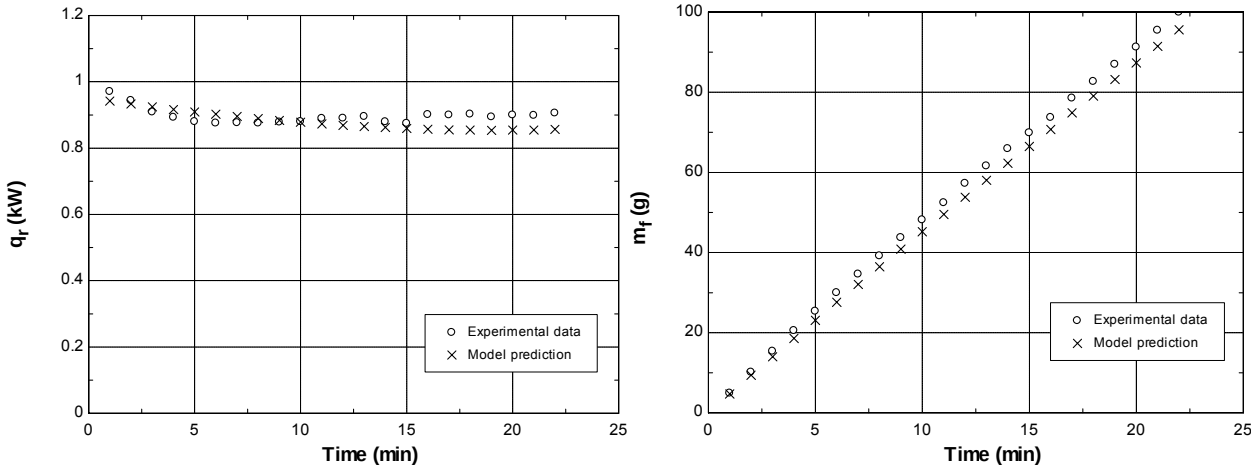

(a) (b)

Figure 5.6 A comparison of the model predictions to experiments for specimen #9 under condition C and constant air mass flow rate ($A_{h,f}$=A_h): (a) heat transfer rate; (b) frost accumulation.

The model does an excellent job in predicting the transient thermal performance; however, predictions of hydraulic performance are more difficult. Success depends on the accuracy of the *f*-factor correlation, and as described earlier, these data usually have large uncertainties for heavily frosted heat exchangers. Example predictions of the pressure drop across specimen #6 for the first 20 minutes are shown in Figure 5.7. The initial *f* factor is predicted using the correlation developed by Davenport (1983):

$$f_0 = 5.47\,\mathrm{Re}_{Lp}^{-0.72}\left(L_p \sin\theta\right)^{0.37}\left(H_f\right)^{0.23}\left(L_p\right)^{0.2}\left(\frac{L_l}{H_f}\right)^{0.89}, \quad 70<\mathrm{Re}<1000. \tag{5.9}$$

Due to the dramatically increasing uncertainty in *f* factor introduced by the uncertainty in frost thickness, the pressure drop is very difficult to predict with satisfactory accuracy, as can be seen from Figure 5.7. The method for predicting hydraulic performance needs improvement either by increasing the accuracy in frost thickness

measurement (which will be very challenging due to the nature of the frost structure), or by seeking a new generalization method (other than the *f* factor).

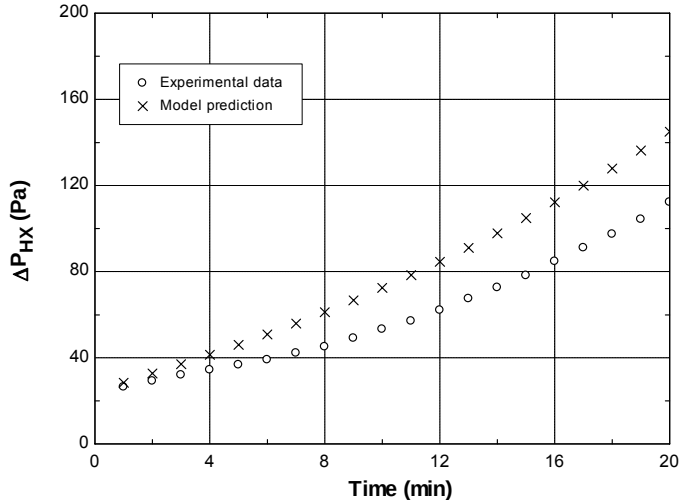

Figure 5.7 An example comparison of the model predictions to pressure drop data for specimen #6.

5.5 Conclusions

A model is developed to predict the transient performance of folded-louvered-fin, flat-tube heat exchangers. The model utilizes the correlations developed from the experimental data and incorporates a sub-model for frost properties. The true generality of this model can be validated when further data become available. A method for predicting the outlet humidity is developed based on the governing equations for heat and mass transfer rates and conservation of energy on both sides of the heat exchanger. The method is validated with experimental data, and demonstrates that partial frosting occurs for heat exchangers with large face areas in this study; these heat exchangers, due to larger heat transfer areas and longer coolant flow lengths, operate with larger coolant temperature changes than the other specimens.

Further validation of the model is provided by comparing the predicted thermal-hydraulic performance of several heat exchangers to experimental data, obtained with different heat exchanger geometries and operating conditions. For cases where the heat transfer surface is fully frosted, the results show the model has excellent predictive performance when it comes to heat transfer and frost accumulation; however, predictions of pressure drop are not very accurate, largely because uncertainties in the experimentally determined friction factor are inherently large for heavily frosted conditions. It is also possible that the frost property correlations obtained from the literature (frost density in particular) cause this problem.

Although caution should be exercised in applying the model to situations where partial frosting occurs, the model provides good predictions of heat transfer and frost accumulation under fully frosted conditions, and reasonable heat transfer predictions under partially frosted conditions. Improvements in predicting frosted/dry area partitioning and pressure drop under heavily frosted conditions could make the model more broadly applicable. The model can be used to evaluate geometry effects on the frost-surface performance of the louvered-fin, flat-tube heat exchangers, and can be easily generalized to other applications with simultaneous heat and mass transfer.

Chapter 6. Conclusions and Recommendations

6.1 Introduction

Motivated by applications in heat pumping and refrigeration, and by the emerging importance of folded-louvered-fin microchannel heat exchangers, a study of the thermal-hydraulic performance of these heat exchangers under frosted-surface conditions has been completed. Not only does the literature reflect a dearth of relevant empirical data, a careful study of the extant work shows that there are gaps and inconsistencies in current data reduction and interpretation schemes that vitiate the generality of existing correlations for frosted heat exchanger performance. The work reported in this thesis has made significant progress in resolving those inconsistencies, in obtaining valuable data, and in modeling and understanding these data. In that sense, this work has advanced our understanding of frosted-surface heat exchanger performance in general, the folded-fin microchannel heat exchanger in particular, and it has provided a framework for consistently interpreting experimental data. In addition, it provides a useful simulation method to model the transient performance of heat exchangers that can be used for design and generalized for other geometries.

6.2 Summary of Results

The temperature distribution within a two-dimensional composite fin was analyzed. A parametric analysis showed that when $B_i > 0.05$ and $R < 0.1$, the fin problem can be approximated as a two-dimensional slab on a one-dimensional fin. Under this approximation, an exact solution to the heat diffusion equation was obtained by an eigenfunction expansion, an approach that results in an unusual and interesting sense of orthogonality. In comparison to prior, fully two-dimensional solutions, this new solution has the advantages of rapid convergence and relatively simple calculation. Moreover, conditions are identified for which a one-term approximation to the solution is sufficient, and it was found that frost on a metallic fin often falls into this range. The analytical solution and the one-term approximation have broad applicability in addition to their use for calculating fin efficiency for frost-coated fins.

Valid *HA*-LMED and *UA*-LMTD methods for wet- and frosted-surface heat transfer were formulated. Fin-efficiency expressions for flat-tube heat exchangers with constant-area fins are provided for both methods, with improved expressions for frosted-surface conditions that consider two-dimensional conduction of heat in the frost layer. The new *UA*-LMTD method was shown to provide the best results for dry, partially wet/frosted, and fully wet/frosted conditions. The *HA*-LMED method is only applicable to fully wet/frosting conditions, unless area partitioning is used. For all the conditions considered, the *UA*-LMTD method provided the value of the air-side convective heat transfer coefficient to within 3% and was found to be more accurate than the method of *HA*-LMED. It is recommended that frosted-surface heat transfer data be interpreted using the new *UA*-LMTD approach, especially when partial frosting conditions might occur.

The thermal-hydraulic behavior of the folded-louvered-fin, microchannel heat exchangers was explored under conditions of air-side frosting, defrosting, and refrosting. Heat transfer and pressure drop data for nine different fin geometries were presented, and a decrease in the overall heat transfer coefficient and increase in the pressure drop was observed with the accumulation of frost. The reduction in air-side flow rate and bridging of louver gaps by frost play significant roles in the heat transfer behavior. For heat exchangers with a large fin depth and/or a

large fin pitch, the average *UA* per unit volume is much lower than for more compact designs. General correlations were developed for thermal performance prediction.

It was found that the refrosting behavior became periodic after the third or fourth cycle. Due to the fin geometry, the corner formed by two adjacent fins tended to retain droplets during a defrost. The droplets froze in subsequent refrosting cycles with significant effects on pressure drop and heat transfer. Although the cyclic data are limited to two coils, the shallow coil was more susceptible to these droplets and frost re-distribution. This sensitivity might be related to disturbance of the developing boundary layers. Unfortunately, it is impossible to isolate fin geometry and flow-depth effects from the data obtained in this limited study.

A model was developed to predict the transient performance of folded-louvered-fin, flat-tube heat exchangers under frosting conditions. The model utilizes the correlations developed from the experimental data and incorporates a sub-model for frost properties. A method for predicting the outlet humidity was developed based on the governing equations for heat and mass transfer rates and conservation of energy on both sides of the heat exchanger. The model was validated with experimental data, and it was found that some heat exchangers under some test conditions manifested partial frosting behavior. Pressure-drop predictions were more challenging than heat transfer and frost accumulation predictions, and the model was less successful, probably due to uncertainties in the friction factor data.

6.3 Recommendations for Future Work

The louvered-fin, flat-tube heat exchangers used in this study do not span large differences in fin pitch or louver design in a way that allows for careful isolation of their effects on frosting and defrosting performance; future work should consider a broader range of geometry. Significantly extending the geometric space could result in correlations that are in a more generalized form to cover a wider range of geometry variations, and help in understanding the differences in flow-depth effects observed in this work. Moreover, the effects of water retention and refreezing on cyclical frost growth could be elucidated through further study with a wider geometrical range. With defrosting and refrosting data for more fin geometries available, a correlation for the multipliers of first-frosting performance to cyclic-frosting performance can be generated, and used to predict the cyclic performance based on the model for the first-cycle performance presented in Chapter 5.

It would also be interesting to study the effects of fin wettability on frost growth, defrost and refrost for these heat exchangers. Because wettability has a direct effect on water retention, its impact on defrost and refrost could be profound. Unfortunately, almost nothing is currently available in the literature to account for such effects.

Finally, an improved ability to predict the hydraulic performance of a frosted heat exchanger could result from further model development. One possible solution is to increase the accuracy in frost thickness measurement. However, due to the nature of the frost structure (fluffy and irregular), this task will be very challenging. Another solution could be seeking new generalization method other than the *f* factor, such as a ratio of the heat transfer decrease rate to the pressure drop increase rate. Since as manifested by the data, a higher decrease rate in heat transfer rate was almost always associated with a higher increase rate in pressure drop, it is possible that a relationship between pressure drop and heat transfer can be used to forecast the pressure drop based on the prediction of heat transfer rate.

Bibliography

Abdel-Wahed, R. M., Hifni, M. A., Sherif, S. A., 1982, Heat and mass transfer from a laminar humid air stream to a plate at subfreezing temperature, *International Journal of Refrigeration*, vol. 7, no. 1, pp. 49-55.

ASHRAE Standard 33-2000 - Methods of Testing Forced Circulation Air Cooling and Air Heating Coils (ANSI approved).

Aviles-Ramos, C., Haji-Sheikh, A., Beck, J.V., 1998, Exact solution of heat conduction in composite materials and application to inverse problems, *Journal of Heat Transfer*, vol. 120, pp. 592-599.

Barker, J. J., 1958, The efficiency of composite fins, *Nuclear Science and Engineering*, vol. 3, pp. 300-312.

Barrow, H., 1985, A note on frosting of heat pump evaporator surfaces, *Journal of Heat Recovery Systems*, vol. 5, no. 3, pp. 195-201.

Bowman, R. A., Mueller, A. C., Nagle, W. M., 1940, Mean temperature difference in design, *Transactions ASME*, vol. 62, no. 4, pp. 283-294.

Brian, P. L. T., Reid, R. C., Shah, Y. T., 1970, Frost deposition on cold surfaces, *Ind. Eng. Chem. Fundam.*, vol. 9, no. 3, pp. 375-380.

Carlson, D. M., Hrnjak, P. S., Bullard, C. W., 2001, Deposition, Distribution, and Effects of Frost on a Multi-Row Heat Exchanger Performance, ACRC TR-183, University of Illinois, Urbana-Champaign.

Chang, Y.-J., Wang, C.-C., 1997, A generalized heat transfer correlation for louver fin geometry, *International Journal of Heat and Mass Transfer*, vol. 40, no. 3, pp. 533-544.

Chen, H., Besant, R. W., Tao, Y.-X., 1999, Frost characteristics and heat transfer on a flat plate under freezer operating conditions: Part II, Numerical modeling and comparison with data, *ASHRAE Transactions*, vol. 105, pt. 2, pp. 252-259.

Chen, H., Thomas, L., Besant, R. W., 1999, Measurement of frost characteristics on heat exchanger fins, *ASHRAE Transactions*, vol. 105, pt. 2, pp. 294-302.

Chen, H., Thomas, L., Besant, R. W., 2000a, Modeling frost characteristics on heat exchanger fins, Part I: Numerical modeling, *ASHRAE Transactions*, vol. 106, pt. 2, pp. 358-367.

Chen, H., Thomas, L., Besant, R. W., 2000b, Modeling frost characteristics on heat exchanger fins, Part II: Model validation and limitations, *ASHRAE Transactions*, vol. 106, pt. 2, pp. 368-376.

Chen, H., Thomas, L., Besant, R. W., 2003, Fan supplied heat exchanger fin performance under frosting conditions, *International Journal of Refrigeration*, vol. 26, pp. 140-149.

Chen, M. M., Rohsenow, W., 1964, Heat, mass, and momentum transfer inside frosted tubes – experiment and theory, *Journal of Heat Transfer*, vol. 86, pp. 334-340.

Cheng, C.-H., Cheng, Y.-C., 2001, Predictions of frost growth on a cold plate in atmospheric air, *International Communications in Heat and Mass Transfer*, vol. 28, no. 7, pp. 953-962.

Cheng, C.-H., Shiu, C.-C., 2002, Frost formation and frost crystal growth on a cold plate in atmospheric air flow, *International Journal of Heat and Mass Transfer*, vol. 45, pp. 4289-4303.

Cheng, C.-H., Shiu, C.-C., 2003, Oscillation effects on frost formation and liquid droplet solidification on a cold plate in atmospheric air flow, *International Journal of Refrigeration*, vol. 26, pp. 69-78.

Cheng, C.-H., Wu, K.-H., 2003, Observations of early-stage frost formation on a cold plate in atmospheric air flow, *Journal of Heat Transfer*, vol. 125, pp. 95-102.

Chu, H., Weng, C., Chen, C., 1983, Transient response of a composite straight fin, *Journal of Heat Transfer*, vol. 105, pp. 307-311.

Chung, P. M., Algren, A. B., 1958, Frost formation and heat transfer on a cylinder surface in humid air cross flow - part I: Experimental study, *Heating, Piping & Air Conditioning*, vol. 30, no. 9, pp. 171-178.

Chung, P. M., Algren, A. B., 1958, Frost formation and heat transfer on a cylinder surface in humid air cross flow - part II: Theoretical study and conclusions, *Heating, Piping & Air Conditioning*, vol. 30, no. 10, pp. 115-122.

Davenport, C. J., 1983, Correlation for heat transfer and flow friction characteristics of louvered fin, AIChE Symp. Ser., vol. 79, pp. 19-27.

Dietenberger, M. A., 1983, Generalized correlation of the water frost thermal conductivity, *International Journal of Heat and Mass Transfer*, vol. 26, no. 4, pp. 607-619.

Dyer, J. M., Storey, B. D., Hoke, J. L., An experimental investigation of the effect of hydrophobicity on the rate of frost growth in laminar channel flows, *ASHRAE Transactions*, vol. 106, pt. 1, pp. 143-151.

Emery, A. F., Siegel, B. L., 1990, Experimental measurement of the effects of frost formation on heat exchanger performance, Heat and Mass Transfer in Frost and Ice, Packed Beds, and Environmental Discharges, *Proc. of AIAA/ASME Thermophysics and Heat Transfer Conference* (Arimilli *et al.* ed.), *ASME HTD*, vol. 139, pp. 1-7.

Feijoo, L., Davis, H. T., Ramkrishna, D., 1979, Heat transfer in composite solids with heat generation, *Journal of Heat Transfer*, vol. 101, pp. 137-143.

Fisk, W. J., Chant, R. E., Archer, K. M., Hekmat, D., Offermann, F. J., Pedersen, B. S., 1985a, Onset of freezing in residential air-to-air heat exchangers, *ASHRAE Transactions*, vol. 91, pt. 1B, pp. 145-158.

Fisk, W. J., Chant, R. E., Archer, K. M., 1985b, Performance of residential air-to-air heat exchangers during operation with freezing and periodic defrosts, *ASHRAE Transactions*, vol. 91, pt. 1B, pp. 159-172.

Friedman, B., 1956, Principles and Techniques of Applied Mathematics, John Wiley and Sons, New York, pp. 205-207.

Gatchilov, T. S., Ivanova, V. S., 1979, Characteristics of extended surface air coolers during operation under frosting conditions, *International Journal of Refrigeration*, vol. 2, no. 4, pp. 233-236.

Gates, R. R., Sepsy, C. F., Huffman, G. D., 1967, Heat transfer and pressure loss in extended surface heat exchangers operating under frosting conditions - part I: Literature survey, test apparatus and preliminary results, *ASHRAE Transactions*, vol. 73, pt. 2, pp. 1.2.1-1.2.13.

Hayashi, Y., Aoki, A., Adachi, S., 1977, Study of frost properties correlating with frost formation types, *Journal of Heat Transfer*, vol. 99, pp. 239–245.

Hayashi, Y., Aoki, A., Yuhara, H., 1977, Study of frost formation based on a theoretical model of the frost layer, *Heat Transfer- Japanese Research*, vol. 6, no. 3, pp. 79-94.

Hoke, J. L., Georgiadis, J. G., Jacobi, A. M., 2000, "The Interaction Between the Substrate and Frost Layer Through Condensate Distribution", ACRC TR-177, Air Conditioning and Refrigeration Center, University of Illinois at Urbana-Champaign.

Huang, C.-H., 2002, An inverse geometry problem in estimation frost growth on an evaporating tube, *Heat and Mass Transfer*, vol. 38, pp. 615-623.

Huang, S. C., Chang, Y. P., 1980, Heat conduction in unsteady, periodic, and steady states in laminated composites, *Journal of Heat Transfer*, vol. 102, pp. 742-748.

Huffman, G. D., Sepsy, C. F., 1967, Heat transfer and pressure loss in extended surface heat exchangers operating under frosting conditions - part II: Data analysis and correlation, *ASHRAE Transactions*, vol. 73, pt. 2, pp. 1.3.1-1.3.16.

Hwang C. L., Fan L. T., 1964, Finite difference analysis of forced-convection heat transfer in entrance region of a flat rectangular duct, *Applied Science Research*, Sect A, vol. 13, pp. 401-422.

Ismail, K. A. R., Salinas, C. S., 1999, Modeling of frost formation over parallel cold plates, *International Journal of Refrigeration*, vol. 22, pp. 425-441.

Ismail, K. A. R., Salinas, C. S., Gonçalves, M. M., 1997, Frost growth around a cylinder in a wet air stream, *International Journal of Refrigeration*, vol. 20, no. 2, pp. 106-119.

Itoh, M., Kogure, H., Yoshinaga, S., Hoshino, R., Wakabayashi, N., Kudoh, M., Kusumoto, H., 1996, Study on parallel-flow-type heat exchangers for residential heat pump systems, *Proc. of the 1996 JAR Annual Conference*, pp. 73-76. (in Japanese)

Jhee, S., Lee, K.-S., Kim, W.-S., 2002, Effect of surface treatments on the frosting/defrosting behavior of a fin-tube heat exchanger, *International Journal of Refrigeration*, vol. 25, pp. 1047-1053.

Jones, B. W., Parker, J. D., 1975, Frost formation with varying environmental parameters, *Journal of Heat Transfer*, vol. 97, pp. 255-259.

Kays, W. M., London, A. L., 1964, Compact Heat Exchangers, second edition. McGraw-Hill, Inc.

Kim, J., Groll, E. A., 2002, Performance comparisons of a unitary split system using microchannel and fin-tube outdoor coils, Part II: Heating test, *Proceedings of the 2002 International Refrigeration and Air Conditioning Conference at Purdue*, vol. I, pp. 249-256.

Kondepudi, S. N., O'Neal, D. L., 1987, The effects of frost growth on extended surface heat exchanger performance – a review, *ASHRAE Transactions*, vol. 93, pt. 2, pp. 258-274.

Kondepudi, S. N., O'Neal, D. L., 1989, Effect of frost growth on the performance of louvered finned tube heat exchangers, *International Journal of Refrigeration*, vol. 12, pp. 151–158.

Kondepudi, S. N., O'Neal, D. L., 1993, A simplified model of pin fin heat exchangers under frosting conditions, *ASHRAE Transactions*, vol. 99, pt. 1, pp. 754-761.

Kwon, J.-T., Lim, H. J., Kwon, Y.-C., Koyama, S., Kim, D.-H., Kondou, C., 2006, An experimental study on frosting of laminar air flow on a cold surface with local cooling, *International Journal of Refrigeration*, vol. 29, pp. 754–760.

Lee, K.-S., Jhee, S., Yang, D.-K., 2003, Prediction of the frost formation on a cold flat surface, *International Journal of Heat and Mass Transfer*, vol. 49, pp. 3789-3796.

Lee, K.-S., Kim, W.-S., Lee, T.-H., 1997, A one-dimensional model for frost formation on a cold flat surface, *International Journal of Heat and Mass Transfer*, vol. 40, no. 18, pp. 4359–4365.

Lee, Y. B., Ro, S. T., 2001, An experimental study of frost formation on a horizontal cylinder under cross flow, *International Journal of Refrigeration*, vol. 24, pp. 468-474.

Lee, Y. B., Ro, S. T., 2002, Frost formation on a vertical plate in simultaneously developing flow, *Experimental Thermal and Fluid Science*, vol. 26, pp. 939-945.

Le Gall, R., Grillot, J. M., Jallut C., 1997, Modeling of frost growth and densification, *International Journal of Heat and Mass Transfer*, vol. 40, no. 13, pp. 3177-3187.

Lüer, A., Beer, H., 2000, Frost deposition in a parallel plate channel under laminar flow conditions, *International Journal of Thermal Science*, vol. 39, pp. 85-89.

Mago, P. J., Sherif, S. A., 2002, Modeling the cooling process path of a dehumidifying coil under frosting conditions, *Journal of Heat Transfer*, vol. 124, pp. 1182-1191.

Mao, Y., Besant, R. W., Chen, H., 1999, Frost characteristics and heat transfer on a flat plate under freezer operating conditions: Part I, Experimentation and correlations, *ASHRAE Transactions*, vol. 105, pt. 2, pp. 231-251.

Mao, Y., Besant, R. W., Falk, J., 1993, Measurement and correlations of frost properties with laminar airflow at room temperature over a flat plate, *ASHRAE Transactions*, vol. 99, pt. 1, pp. 739-745.

Mao, Y., Besant, R. W., Rezkallah, K. S., 1992, Measurement and correlations of frost properties with airflow over a flat plate, *ASHRAE Transactions*, vol. 98, pt. 2, pp. 65-78.

Marinyuk, B. T., 1980, Heat and mass transfer under frosting conditions, *International Journal of Refrigeration*, vol. 3, no. 6, pp. 366-368.

Miller, W. A., 1987, Laboratory examination and seasonal analysis of frosting and defrosting for an air-to-air heat pump, *ASHRAE Transactions*, vol. 93, pt. 1, pp. 1474-1489.

Mokheimer, E. M. A., Antar, M. A., Farooqi, J., Zubair, S. M., 1997, Analytical and numerical solution along with PC spreadsheets modeling for a composite fin, *Heat and Mass Transfer*, vol. 32, pp. 229-238.

Na, B., Webb, R. L., 2003, A fundamental understanding of factors affecting frost nucleation, *International Journal of Heat and Mass Transfer*, vol. 46, pp. 3797-3808.

Niederer, D. H., 1976, Frosting and defrosting effects on coil heat transfer, *ASHRAE Transactions*, vol. 82, pt. 1, pp. 467-473.

Ogawa, K., Tanaka, N., Takeshita, M., 1993, Performance improvement of plate fin-and-tube heat exchangers under frosting conditions, *ASHRAE Transactions*, vol. 99, pp. 762-774.

Okoroafor, E. U., Newborough, M., 2000, Minimising frost growth on cold surfaces exposed to humid air by means of crosslinked hydrophilic polymeric coatings, *Applied Thermal Engineering*, vol. 20, pp. 737-758.

O'Neal, D. L., Bryant, J. A., Parker, B., 1997, Impact of a hydrophobic coating on the frost buildup and defrost performance of a heat pump evaporator, *New Approach Toward Low-Temperature Thermal Engineering Without Fluorocarbon Refrigerants, Proceedings of the 45th Oji International Seminar*. ed: S. Fukusako and K. Hijikata. Tomakomai city, Hokkaido Japan, pp. 181-187.

O'Neal, D. L., Tree, D. R., 1984, Measurement of frost growth and density in a parallel plate geometry, *ASHRAE Transactions*, vol. 90, pt. 2a, no. 2843, pp. 278–290.

O'Neal, D. L., Tree, D. R., 1985, Review of frost formation in simple geometries, *ASHRAE Transactions*, vol. 91, no. 2, pp. 267–281.

Östin, R., 1992, A study of heat exchanger under frosting conditions, *Heat Recovery Systems & CHP*, vol. 12, no. 2, pp. 89-103.

Östin, R., Andersson, S., 1991, Frost growth parameters in a forced air stream, *International Journal of Heat and Mass Transfer*, vol. 34, no. 4-5, pp. 1009-1017.

Östin, R., Johannesson, G., 1991, A polymeric approach to counteract frosting in air-to-air heat exchangers, *Heat Recovery Systems & CHP*, vol. 11, no. 5, pp. 415-421.

Padki, M. M., Sherif, S. A., Nelson, R. M., 1989, A simple method for modeling the frost formation phenomenon in different geometries, *ASHRAE Transactions*, vol. 95, pp. 1127–1137.

Padovan, J., 1974, Generalized Sturm-Liouville procedure for composite domain anisotropic transient heat conduction problems, *AIAA Journal*, vol. 12, no. 8, pp. 1158-1160.

Şahin, A. Z., 1994, An experimental study on the initiation and growth of frost formation on a horizontal plate, *Experimental Heat Transfer*, vol. 7, pp. 101-119.

Şahin, A. Z., 1995, An analytical study of frost nucleation and growth during the crystal growth period, *Heat and Mass Transfer*, vol. 30, pp. 321-330.

Şahin, A. Z., 2000, Effective thermal conductivity of frost during the crystal growth period, *International Journal of Heat and Mass Transfer*, vol. 43, pp. 539-553.

Sami, S. M., Duong, T., 1989, Mass and heat transfer during frost growth, *ASHRAE Transactions*, vol. 95, pt. 1, pp. 158-165.

Sanders, C., 1974, The Influence of Frost Formation and Defrosting on the Performance of Air Coolers. Ph. D. Dissertation, Technische Hogescool, Delft, Netherlands.

Schneider, H. W., 1978, Equation of the growth rate of frost forming on cooled surfaces, *International Journal of Heat and Mass Transfer*, vol. 21, pp. 1019–1024.

Schulte, D. W., Howell, R. H., 1982, The effect of air turbulence on the rate of frost growth on a horizontal flat plate, *ASHRAE Transactions*, vol. 88, pt. 2, pp. 201–217.

Sengupta, S., Sherif, S. A., Wong, K. V., 1998, Empirical heat transfer and frost thickness correlations during frost deposition on a cylinder in cross-flow in the transient regime, *International Journal of Energy Research*, vol. 22, pp. 615-624.

Shah, R. K., London, A. L., 1978, *Laminar Flow Forced Convection in Ducts – A Source Book for Compact Heat Exchanger Analytical Data*, Academic Press, New York.

Sherif, S. A., Raju, S. P., Padki, M. M., Chan, A. B., 1993, A semi-empirical transient method for modeling frost formation on a flat plate, *International Journal of Refrigeration*, vol. 16, no. 15, pp. 321-329.

Shin, J., Tikhonov, A. V., Kim, C., 2003, Experimental study on frost structure on surfaces with different hydrophilicity: density and thermal conductivity, *Journal of Heat Transfer*, vol. 125, pp. 84-94.

Smith, G. R., 1989, Theoretical cooling coil calculations at freezer temperatures to avoid unfavorable coil-frost, *ASHRAE Transactions*, vol. 95, pt. 2, pp. 1138-1148.

Stoecker, W. F., 1957, How frost formation on coils affects refrigeration systems, *Refrigerating Engineering*, vol. 65, no. 2, pp. 42-46.

Stoecker, W. F., 1960, Frost formation on refrigeration coils, *ASHRAE Transactions*, vol. 66, pp. 91-103.

Stoecker, W. F., Jones, J. W., 1982, Refrigeration and Air Conditioning, Second Edition, McGraw-Hill, Inc., p. 54-55.

Storey, B. D., Jacobi, A. M., 1999, The effect of streamwise vortices on the frost growth rate in developing laminar channel flows, *International Journal of Heat and Mass Transfer*, vol. 42, pp. 3787-3802.

Tantakitti C., Howell R. H., 1986, Air to air heat pumps operating under frosting conditions on the outdoor coil, *ASHRAE Transactions.*, vol. 92, pt. 1, pp. 827-842.

Tao, Y.-X., Besant, R. W., 1993, Prediction of spatial and temporal distributions of frost growth on a flat plate under forced convection, *Journal of Heat Transfer*, vol. 115, pp. 278-281.

Tao, Y.-X., Besant, R. W., Mao, Y., 1993a, Characteristics of frost growth on a flat plate during the early growth period, *ASHRAE Transactions*, vol. 99, pp. 746-753.

Tao, Y.-X., Besant, R. W., Rezkallah, K. S., 1993b, A mathematical model for predicting the densification and growth of frost on a flat plate, *International Journal of Heat and Mass Transfer*, vol. 36, no. 2, pp. 353-363.

Tao, Y.-X., Mao, Y., Besant, R. W., 1994, Frost growth characteristics on heat exchanger surfaces: Measurement and simulation studies, Fundamentals of Phase Change: Sublimation and Solidification, *ASME HTD*, vol. 286, pp. 29-38.

Thomas, L., Chen, H., Besant, R. W., 1999, Measurement of frost characteristics on heat exchanger fins, Part I: Test facility and instrumentation, *ASHRAE Transactions*, vol. 105, pt. 2, pp. 283-293.

Tittle, C. W., 1965, Boundary value problems in composite media: quasi-orthogonal functions, *Journal of Applied Physics*, vol. 36, no. 4, pp. 1486-1488.

Tokura, I., Saito, H., Kishinami, K., 1983, Study on properties and growth rate of frost layers on cold surfaces, *Journal of Heat Transfer*, vol. 105, pp. 895-901.

Trammel, G. J., Little, D. C., Killgore, E. M., 1968, A study of frost formed on a flat plate held at sub-freezing temperature, *ASHRAE Journal*, vol. 10, no. 7, pp. 42-47.

Wang, C.-C., Huang, R.-T., Sheu,W.-J., Chang, Y.-J., 2004, Some observations of the frost formation in free convection: with and without the presence of electric field, *International Journal of Heat and Mass Transfer*, vol. 47, no. 14-16, pp. 3491-3505.

Watters, R. J., O'Neal, D. L., Yang, J., 2001a, Effect of fin staging on frost/defrost performance of a two-row heat pump evaporator at standard test conditions, *ASHRAE Transactions*, vol. 107, pt 2, pp. 240-249.

Watters, R. J., O'Neal, D. L., Yang, J., 2001b, Effect of fin staging on frost/defrost performance of a two-row heat pump evaporator under heavy frosting conditions, *ASHRAE Transactions*, vol. 107, pt 2, pp. 250-258.

Wibulswas, P., 1966, Laminar-Flow Heat-Transfer in Non-Circular Ducts, Ph.D. thesis, London University, London.

Wu, G., Bong, T.-Y., 1994, Overall efficiency of a straight fin with combined heat and mass transfer, *ASHRAE Transactions*, vol. 100, pp. 367-374.

Wu, X. M., Webb, R. L., 2001, Investigation of the possibility of frost release from a cold surface, *Experimental Thermal and Fluid Science*, vol. 24, pp. 151-156.

Wu, Y., Verma, P., Bullard, C. W., Hrnjak, P. S., 2001, Simulating the Performance of a Heat Exchanger During Frosting, ACRC TR-186, University of Illinois, Urbana-Champaign.

Xia, Y., Jacobi, A. M., 2004, An exact solution to steady heat conduction in a two-dimensional slab on a one-dimensional fin: application to frosted heat exchangers, *International Journal of Heat and Mass Transfer*, vol. 47, pp. 3317-3326.

Yamakawa, N., Takahashi, N., Ohtani, S., 1972, Forced convection heat and mass transfer under frost condition, *Heat Transfer- Japanese Research*, vol. 1, no. 2, pp. 1-10.

Yan, L., Haji-Sheikh, A., Beck, J. V., 1993, Thermal characteristics of two-layered bodies with embedded thin-film heat source, *Journal of Heat Transfer*, vol. 115, pp. 276-283.

Yan, W.-M., Li, H.-Y., Tsay, Y.-L., 2005, Thermofluid characteristics of frosted finned-tube heat exchangers, *International Journal of Heat and Mass Transfer*, vol. 48, pp. 3073-3080.

Yonko, J. D., Sepsy, C. F., 1967, An investigation of the thermal conductivity of frost while forming on a flat horizontal plate, *ASHRAE Transactions*, vol. 73, pt 2, no. 2043.

Yun, R., Kim, Y., Min, M., 2002, Modeling of frost growth and frost properties with airflow over a flat plate, *International Journal of Refrigeration*, vol. 25, pp. 362-371.

Appendix A: An Eigenvalue Problem

The eigenvalue problem

$u'' + \gamma u = 0$, satisfying (A.1)

$u'(1) = c_1 u(1)$, and (A.2a)

$u'(0) = \gamma c_2 u(0)$ (A.2b)

is unusual, because the eigenvalue appears in the boundary condition. Following Friedman (1956), who presented the solution to a similar problem, we consider the space of two-component vectors U whose first component is a real twice-differentiable function $u(x)$ and whose second component is a real number u_o. That is,

$$U = \begin{pmatrix} u(x) \\ u_o \end{pmatrix} \quad . \tag{A.3}$$

Define the scalar product of two vectors U and V as

$$\langle \mathrm{U}\ , \mathrm{V} \rangle = \int_0^1 u(x)v(x)\mathrm{d}x - c_2 u_0 v_0 \quad , \tag{A.4}$$

and consider a subspace D of vectors U, such that

$u'(1) = c_1 u(1)$, and (A.5a)

$u(0) = u_o$. (A.5b)

If the linear operator, L, is defined such that

$$LU = \begin{pmatrix} -u''(x) \\ u'(0)/c_2 \end{pmatrix} \quad , \tag{A.6}$$

then the eigenvalue problem is reduced to finding a vector U in D such that $LU=\gamma U$. Moreover, with Equations (A.4) and (A.6) we have

$$\langle V, LU \rangle = -\int_0^1 v(x)u''(x)\mathrm{d}x - c_2 v_0 u'(0)/c_2 \quad \text{, which gives} \tag{A.7a}$$

$$\langle V, LU \rangle = \left[-vu' + v'u \right]_0^1 - \int_0^1 uv''\mathrm{d}x - v(0)u'(0) \quad \text{, or} \tag{A.7b}$$

$$\langle V, LU \rangle = -\int_0^1 uv''\mathrm{d}x - u_0 v'(0) = \langle LV, U \rangle \quad . \tag{A.7c}$$

Equations (A.7) prove that L is self-adjoint, and therefore all the eigenvalues are real valued, and the eigenfunctions are orthogonal in the sense of Equation (A.4), i.e.

$$\langle U_m, U_n \rangle \begin{cases} = 0, & m \neq n \\ \neq 0, & m = n \end{cases} \quad . \tag{A.8}$$

Any arbitrary function can be expressed as a series of the eigenfunctions, e.g. let

$$F = \begin{pmatrix} f(x) \\ f(0) \end{pmatrix} \text{ and } U_n = \begin{pmatrix} u_n(x) \\ u_n(0) \end{pmatrix} \tag{A.9}$$

be vectors in D, where $u_n(x)$ is the solution of the original differential equation, corresponding to eigenvalue γ_n. Then we have the expansion

$$F = \sum \alpha_n U_n \quad , \text{ or} \tag{A.10}$$

$$f(x) = \sum_1^\infty \alpha_n u_n(x) \text{ and } f(0) = \sum_0^\infty \alpha_n u_n(0) \quad , \tag{A.11}$$

where the coefficients α_n's are determined by

$$\alpha_n = \frac{\langle F, U_n \rangle}{\langle U_n, U_n \rangle} = \frac{\int_0^1 f(x) u_n(x) \mathrm{d}x - c_2 f(0) u_n(0)}{\int_0^1 [u_n(x)]^2 \, \mathrm{d}x - c_2 [u_n(0)]^2} \quad . \tag{A.12}$$

Appendix B: Fin Efficiency Problems

The physical situation of interest, frost on a metallic fin, is described in Chapter 2.2. The metallic fin and the frost slab form a composite medium. The convection coefficient, free-stream dry and wet bulb temperatures, base temperature, and thermophysical properties are considered as constant. The mass deposition occurs everywhere on the frost surface, and the frost layer is assumed to be of uniform thickness. There is no contact resistance between the frost and the fin. The following assumptions are invoked: steady-state, two-dimensional conduction in frost layer on a one-dimensional fin, with no internal generation, and constant properties. With these assumptions, the fin temperature T_{fi} is a function of x only, and the frost temperature is $T_f(x,y)$. The governing equations for the temperature distribution are:

$$k_{fi}t\frac{d^2T_{fi}}{dx^2}+k_f\left.\frac{\partial T_f}{\partial y}\right|_{y=0}=0 \qquad \text{in } 0<x<H_f/2, \text{ and} \tag{B.1a}$$

$$\frac{\partial^2 T_f}{\partial x^2}+\frac{\partial^2 T_f}{\partial y^2}=0 \qquad \text{in } 0<x<H_f/2,\ 0<y<\delta_f, \tag{B.1b}$$

subject to

$$\left.\frac{dT_{fi}}{dx}\right|_{x=H_f/2}=0,\ \left.\frac{\partial T_f}{\partial x}\right|_{x=H_f/2}=0, \tag{B.2a}$$

$$T_{fi}(0)=T_w,\ T_f(0,y)=T_w, \tag{B.2b}$$

$$T_{fi}(x)=T_f(x,0), \text{ and} \tag{B.2c}$$

$$\left.\frac{\partial T_f}{\partial y}\right|_{y=\delta_f}=\frac{h}{k_f}\left(T_a-T_f\left(x,\delta_f\right)\right)+\frac{h_{sg}g_m}{k_f}\left(\varpi_a-\varpi_{fs}\left(x,\delta_f\right)\right), \tag{B.2d}$$

where ω_{fs} is the saturated humidity ratio corresponding to $T_f(x,\delta_f)$. Note that the fully frosted condition implies that ω_a is always bigger than ω_{fs}. If there is no mass transfer between the air and the frost, Equation (B.2d) should be replaced by

$$\left.\frac{\partial T_f}{\partial y}\right|_{y=\delta_f}=\frac{h}{k_f}\left(T_a-T_f\left(x,\delta_f\right)\right). \tag{B.3}$$

Xia and Jacobi (2004) provided the analytical solution to Equations (B.1) subject to (B.2a)-(B.2c) and (B.3). The full series solution is

$$\frac{T_f(x,y)-T_a}{T_w-T_a}=\sum_{n=1}^{\infty}C_n\left[\cos\left(\frac{\lambda_n y}{\delta_f}\right)-\frac{k_{fi}t}{k_f\delta_f}\lambda_n\sin\left(\frac{\lambda_n y}{\delta_f}\right)\right]\cosh\left(\frac{\lambda_n\left(H_f/2-x\right)}{\delta_f}\right), \tag{B.4a}$$

with C_n calculated using Equation (3.7b), and λ_n is the root of

$$\tan(\lambda_n)=\frac{k_{fi}k_f t}{\delta_f\left(k_f^2+hk_{fi}t\right)}\left[\left(\frac{h\delta_f^2}{k_{fi}t}\right)\frac{1}{\lambda_n}-\lambda_n\right]. \tag{B.4b}$$

Equations (B.4) provide a basis for deriving fin efficiencies.

Fin efficiency in the HA-LMED method

Based on Equations (3.1) and (3.2), Equations (B.1) and (B.2) can be reduced to

$$k_{fi}t\frac{d^2 i_{fi}}{dx^2}+k_f\left.\frac{\partial i_f}{\partial y}\right|_{y=0}=0 \qquad \text{in } 0<x<H_f/2, \text{ and} \tag{B.5a}$$

$$\frac{\partial^2 i_f}{\partial x^2}+\frac{\partial^2 i_f}{\partial y^2}=0 \qquad \text{in } 0<x<H_f/2,\ 0<y<\delta_f, \tag{B.5b}$$

subject to the following boundary conditions:

$$\left.\frac{di_{fi}}{dx}\right|_{x=H_f/2}=0,\ \left.\frac{\partial i_f}{\partial x}\right|_{x=H_f/2}=0, \tag{B.6a}$$

$$i_{fi}(0)=i_w,\ i_f(0,y)=i_w, \tag{B.6b}$$

$$i_{fi}(x)=i_f(x,0), \text{ and} \tag{B.6c}$$

$$\left.\frac{\partial i_f}{\partial y}\right|_{y=\delta_f}=\frac{hb/c_{p_a}}{k_f}\left(i_a-i_f\left(x,\delta_f\right)\right), \tag{B.6d}$$

where $i_{fi}(x)$ and $i_f(x,y)$ are the saturated enthalpies of moist air at corresponding temperatures. Comparing Equations (B.5) and (B.6) to (B.1), (B.2a)-(B.2c) and (B.3), the solution is obtained by replacing the T's and h in Equations (B.4) with i's and hb/c_{pa}.

The total heat transfer per unit fin width to the fin surface is then calculated by

$$\frac{q_{fi,b}}{L_f}=4\left(k_{fi}t/b\left.\frac{di_{fi}}{dx}\right|_{x=0}+\int_0^{\delta_f}k_f/b\left.\frac{\partial i_f}{\partial x}\right|_{x=0}dy\right). \tag{B.7}$$

Then, the fin efficiency defined by Equation (3.6) is calculated to obtain Equation (3.7).

Starting from the definition, Equation (3.5), and considering the total heat transfer as comprised of $q_{fi,b}$ and $q_{w,unf}$, which are the heat transfer to the frosted fin surface and to the unfinned surface respectively, the surface efficiency is obtained as

$$\eta_h=\frac{q_{fi,b}}{A_h\left(h_h/c_{p_a}\right)\left(i_a-i_{w,o}\right)}+\frac{q_{w,unf}}{A_h\left(h_h/c_{p_a}\right)\left(i_a-i_{w,o}\right)}. \tag{B.8}$$

For $q_{w,unf}$, we have

$$q_{w,unf}=\left(A_h-A_{fi}\right)\left(h_h/c_{p_a}\right)\left(i_a-i_{fs,w}\right). \tag{B.9}$$

Assuming one-dimensional heat conduction in the frost layer on the tube wall (normal to the tube wall), the saturated enthalpy corresponding to the temperature of the frost surface on the tube wall can be expressed as

$$i_{fs,w}=\frac{i_a\left(h_hb/c_{p_a}\right)+i_{w,o}k_f/\delta_f}{\left(h_hb/c_{p_a}\right)+k_f/\delta_f}. \tag{B.10}$$

Substituting Equations (3.6), (B.9), and (B.10) into Equation (B.8), the expression for overall surface efficiency, Equation (3.10), is obtained.

Fin efficiency in the UA-LMTD method

Here the mass transfer effects are included in the convective heat transfer coefficient *h* by utilizing the assumption of constant sensible heat ratio. Equations (B.1) and (B.2) remain unchanged, except that the last boundary condition, Equation (B.2d) becomes

$$\left.\frac{\partial T_f}{\partial y}\right|_{y=\delta_f} = \frac{hq_a / q_{a,s}}{k_f}\left(T_a - T_f\left(x,\delta_f\right)\right). \tag{B.11}$$

The solution can be easily obtained by replacing the h in Equations (B.4) with $hq_a/q_{a,s}$. The details of the derivation are omitted.

If mass transfer effects are to be isolated, and a linear relation between the saturated humidity ratio and temperature from fin tip to base is assumed, then the last boundary condition, Equation (B.2d), is rewritten as

$$\left.\frac{\partial T_f}{\partial y}\right|_{y=\delta_f} = \frac{h}{k_f}\left(T_a - T_f\left(x,\delta_f\right)\right) + \frac{h_{sg}g_m}{k_f}\left[\left(\varpi_a - \varpi_{a,sat}\right) + \left(\varpi_{a,sat} - \varpi_{fs}\left(x,\delta_f\right)\right)\right], \tag{B.12}$$

where $\omega_{a,sat}$ is the saturated humidity ratio corresponding to the temperature of the moist air. Noting that (ω_a-$\omega_{a,sat}$) is constant, and using Equation (3.33), Equation (B.12) becomes

$$\left.\frac{\partial T_f}{\partial y}\right|_{y=\delta_f} = \frac{h'}{k_f}\left(T_a' - T_f\left(x,\delta_f\right)\right), \text{ with} \tag{B.13}$$

$$h' = h\left(1 + \frac{h_{sg}g_m e}{h}\right), \text{ and} \tag{B.14}$$

$$T_a' = T_a + \frac{h_{sg}g_m / h}{1 + h_{sg}g_m e / h}\left(\varpi_a - \varpi_{a,sat}\right). \tag{B.15}$$

The solution to Equations (B.1) and (B.2) with (B.13) substituted for (B.2d) can be easily obtained by replacing h and T_a in Equation (B.4) with h' and T_a'.

The total heat transfer to the fin surface per unit fin width is then calculated by

$$\frac{q_{fi,b}}{L_f} = 4\left(k_{fi}t\left.\frac{dT_{fi}}{dx}\right|_{x=0} + \int_0^{\delta_f} k_f \left.\frac{\partial T_f}{\partial x}\right|_{x=0} dy\right). \tag{B.16}$$

The maximum heat transfer is (were the fin surface at the base temperature)

$$\frac{q_{\max}}{L_f} = 2H_f\left[h\left(T_a - T_w\right) + h_{sg}g_m\left(\varpi_a - \varpi_{w,sat}\right)\right] = 2H_f h'\left(T_a' - T_w\right). \tag{B.17}$$

Thus, the fin efficiency is calculated yielding Equation (3.34).

Appendix C: Ancillary Procedures

The values for the cross-flow correction factor, F: they are obtained using correlations constructed from the plot of LMTD correction factor for a cross-flow heat exchanger developed by Bowman *et al.* (1940). First, two values are calculated:

$$P_F = \frac{T_{r,o} - T_{r,i}}{T_{a,i} - T_{r,i}}, \text{ and} \tag{C.1}$$

$$R_F = \frac{T_{a,i} - T_{a,o}}{T_{r,o} - T_{r,i}}. \tag{C.2}$$

Then, F is calculated using appropriate correlation according to the value of R_F (interpolation is needed when R_F is not equal to those specific values):

$$F = \begin{cases} 1.006503497\text{-}0.91002331P_F + 14.86742424P_F^{\,2}\text{-}75.83041958P_F^{\,3}, & R_F = 5 \\ 1.004516484\text{-}0.552422577P_F + 7.696053946P_F^{\,2}\text{-}36.71328671P_F^{\,3}, & R_F = 4 \\ 1.009437564\text{-}0.706546698P_F + 7.585461816P_F^{\,2}\text{-}25.76754386P_F^{\,3}, & R_F = 3 \\ 1.020288538\text{-}1.078900562P_F + 9.201685043P_F^{\,2}\text{-}23.70241315P_F^{\,3}, & R_F = 2.5 \\ 1.000939394\text{-}0.096343942P_F + 0.751652682P_F^{\,2}\text{-}4.091496583P_F^{\,3}, & R_F = 2 \\ 1.00035991\text{-}0.051020131P_F + 0.257962099P_F^{\,2}\text{-}1.90621894P_F^{\,3}, & R_F = 1.5 \\ 1.000535056\text{-}0.051630981P_F + 0.180643473P_F^{\,2}\text{-}1.033913698P_F^{\,3}, & R_F = 1 \end{cases}. \tag{C.3}$$

The correlations for properties of moist air are:

$$\rho = 1.287\text{-}0.005T\text{-}2.013\varpi; \tag{C.4}$$

$$c_p = 1.006\text{+}5.643\text{e-}5T\text{+}1.839\varpi; \tag{C.5}$$

$$k = 0.0236\text{+}7.615\text{e-}5T\text{+}0.00337\varpi; \tag{C.6}$$

$$\mu = 1.730\text{e-}5\text{+}4.96\text{e-}8T\text{-}2.455\text{e-}6\varpi; \tag{C.7}$$

$$\text{Pr} = 0.7363\text{-}2.333\text{e-}4T; \tag{C.8}$$

$$D_{12}\text{=}2.3\text{e-}5\left(\frac{T\text{+}273}{273}\right)^{1.74}\frac{101\text{e}3}{P_{amb}}. \tag{C.9}$$

The correlation for the specific heat of ethyl alcohol is:

$$c_p = 2.230044\text{+}6.741\text{e-}3T\text{+}6.67286\text{e-}5T^2\text{+}4.65\text{e-}7T^3\text{+}1.43\text{e-}9T^4. \tag{C.10}$$

To calculate the humidity ratio of moist air at dew point temperature T and ambient pressure P_{amb}:

$$\varpi\text{=}0.62198\frac{P_w}{P_{amb}\text{-}P_w}, \text{ where} \tag{C.11}$$

$$P_w\text{=}\text{Exp}\left[\frac{C_1}{T\text{+}273} + C_2 + C_3\left(T\text{+}273\right) + C_4\left(T\text{+}273\right)^2 + C_5\left(T\text{+}273\right)^3 + C_6\left(T\text{+}273\right)^4 + C_7\,\text{Log}\left(T\text{+}273\right)\right], \tag{C.12}$$

with C_1=-5.6745359e3; C_2=6.3925247; C_3=-9.677843e-3; C_4=6.2215701e-7; C_5=2.0747825e-9; C_6=-9.484024e-13; and C_7=4.1635019.

To calculate the latent heat of ablimation for water vapor:

$$h_{sg}\text{=}h_1 - h_2, \text{ with} \tag{C.13}$$

$$h_1 = A_0 + A_1(T+273) + A_2(T+273)^2 + A_3(T+273)^3 + A_4(T+273)^4 + A_5(T+273)^5 - R(T+273)^2\left(db'\right)P_{ice}, \quad \text{(C.14)}$$

and

$$h_2 = D_0 + D_1(T+273) + D_2(T+273)^2 + D_3(T+273)^3 + D_4 P_{ice}, \text{ where} \quad \text{(C.15)}$$

$$P_{ice} = 661.36\text{Exp}\left(0.09575T\right), \quad \text{(C.16)}$$

$$db' = 0.147184\text{e-}8\frac{1734.29}{\left(\text{T}+273\right)^2}\text{Exp}\left(\frac{1734.29}{\text{T}+273}\right), \quad \text{(C.17)}$$

with $R=0.4615199$; A_0=0.199798e4; A_1=0.18035706e1; A_2=0.36400463e-3; A_3=-0.14677622e-5; A_4=0.28726608e-8; A_5=-0.17508262e-11; D_0=-0.647595e3; D_1=0.274292; D_2=0.2910583e-2; D_3=0.1083437e-5; and D_4=0.107e-5.

Appendix D: An Analytical Expression for the Outlet Humidity Ratio

An analytical expression for outlet humidity ratio will be derived, based on the following equations for heat and mass transfer rates and conservation of energy on both sides of a counter-flow heat exchanger:

$$\mathrm{d}q_a = -\dot{m}_r c_{p_r} \mathrm{d}T_r\,, \tag{D.1}$$

$$\mathrm{d}q_{a,s} = -\dot{m}_a c_{p_a} \mathrm{d}T_a\,, \tag{D.2}$$

$$\mathrm{d}q_{a,s} = \mathrm{d}\tilde{A}_h h_h \eta_h \left(T_a - T_w\right), \tag{D.3}$$

$$\mathrm{d}q_a = \mathrm{d}\tilde{A}_c h_c \left(T_w - T_r\right), \tag{D.4}$$

$$\mathrm{d}q_{a,l} = \mathrm{d}\tilde{A}_h h_{sg} g_m \left(\varpi_a - \varpi_s\right), \tag{D.5}$$

$$\mathrm{d}q_{a,l} = -h_{sg} \dot{m}_a \mathrm{d}\varpi_a\,. \tag{D.6}$$

The derivation is aimed at the frosted part of the airside surface and the corresponding tube side surface, because otherwise Equations (D.5) and (D.6) will be invalid. Note that $\tilde{A}_h$ and $\tilde{A}_c$ denote the independent variables, while A_h and A_c denote the total area. Combine Equations (D.5) and (D.6), we have

$$\frac{\mathrm{d}\varpi_a}{\mathrm{d}\tilde{A}_h} = -\frac{g_m}{\dot{m}_a}\varpi_a + \frac{g_m}{\dot{m}_a}\varpi_s\,. \tag{D.7}$$

Assuming a linear relationship between the humidity ratio and temperature of saturated moist air, that is

$$\varpi_s = aT_s + b\,, \tag{D.8}$$

then Equation (D.7) becomes

$$\frac{\mathrm{d}\varpi_a}{\mathrm{d}\tilde{A}_h} = -\frac{g_m}{\dot{m}_a}\varpi_a + \frac{g_m}{\dot{m}_a}\left(aT_s + b\right). \tag{D.9}$$

From Chapter 4, we have

$$T_s = \frac{\left[1 - \lambda^2\left(k_{fi}t\right)/\left(k_f\delta_f\right)\right]}{\cosh\left(\lambda H_f / 2\delta_f\right)}\left[T_w - T_a\right] + T_a\,, \text{ and} \tag{D.10}$$

$$T_w = \frac{T_a h_h \left(q_a / q_{a,s}\right)\eta_h A_h + T_r h_c A_c}{h_h \left(q_a / q_{a,s}\right)\eta_h A_h + h_c A_c}\,. \tag{D.11}$$

Substitute Equation (D.11) into (D.10), and rearrange to obtain

$$T_s = M'\left(T_r - T_a\right) + T_a\,, \text{ where} \tag{D.12}$$

$$M' = \frac{MA_c h_c}{h_h \left(q_a / q_{a,s}\right)\eta_h A_h + h_c A_c}\,, \text{ and} \tag{D.13}$$

$$M = \frac{\left[1 - \lambda^2\left(k_{fi}t\right)/\left(k_f\delta_f\right)\right]}{\cosh\left(\lambda H_f / 2\delta_f\right)}\,. \tag{D.14}$$

Thus, Equation (D.9) becomes

$$\frac{\mathrm{d}\varpi_a}{\mathrm{d}\tilde{A}_h} = -\frac{g_m}{\dot{m}_a}\varpi_a + \frac{g_m}{\dot{m}_a}\left\{a\left[M'\left(T_r - T_a\right) + T_a\right] + b\right\}. \tag{D.15}$$

Next, expressions of T_a and T_r as functions of $\tilde{A}_h$ (or the airside flow path) are derived. Eliminate T_w from Equations (D.3) and (D.4), and we have

$$T_a - T_r = \frac{\mathrm{d}q_{a,s}}{\mathrm{d}\tilde{A}_h \eta_h h_h} + \frac{\mathrm{d}q_a}{\mathrm{d}\tilde{A}_c h_c}. \tag{D.16}$$

Extract ($\mathrm{d}q_{a,s}/\mathrm{d}\tilde{A}_h$) from RHS of Equation (D.16), consider $\mathrm{d}\tilde{A}_c/\mathrm{d}\tilde{A}_h = A_c/A_h$=constant, and assume $\mathrm{d}q_a/\mathrm{d}q_{a,s} = q_a/q_{a,s}$ =constant as we did in Chapter 3, then we have

$$T_a - T_r = \frac{\mathrm{d}q_{a,s}}{\mathrm{d}\tilde{A}_h}\left[\frac{1}{\eta_h h_h} + \frac{\left(q_a / q_{a,s}\right)}{\left(A_c / A_h\right) h_c}\right]. \tag{D.17}$$

Combining Equations (D.1) and (D.2) gives

$$\mathrm{d}\left(T_a - T_r\right) = \frac{\mathrm{d}q_a}{\dot{m}_r c_{p_r}} - \frac{\mathrm{d}q_{a,s}}{\dot{m}_a c_{p_a}}. \tag{D.18}$$

Extract $\mathrm{d}q_{a,s}$ from RHS of Equation (D.18) and use the assumption of constant sensible heat ratio again, and the equation becomes

$$\mathrm{d}\left(T_a - T_r\right) = \mathrm{d}q_{a,s}\left[\frac{\left(q_a / q_{a,s}\right)}{\dot{m}_r c_{p_r}} - \frac{1}{\dot{m}_a c_{p_a}}\right]. \tag{D.19}$$

Combine Equations (D.17) and (D.19), and we have

$$\frac{\mathrm{d}\left(T_a - T_r\right)}{\left(T_a - T_r\right)} = \mathrm{d}\tilde{A}_h \frac{\left[\frac{\left(q_a / q_{a,s}\right)}{\dot{m}_r c_{p_r}} - \frac{1}{\dot{m}_a c_{p_a}}\right]}{\left[\frac{1}{\eta_h h_h} + \frac{\left(q_a / q_{a,s}\right)}{\left(A_c / A_h\right) h_c}\right]} \triangleq K\mathrm{d}\tilde{A}_h, \tag{D.20}$$

where the constant K is introduced for simplicity,

$$K = \frac{\left[\frac{\left(q_a / q_{a,s}\right)}{\dot{m}_r c_{p_r}} - \frac{1}{\dot{m}_a c_{p_a}}\right]}{\left[\frac{1}{\eta_h h_h} + \frac{\left(q_a / q_{a,s}\right)}{\left(A_c / A_h\right) h_c}\right]}. \tag{D.21}$$

Integrate Equation (D.20), and we get an expression of (T_a - T_r) as a function of $\tilde{A}_h$:

$$T_a - T_r = \left(T_{a,i} - T_{r,o}\right)\exp\left(K\tilde{A}_h\right). \tag{D.22}$$

Next, from Equations (D.2), (D.17) and (D.22) we have

$$\frac{\mathrm{d}T_a}{\mathrm{d}\tilde{A}_h} = \frac{\left(T_{r,o} - T_{a,i}\right)}{\dot{m}_a c_{p_a}\left[\frac{1}{\eta_h h_h} + \frac{\left(q_a / q_{a,s}\right)}{\left(A_c / A_h\right) h_c}\right]}\exp\left(K\tilde{A}_h\right). \tag{D.23}$$

Integration gives

$$
\begin{aligned}
T_a &= T_{a,i} + \frac{\left(T_{r,o} - T_{a,i}\right)}{\dot{m}_a c_{p_a} K \left[\frac{1}{\eta_h h_h} + \frac{\left(q_a / q_{a,s}\right)}{\left(A_c / A_h\right) h_c}\right]} \left[\exp\left(K\tilde{A}_h\right) - 1\right] \\
&= T_{a,i} + K^{'}\left[\exp\left(K\tilde{A}_h\right) - 1\right]
\end{aligned}, \tag{D.24}
$$

where

$$
K^{'} = \frac{\left(T_{a,i} - T_{r,o}\right)}{\dot{m}_a c_{p_a}\left[\frac{1}{\dot{m}_a c_{p_a}} - \frac{\left(q_a / q_{a,s}\right)}{\dot{m}_r c_{p_r}}\right]}. \tag{D.25}
$$

Thus, Equation (D.15) takes the form

$$
\begin{aligned}
\frac{\mathrm{d}\varpi_a}{\mathrm{d}\tilde{A}_h} &= -\frac{g_m}{\dot{m}_a}\varpi_a + \frac{g_m}{\dot{m}_a}\left\{a\left[M^{'}\left(T_{r,o} - T_{a,i}\right)\exp\left(K\tilde{A}_h\right) + T_{a,i} + K^{'}\left(\exp\left(K\tilde{A}_h\right) - 1\right)\right] + b\right\} \\
&= -\frac{g_m}{\dot{m}_a}\varpi_a + \frac{g_m}{\dot{m}_a}K^{"}\exp\left(K\tilde{A}_h\right) + \frac{g_m}{\dot{m}_a}K^{'''}
\end{aligned}. \tag{D.26}
$$

where

$$
K^{"} = a\left[M^{'}\left(T_{r,o} - T_{a,i}\right) + K^{'}\right], \text{ and} \tag{D.27}
$$

$$
K^{'''} = a\left(T_{a,i} - K^{'}\right) + b. \tag{D.28}
$$

Integrating Equation (D.26), we finally get

$$
\omega_a = \left[\varpi_i - \frac{\left(g_m / \dot{m}_a\right)K^{"}}{K + \left(g_m / \dot{m}_a\right)} - K^{'''}\right]\exp\left(-\frac{g_m}{\dot{m}_a}\tilde{A}_h\right) + \frac{\left(g_m / \dot{m}_a\right)K^{"}}{K + \left(g_m / \dot{m}_a\right)}\exp\left(K\tilde{A}_h\right) + K^{'''}. \tag{D.29}
$$

The values for coefficients *a* and *b* in Equation (D.8): Assuming a linear relationship between the humidity ratio and temperature of saturated moist air within the range of the surface temperature encountered in this study, -13 to -1 ºC, the coefficients are determined by throwing a curve fit of first order polynomial to the saturated humidity ratio with respect to temperature. The values are

$$
a = 0.000186347, \text{ and} \tag{D.30}
$$

$$
b = 0.00349672. \tag{D.31}
$$

Appendix E: An Analytical Method for Predicting the Area of Frosted Surface

Figure E.1 illustrates a partially frosted counter-flow heat exchanger. Conduction resistance of the tube wall is neglected. The problem is to determine the area of the frosted portion, $A_{h,f}$, given that the inlet and outlet conditions, air and coolant mass flow rates, and convection coefficients $h_{h,2}$ and h_c are known.

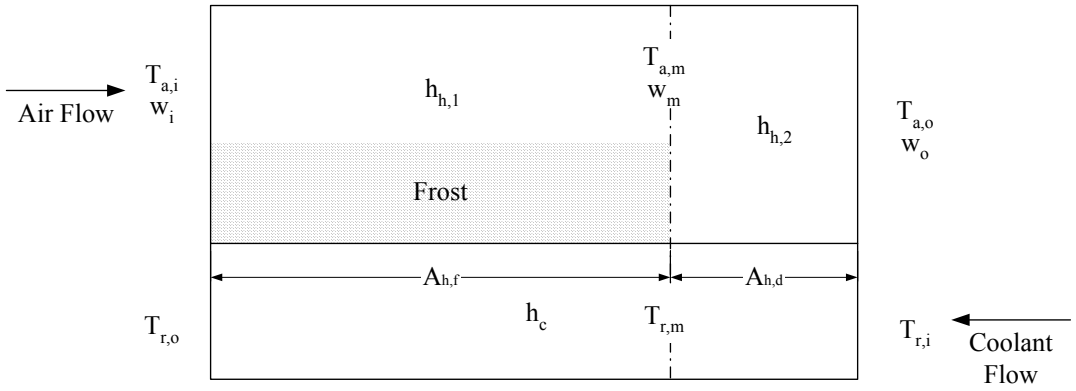

Figure E.1 Schematic of a partially frosted counter-flow heat exchanger.

Since no mass transfer occurs over the dry part, the humidity ratio will not change over that part and will equal to the saturated humidity ratio of moist air corresponding to the temperature of the wall where the dry surface starts, i.e.,

$$\varpi_m = \varpi_o = \varpi_{sat}\left(T_{w,m}\right). \tag{E.1}$$

Thus, $T_{w,m}$ is determined from the above equation. The equality of heat transfer rates over an infinitesimal area dA_h (or corresponding dA_c) located at the very beginning of the dry part gives

$$\mathrm{d}A_c h_c\left(T_{w,m} - T_{r,m}\right) = \mathrm{d}A_h h_{h_2}\left(T_{a,m} - T_{w,m}\right). \tag{E.2}$$

The heat balance for the dry part gives

$$\dot{m}_a c_{p_a}\left(T_{a,m} - T_{a,o}\right) = \dot{m}_r c_{p_r}\left(T_{r,m} - T_{r,i}\right). \tag{E.3}$$

Combining Equations (E.2) and (E.3), and keeping in mind that dA_c/dA_h=A_c/A_h, we can solve for $T_{r,m}$ and $T_{a,m}$,

$$T_{r,m} = \frac{A_c h_c T_{w,m} + A_h h_{h,2} T_{r,i}\dfrac{\dot{m}_r c_{p_r}}{\dot{m}_a c_{p_a}} + A_h h_{h,2}\left(T_{w,m} - T_{a,o}\right)}{A_c h_c + A_h h_{h,2}\dfrac{\dot{m}_r c_{p_r}}{\dot{m}_a c_{p_a}}}, \text{ and} \tag{E.4}$$

$$T_{a,m} = \frac{\dot{m}_r c_{p_r} T_{r,m} - \dot{m}_r c_{p_r} T_{r,i} + \dot{m}_a c_{p_a} T_{a,o}}{\dot{m}_a c_{p_a}}. \tag{E.5}$$

Next, apply the *UA*-LMTD method to the dry part, and note that $A_{c,d}/A_{h,d}$=A_c/A_h,

$$q_{a,2} = \dot{m}_a c_{p_a}\left(T_{a,m} - T_{a,o}\right); \tag{E.6}$$

$$UA_2 = q_{a,2} / \Delta T_{lm,2}\text{ ; and} \tag{E.7}$$

$$\frac{1}{UA_2} = \frac{1}{h_c A_{c,d}} + \frac{1}{h_{h,2} A_{h,d}} = \frac{1}{h_c A_{h,d} \left(A_c / A_h \right)} + \frac{1}{h_{h,2} A_{h,d}}. \tag{E.8}$$

Thus, the area of the frosted portion can be determined using

$$A_{h,f} = A_h - A_{h,d} = A_h \left[1 - UA_2 \left(\frac{1}{h_c A_c} + \frac{1}{h_{h,2} A_h} \right) \right]. \tag{E.9}$$

For a finned heat exchanger with a counter-cross flow configuration, the overall surface efficiency and a correction factor to the log-mean temperature difference should be applied to Equation (E.7).